Ship-cargo interaction for large and stiff cargo

Investigating the non-linear structural dynamics of cargo and sea-fastening subjected to ship-induced loads

MT54035

A.D. Speksnijder

Delft University of Technology

TU Delft

Thesis for the degree of MSc in Marine Technology in the specializations of Ship and Offshore Structures and Ship Hydromechanics

Ship-cargo interaction for large and stiff cargo

Investigating the non-linear structural dynamics of cargo and sea-fastening subjected to ship-induced loads

by

A.D. Speksnijder

at

BigLift Shipping

This thesis MT.23/24.011.M is classified as confidential in accordance with the general conditions for projects performed by the TU Delft.

To be defended publicly on Monday December 4, 2023 at 16:00

Thesis committee:	Dr. H.C. Seyffert	TU Delft, chair
	Dr. A. Grammatikopoulos	TU Delft
	Dr. A. Cabboi	TU Delft
	U. Karacadagli MSc	BigLift Shipping
	Ir. R. Verwey	BigLift Shipping

Project Duration:	February, 2023 - December, 2023
Institution:	Delft University of Technology
Faculty:	Faculty of Mechanical, Maritime and Materials Engineering, Delft
Student number:	4671813
Cover:	Photograph taken during the Yunlin project by BigLift

Electronic version: `http://repository.tudelft.nl/`

TU Delft

BIGLIFT

Preface

Dear reader,

This thesis on ”Ship-cargo interaction for large and stiff cargo” finalizes the master Marine Technology at Delft University of Technology. The research was conducted at BigLift Shipping, one of the leaders in the heavy-lift shipping market. Heavy-lift shipping is an area where both my specialization tracks ’Ship Hydromechanics’ and ’Ship and Offshore Structures’ are of great importance. The interaction between the tracks was something that I wanted to include in my research, leading to the thesis as presented to you.

I could not have completed this thesis without the help of many people. At first, I would like to thank my supervisors from Delft, being Apostolos Grammatikopoulos and Harleigh Seyffert. In my experience, they gave me a lot of freedom on how to tackle this problem. They were always open for discussions and supported me with new perspectives when I got stuck. I really enjoyed working together with you both. At last, I would like to thank Alessandro Cabboi for participating in the thesis committee and sharing his views on the thesis.

I also appreciate the support from Umut Karacadagli and Roel Verwey, and Anne Vreeburg for the first part, for their supervision from BigLift. They helped me envision the problem from the operative side, helping me to focus on the practical implementation of my results. Their constructive feedback helped me improve the quality of my research. Finally, something I also greatly value was being able to propose my own research problem.

At last, but certainly not least, I am grateful to my parents, brother, sister, flatmates, and friends for supporting me through my thesis. They helped me reflect on the process and kept me motivated.

A.D. Speksnijder
Delft, November 2023

Summary

An important trend exhibited by the offshore wind market is the increase in the size of wind turbines, leading to longer and stiffer monopiles with larger diameter-to-thickness ratios. Current transport analysis is focused on loads resulting from hydrodynamic accelerations, without taking into account loads resulting from differences in bending deflection between the vessel and cargo.

Research related to ship-cargo-fluid dynamics comprises shifting cargo related to stability, sloshing and its influence on dynamics and multi-body dynamics related to lifting operations. However, research concerning the impact of stiffness on dynamic behavior and structural response is limited. A specific study has shown the influence of the on the mode shapes, load distribution and eigenfrequencies, but some limitations were identified here. In this study, hydrodynamic contributions were excluded and linear modeling was applied. This emphasizes the need for further research.

Understanding the structural response of cargo and sea-fastening systems subjected to hydrodynamic loads helps engineers optimize support structures and identify potential risks that result in cargo damage. The identified knowledge gap is summarized in the following research question:

"How does the interaction between a vessel and large, stiff cargo affect the structural dynamic behavior, considering the influence of non-linear constraints posed by sea-fastening?"

This research aims to create an efficient numerical model that defines the responses of the cargo and sea-fastening system based on hydrodynamic loads. Using this model for analysis enables providing an answer on the research question.

An in-depth analysis is conducted on a project executed by BigLift. Analyzing this case in a static manner showed the sensitivity of force distribution in the sea-fastening system, particularly for stiff cargoes with low deflection. This analysis also showed that the axial deflection of the saddles and the bending deflection of the ship significantly influence the force distribution.

The dynamic analysis conducted on this case showed that this problem should indeed be modeled in a non-linear manner, because contact was lost for some saddles in the sea-fastening system. Linear modeling results in an overconstrained situation, overestimating forces in the sea-fastening system and bending moments in the cargo.

Finally, different parametric analyses are performed where the sea-fastening system and cargo properties are varied. Increasing the number of saddles in combination with decreasing their stiffness leads to a significant decrease in maximum force in the sea-fastening system and maximum bending moment in the cargo. But, increasing the number of saddles without decreasing its stiffness leads to increased non-linear behavior, caused by earlier cargo detachment from saddles in the sea-fastening system.

A parametric analysis related to the lashing properties showed little influence of this element on the structural response of the sea-fastening system and cargo. This can be explained by the difference in magnitude between lashing forces, weight of the cargo and resulting normal forces.

The last parametric analysis performed is related to the stiffness and length of the cargo. This parametric analysis showed that the normal force increases for both and increases in length and diameter. For the bending stress a decrease is observed for an increasing diameter, due to the increase in stiffness. In addition, the two different parameteric analyses performed on the cases with the largest structural response showed that certain different sea-fastening arrangements can be defined when the structural response boundary conditions are taken into account.

Finally, a workflow on how sea-fastening design can be performed in a more informed manner is identified, using the model created in this research.

Contents

1

Introduction

Within the offshore wind market, there is a significant trend towards larger wind turbines in terms of power and size, with rotor diameters exceeding 250 meters by 2030 [1, 2]. As a result, the monopiles used as foundation also increase in size [3]. Concerns arise that this increase in size could affect the transport operation. Current transport analysis is focused on loads resulting from hydrodynamic accelerations, without taking loads into account resulting from differences in bending deflection between the vessel and cargo.

BigLift Shipping is specialized in heavy-lift transport and is one of the leaders in this market. Within the BigLift fleet, a number of different ship classes are used to transport various types of cargo. This research focuses on stiff and oversized cargo, which is transported by MC-class carriers, capable of carrying loads up to 16.000 mT. Figure 1.1 shows an example of a project in which monopiles with a diameter of 8 meters were transported.

Figure 1.1: Example of large monopiles being carried by MC-class

The main particulars of this vessel type are shown in table 1.1. This information is based on data from BigLift. The table shows that the length is limited, especially in comparison to its breadth. This large breadth follows from stability and cargo capacity concerns.

Table 1.1: Main particulars MC-class vessel

Parameter		Value	Unit
Length overall	L	171	m
Breadth	B	42	m
Depth	H	12	m
Draught	T	6.5	m
Deadweight	DWT	20.675	mt
Displacement	∇	32.000	m^3

Knowledge gap

When analyzing ship-cargo interactions, extensive research is done on the influence of moving cargoes on ship stability or load distribution [4–6]. Much research is also available on the effect of sloshing on the dynamics of a vessel [7–9]. Finally, a vast amount of literature is present which models and analyzes the flexible multibody dynamics of suspended cargo during lifting and transport operations [10–14].

Research on the interaction effects between ship and stiff cargo, and the behavior of the combined system is limited. The research carried out by Mikail analyzes the influence of stiff monopiles on the frequency-response curves of a heavy lift vessel [15]. Although this research addresses the fact that it influences the frequency-response curves, some additional elements need to be investigated. Hydrodynamic contributions were excluded in this research, and the results were obtained using a linear approach. The thesis of Hazim showed that a linear versus non-linear approach can have significant influence on the frequency response curves [16]. A linear approach can lead to a large difference if it results in the problem being overconstrained. This emphasizes the need for further research.

Accurate knowledge of ship and cargo dynamics could be of great importance for heavy-lift transport. The design accelerations by the cargo define the size of the sea-fastening system that needs to be applied for safe transportation. With regard to the sea-fastening of heavy-lift shipping, some important behavior can be identified.

Heavily constraining the cargo by sea-fastening leads to load transfer from the ship to the cargo. In addition to the resulting stresses and stress concentrations, this could also lead to severe fatigue damage. From this point of view, loose sea-fastening is preferred. This implies that less loads are transferred from the vessel to the cargo, which preserves its fatigue life. Some studies have been conducted on fatigue damage to the sea-fastening system [17], but no research is found relating fatigue damage to cargo to the influence of loads transferred by the sea-fastening system. The need to understand the structural vibrations of the cargo is essential to define fatigue damage, as this contribution can become significant [18].

In contrast, not constraining the cargo enough could lead to unwanted vibration of the cargo, or it completely detaching from the sea-fastening system. In addition to this, Steelwind Norderham shows that for very high diameter-to-thickness ratios the monopile also becomes sensitive to damage at the support locations [19]. They showed that weight induces high local bending stresses, which could lead to local plasticity at support locations. This implies that too much reduction in sea-fastening grillage leads to structural deterioration of the monopile. Therefore, an optimum can be found in the level of constraining that is applied.

Relevance & Significance

Research shows that wind turbine transport and installation account for approximately 18 % of capital costs [20, 21]. Reducing the levelized cost of energy (LCOE) of offshore wind energy is one of the main concerns of the industry, to be more competitive to fossil-based alternatives. A better understanding of ship and cargo responses could result in a more optimized sea-fastening arrangement, which would lower transport costs.

A study of marine accidents in the heavy-lift industry showed that the second most significant contributor to accidents are technical failures, accounting for 23 % of the total failures [22]. In Europe maritime

accidents account for 140 deaths and 1.5 billion euros damage annually [23]. This is especially true in heavy-lift shipping, in which cargoes are specialized and of high value. For the cargoes transported by BigLift, the values transported by the MC-class can be multiples of 10 million euros. This data is based on consultation with BigLift cargo superintendents.

This emphasizes the need for a thorough understanding of the ship-cargo interactions in relation to the sea-fastening system, to mitigate the risk of a technical failure. This is emphasized by the increasing diameter-to-thickness ratios of the monopiles, making them more vulnerable in general. This research has the potential to enhance the understanding of interactions and inform engineers about possible critical situations.

Research question, objective & scope

To summarize, almost no research is available which covers the response of the cargo and sea-fastening system in relation to hydrodynamic-based loads encountered during transport. This is in contrast to the fact that research related to this behavior could be of great importance to the industry.

The trend of monopiles becoming more stiff and vulnerable as a result of their increasing diameter-to-thickness ratios emphasizes the need for research regarding this behavior. Insight into cargo responses helps to ensure safe transportation while preventing damage. This insight could contribute to a more optimized sea-fastening system, reducing transporting costs.

The research question is defined as follows, based on this identified knowledge gap:

"How does the interaction between a vessel and large, stiff cargo affect the structural dynamic behavior, considering the influence of non-linear constraints posed by sea-fastening?"

This research question is broken down into the following sub-questions:

1. In what manner can the interactions between the vessel and cargo be modeled using non-linear constraints imposed by the sea-fastening system?
2. How does the bending of the cargo contribute to additional loads experienced in the ship and sea-fastening system?
3. What is the influence of sea-fastening on the structural dynamic response of the cargo and sea-fastening and how can connection be ensured?
4. To what extent does non-linear modeling influence the observed response compared to a linear approach?

The main objective follows from the research question and is defined as follows:

"To create a numerically efficient model that defines the response of the cargo and sea-fastening system based on ship-induced loads"

It should be emphasized that an efficient model is important in this research. Due to the absence of other research and the variability of cargo and sea-fastening arrangements, it is valuable to be able to perform a vast amount of calculations. This enables the investigation of a large spectrum of this behavior, identifying cases where there is a significant change in dynamic behavior or load distribution. Types of analysis could be, but are not limited to, parametric studies or Monte Carlo analysis.

The research is focused on the MC-class vessels of BigLift. The parameters of these vessels are used as input in this research. It is expected that the results of this research can be extrapolated to other vessels, as long as the hull properties are similar. For hulls with open sections this research might not be representative.

Furthermore, this research focuses only on cargo relevant to heavy-lift shipping. Cranes, monopiles and topsides are examples of this. Within the modeling, no impact dynamics or mechanics are considered. The only relevant part is to define the situation and magnitude of disconnection of the cargo, not necessarily what happens afterward.

At last, only harmonic loads or excitation sources are considered in this research. This could be wave loads or propeller and engine vibrations. Impact loads such as slamming or whipping are not considered in this research. The identified solution method is not able to solve for transient behavior.

Thesis outline

At first, a brief summary of the literature review is presented in chapter 2. Note that this is a condensed version of the initial review, including only the elements relevant to the research that is presented. Chapter 3 describes the identified models and further elaborates on them. A different identified approach is discussed here as well. Chapter 4 describes the hydrodynamic model that is created and how its results serve as a loadcase for the structural model. The structural model is constructed using both linear and non-linear approaches, with details provided in chapter 5. This finalizes the modeling part, enabling to start the research, for which the results are presented in chapter 6. The results consist of the analysis of various cases and different parametric analyses, all of which are presented within this section. Finally, chapter 7 summarizes the conclusions and recommendations.

2

Literature review

This chapter discusses the relevant literature related to the identified solution method. Note that this is a summarized version of the original literature review, only literature that contributed to creating the model and obtaining results is discussed.

2.1. Description to-be-created model

A general outline of the to-be-constructed model can be defined based on the problem description. Figure 2.1 shows a schematic version of an MC-class vessel carrying a monopile. This figure shows that 2 sub-models are required to model the complete problem, being a structural model and a hydrodynamic model. Note that for these models the ship is the connection between the two models, since it is present in both the structural and hydrodynamic model.

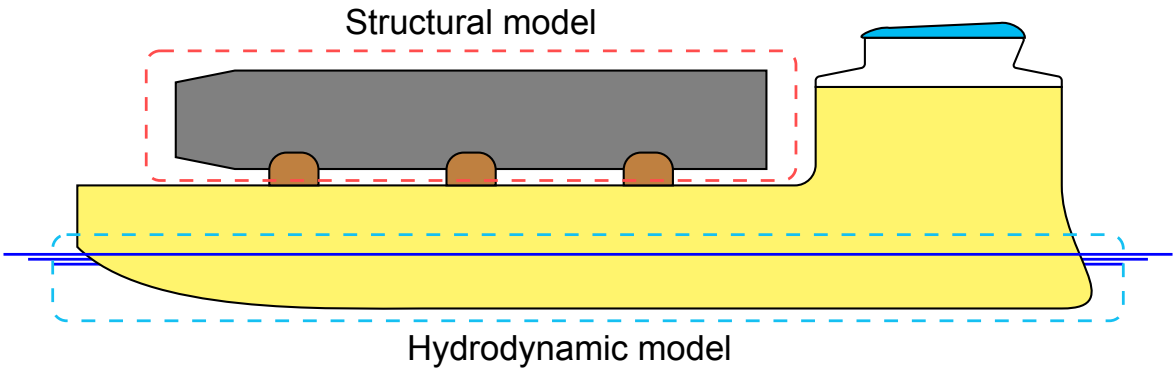

Figure 2.1: Distinguished sub-models required to analyse the total problem

At first, a broad understanding exists related to the hydrodynamic model. Various methods exist that define the dynamic behavior of a ship subjected to wave loads. Note that this dynamic behavior is used as input for the structural model, this defines the excitation. For the structural model this is not the case, here complexity is introduced non-linear elements in the sea-fastening system. These elements are described in further detail in section 2.2.2. Research is required on how the ship-cargo interactions can be defined when these objects are connected using non-linear elements. An investigation is made to determine how methods from different fields of study can be applied to solve for structural dynamics.

The identified sub-models and elements in the models will form the basis for this literature review. For all elements an analysis in the literature is made on how these can be modeled best. The analysis for both submodels ends with a conclusion where trade-offs are made if a choice exists between different models.

2.2. Definition of structural model

This paragraph describes the definition and approach applied to the structural model, as identified in figure 2.1. The desired functionality of this model is to define the structural and elasto-dynamic response of the ship, sea-fastening elements and cargo. Figure 2.2 shows an outline of this model. This figure shows that the structural model consists of 3 elements, being the ship, sea-fastening system and the cargo. In this figure an arbitrary set-up of the sea-fastening system is shown, represented by a spring, a unilateral spring and a rotational spring respectively. The sea-fastening system is expected to significantly influence the response, because here the forces and moments are exchanged by the ship and cargo.

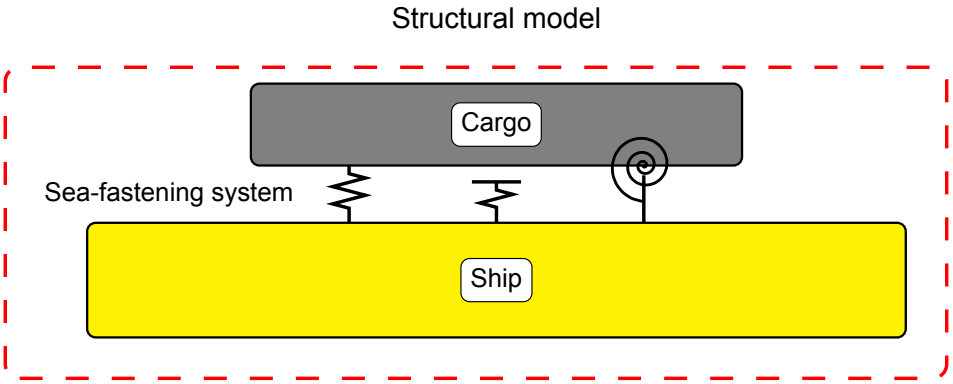

Figure 2.2: Identified elements in structural model

Based on this subdivision of elements separate analysis is performed on how these elements best can be modeled, taking the desired functionality into account. These analyses are presented in paragraphs 2.2.1 and 2.2.2.

2.2.1. Modeling of ship and cargo

Based on the dimensions shown in table 1.1 the conclusion can be drawn that the ship can be modeled as a beam. This is justified by the fact that the length is significantly larger than the width or height. Two different models with different properties are distinguished, these are Euler-Bernoulli and Timoshenko theory. These are the so-called classical models. Compared to each other, the Timoshenko is more extensive since it includes shear deformation [24, 25]. In general, the Euler-Bernoulli model is valid for homogeneous slender beams, while the Timoshenko model can be applied in the case of thick orthotropic beams as well.

The paper of Labuschagne shows that for higher modes, corresponding to higher eigenfrequencies, the effects of shear become important [24]. It shows that the Euler-Bernoulli model becomes invalid, with discrepancies of factor 4 compared to the eigenfrequencies defined by the FEM model. The results of the Timoshenko model are accurate compared to the FEM model, with differences less than 3% [25]. Therefore, for this thesis the ship is modeled as a Timoshenko beam.

Another important element to emphasize is the fact that the ship's hull is closed. This results in there being no coupling between torsional and horizontal bending [26]. Therefore, it is possible to model the ship in a 2D manner. Later on in the literature review this will be elaborated further.

For the cargo model the variability of the cargo is an important element. It might occur that some cargoes cannot be classified as slender, so, therefore, the more general Timoshenko theory is better suitable [24, 25].

2.2.2. Modeling of sea-fastening system's elements

Within heavy lift shipping, various sea-fastening arrangements are present. These arrangements function as the boundary conditions between the coupled ship-cargo system.

In practice, BigLift uses various types of structural elements to ensure sea-fastening. Examples of these are push-pull bars, shear plates and lashing wires. Elements of the sea fastening system are summarized with their properties in table 2.1. Combinations of these elements are used to ensure the sea-fastening of cargo elements. Note that for the lashing wire and saddles non-linear behavior can originate. In order to fully behave linearly, the component needs to be able to have the same reaction in tension or compression.

For shear plates and stoppers a different conclusion can be drawn. These elements are generally not used to provide tensile resistance in a sea-fastening arrangement. But when evaluating their force deflection properties the conclusion can be drawn that these elements can be modeled in a linear manner.

Table 2.1: Elements sea-fastening system used at BigLift and loads it can withstand

Element	Tension	Compression
Lashing wire/chain	✓	×
Saddle	×	✓
Shear plate	×	✓
Stoppers	×	✓
Push-pull bars	✓	✓

Lashing wire

The tension test of a steel wire showed that the load-strain relation is linear up to the point where yielding occurs [27]. Therefore, the lashing wire can be modeled as a linear spring, no nonlinearities are involved here. Note that in some cases this lashing wire can be applied with pre-tension as well.

Saddles

The saddles carry the weight of the monopiles and resist movement in port-starboard directions. In the longitudinal direction the movement is constrained by friction forces and lashing wires. Here, nonlinearities can originate. Literature shows that if both static and dynamic friction are taken into account in dynamic analysis, the friction force becomes a non-linear function of the velocity [28]. This would be present in cases where saddles are used.

This friction would be a damping factor since it always counteracts the velocity. Various models could be applied, from which Coulomb friction would be the simplest [29]. Later in the research, an analysis should be made to determine the influence of friction on the coupled dynamics.

Shear plates, push-pull bars, stoppers

These sea-fastening elements completely restrict movement in certain directions. If these are applied all together, a pinned or rotationally restrained boundary condition can be assumed. For the push-pull bars it should be noted that these distribute the load on a larger part of the vessel. Figure 2.3 shows an example of how these elements are applied within the sea-fastening systems at BigLift.

Figure 2.3: Usage of shear plates and push-pull bars in the sea-fastening system on the MC-class vessels

Multi-body contact problem

Based on knowledge from practice from BigLift and previous research, the case shown in figure 2.4 is distinguished. This shows the lashing system used for monopiles, consisting of lashing wires and saddles. The lashing wires are depicted as springs in this figure, and it is assumed that some form of pretension is applied. The saddles are represented by the boxes present between the monopile and the ship.

Using a linear solver does not allow for separation between the monopile and contact points [15]. Therefore, the problem could be overconstrained, leading to incorrect load transfers from and to the monopiles. This research should investigate to what extent linear modeling influences the results.

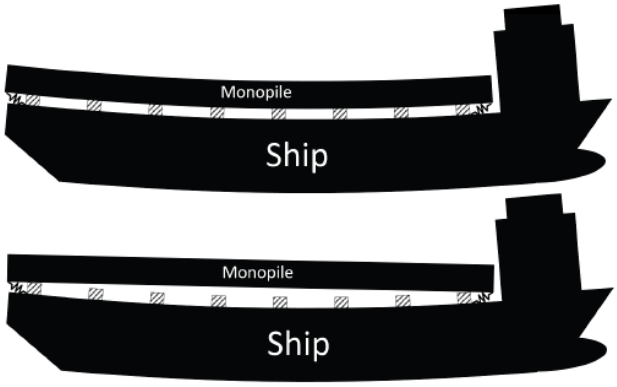

Figure 2.4: Constraints applied to monopiles in [15]

This leads to the conclusion that the utilized model should enable the use of non-linear constraints, to ensure that friction and the multi-body contact problem can be handled.

Furthermore, the sea-fastening elements cause discontinuities in the to-be-created model. Therefore, the problem cannot be solved with an analytical solution. A model needs to be created that takes all boundary conditions into account, using beam theory and solving it using a system of equations.

2.2.3. Elasto-dynamic model

This section describes the model required to define the response for a given load. The domain of elastodynamics covers how materials deform and respond for a dynamic load. Due to the oscillatory nature of wave loads, vibrations are relevant. Further details on wave loads are described in section 2.3. In addition, several other vibration sources such as engines and propellers are also present on board a vessel. First, some basic models are discussed to obtain general knowledge. These models are relevant in case no non-linear boundary conditions are used in the structural interface. After that, more sophisticated methods are discussed, which are able to solve the multi-body contact problem. Attention is paid to the non-linear boundary conditions.

Analytical solution

When considering vibration dynamics, equation 2.1 is defined as the governing equation for Euler-Bernoulli beams. This equation is derived from the force equilibrium in the y-direction, which is perpendicular to the length of the beam [30]. Coordinate x is in the length direction of the beam. In this equation parameter ρA is defined as the mass per unit length. Parameter E is defined as the Young's modulus and parameter I as the area moment of inertia. Finally, p is defined as the applied load, as a function of position and time.

$$\rho A \frac{\partial^2 y}{\partial t^2} + \frac{\partial^2}{\partial x^2}\left(EI(x)\frac{\partial^2 y}{\partial x^2}\right) = p(x,t) \tag{2.1}$$

Solving this equation for a homogeneous beam without an applied load result in certain eigenmodes and eigenfrequencies. This solution would be a continuous analytical solution. These modes and

frequencies are defined by the boundary conditions of the problem.

For Timoshenko beams, equation 2.2 represents differential equations [31, 32]. These result from the force and moment equilibrium for an infinitesimal small element. Here, the angle ψ represents the rotation of the plane perpendicular to the neutral axis due to shear, while the angle γ is the angle caused by pure bending. Parameter k is the Timoshenko shear coefficient. All other parameters in this equation have the same definition as in equation 2.1.

$$\begin{aligned} -kGA\frac{\partial\gamma(x,t)}{\partial x} + \rho A\frac{\partial^2 y(x,t)}{\partial t^2} &= p(x,t) \\ -EI(x)\frac{\partial^2\psi(x,t)}{\partial x^2} + kGA\gamma(x,t) - I(x)\rho\frac{\partial^2\psi(x,t)}{\partial t^2} &= 0 \end{aligned} \tag{2.2}$$

Note that no analytical solution exists for Timoshenko beams. These governing equations are used in the derivation of the stiffness matrix for a FEM model [33].

Finite element solution

Two main modeling techniques exist, being [34]:

- Mesoscale-based: Lattice element model
- Continuum-based: Finite element model

Mesoscale models are able to incorporate complex properties of materials, like disorders, quasi-brittleness and fracture [34]. Bolander states that this type of modeling should be applied in case of severe inelastic processes [35]. For example, in [36] the lattice element method is used to model the dynamics of a cracked beam.

Continuum models provide an efficient solution method for homogeneous elastic structural problems [35]. It is known that the material properties in this research will vary as continuous functions, so therefore a continuum approach is valid. Yielding, cracks or other strong discontinuous processes are not considered in this research. Note that in this approach, the assumption is made that rotations and strains remain small [37].

Figure 2.5 shows the discretization of the system shown in figure 2.1 in the normal mode method. Here, the distributed mass of the ship is discretized into a finite number of elements. The top masses are defined by the cargo, connected by beams to incorporate its stiffness. Extensive literature is present to define Timoshenko beam elements in a finite element method [38, 39]. Note that cubic interpolation for displacement and quadratic interpolation for rotation must be used to prevent the effect of shear locking [40]. This research will be used to construct the model.

The bottom part of the figure shows the hydrodynamic restoring stiffness and hydrodynamic damping represented by springs and dampers respectively. The hydrodynamic added mass is accounted for in the mass at the nodes. At last, the hydrodynamic loads can be considered to be distributed over the hull.

Note that, as mentioned earlier, this problem is modeled in 2D. Because of the low bending-torsion coupling, it is expected that this does not have a significant influence on the bending dynamics.

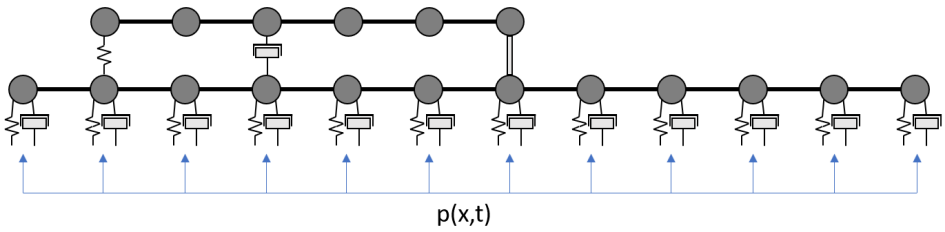

Figure 2.5: Discretization of ship-cargo-fluid system using the finite element method. The boundary conditions are the same as defined in figure 2.1.

This discretization shown in figure 2.5 is performed in order to use the normal mode method [30, 41]. In case of a linear analysis, two important properties can be distinguished [41]:

- Invariance: if a motion is excited on a certain mode, the others stay limited
- Modal superposition: individual motions of free and forced oscillations can be super-imposed.

By using the aforementioned properties, linear algebra and orthogonality relations, the eigenmodes and eigenfrequencies can be defined for multi-degree of freedom systems. Using this, frequency-response spectra can be obtained.

Non-linear solution

Although the properties of linear systems are convenient, this method is not able to model the complex behavior expected due to the non-linear constraints. For this reason, the non-linear normal mode method is proposed by Rosenberg [42, 43]. Rosenberg defines a non-linear normal mode as a vibration in unison, which implies that all discretized points reach their maxima and pass through zero at the same time instant [43].

An additional definition is presented by Shaw and Pierre, who define a non-linear normal mode as a two-dimensional invariant manifold in phase space. This approach makes the analysis possible for non-conservative systems [44, 45]. Three key properties that distinguish non-linear normal modes from their linear counterparts are [41]:

- Frequency–energy dependence: the shape of the frequency response spectrum depends on excitation energy
- Modal interactions: Non-linear Normal Modes (NNMs) can experience internal resonance, which implies an internal energy exchange between modes
- Mode bifurcations: within the frequency-response spectrum multiple responses for the same excitation frequency can be found

The frequency-energy dependence is shown mathematically in equation 2.3 [46]. This implies that both the mode shape ψ_s and corresponding eigenfrequency ω_s depend on the excitation amplitude a. Appendix A shows an example of this behavior, compared to its linear counterpart.

$$\begin{aligned} \psi_s &= \psi(x, a) \\ \omega_s &= \omega(a) \\ s &= 1, 2, \dots \end{aligned} \tag{2.3}$$

Regarding the modal interactions and mode bifurcations an example is shown in appendix B. This example shows that internal resonances cause bifurcations and it shows the energy exchange between different modes. Note that not all non-linear normal modes are stable, and therefore, these cannot be represented physically. So, not all branches shown in appendix B are stable, in reality this would be observed as a rapid change in energy. For instance, exciting a high-frequency mode could lead to a large response in a low-frequency mode [41]. Another important property is that at a low energy level, the non-linear normal mode is equal to the linear normal mode. Various methods use this property to make an initial guess for further calculations.

Equation of motion

Equation 2.4 shows a non-linear equation of motion, for a multi-body system [47]. In this equation **M** represents the mass matrix, **K** the stiffness matrix, $\mathbf{g}_{nl}$ the non-linear stiffness and damping vector and $\mathbf{f}_{nl}$ the time dependent excitation vector. This equation is then solved for the displacement vector **x**, which represents the lumped mass degree of freedom.

$$\mathbf{M}\ddot{\mathbf{x}} + \mathbf{C}\dot{\mathbf{x}} + \mathbf{K}\mathbf{x} + \mathbf{g}_{nl}\{\mathbf{x}, \dot{\mathbf{x}}\} = \mathbf{f}_{nl}\{\mathbf{x}, \dot{\mathbf{x}}, t\} \tag{2.4}$$

Note that this equation can be transformed into a first order differential equation by using the state vector $\mathbf{z} = \{\mathbf{x}, \dot{\mathbf{x}}\}$ [47]. The main limitation compared to the linear normal mode method is, at first, that the principle of superposition does not hold anymore. Therefore, the problem cannot be transformed into an eigenvalue problem. Another complication is that orthogonality relations, for example between eigenmodes, are also limited [41]. Therefore, solutions are more complex to derive.

In this case, the solution should be specified for discrete systems, in order to account for the discontinuities between the cargo and ship model. In addition, due to the possible case of damping by friction, the system becomes non-conservative. Complex behavior arises when friction is taken into account, numerous and complex bifurcations are present for these systems [48].

Figure 2.6 shows an example of bifurcations for an arbitrary system in a frequency response plot. In this figure, *cons.* is an abbreviation of conservative. This behavior needs to be accounted for in the solution method, since the dashed line is an unstable situation, but part of the solution of the non-linear differential equation. Therefore, a solution method must be able to identify both responses X_1 for a given excitation frequency Ω.

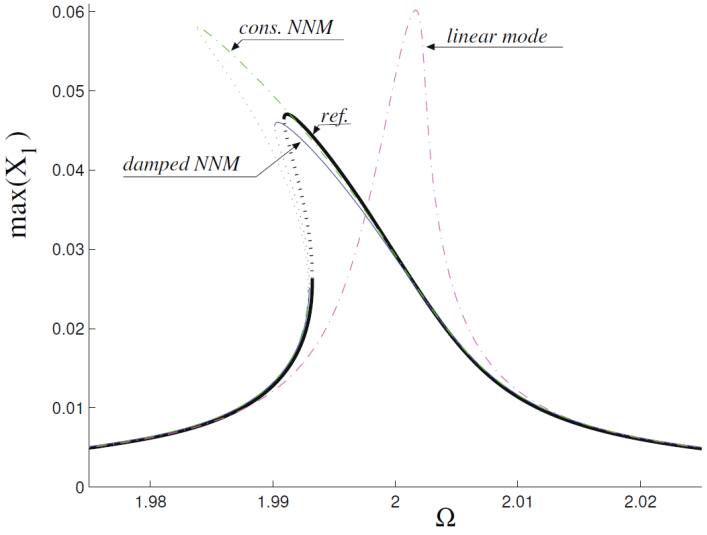

Figure 2.6: Example of bifurcation in non linear normal mode systems [49]

When considering analytical solution techniques the major advantage is that symbolical solutions provide insight and are useful for parametric studies. But, on the contrary, for complex multi-body systems these solutions get rather long and complicated. Other drawbacks are that the dynamics is only accurate for small amplitudes and that the results are inaccurate for strong nonlinearities [41]. Furthermore, [48] states that for damped systems no analytical solution can be found. The modes found in an analytical manner can only serve as a basis for the damped case, but when the system becomes moderately non-linear numerical methods become the only solution.

Shooting method & Pseudo-arclength continuation

A numerical method for non-linear systems is presented by Peeters et al. [50]. They proposed to use a so called shooting method in combination with Pseudo-arclength continuation. The shooting method provides a solution for the equation of motion, while the pseudo-arclength continuation ensures that bifurcations are handled correctly. Equation 2.5 shows the shooting function **H**, which represents the difference between initial conditions and the response at time T [50]. Note that this time T represents the eigenfrequency of the normal mode. This implies that this is a check if the displacement $\mathbf{z_p}$ repeats.

$$\mathbf{H}\left(\mathbf{z}_{p0}, T\right) \equiv \mathbf{z}_p\left(T, \mathbf{z}_{p0}\right) - \mathbf{z}_{p0} = \mathbf{0} \tag{2.5}$$

Figure 2.7 shows an example of the iteration performed by the solver, in this figure 4 steps are shown. This figure shows that for the final iteration the starting point at $t = 0$ is almost equal to the endpoint

$t = T$. This indicates an oscillation with period T, making it a solution of equation 2.5.

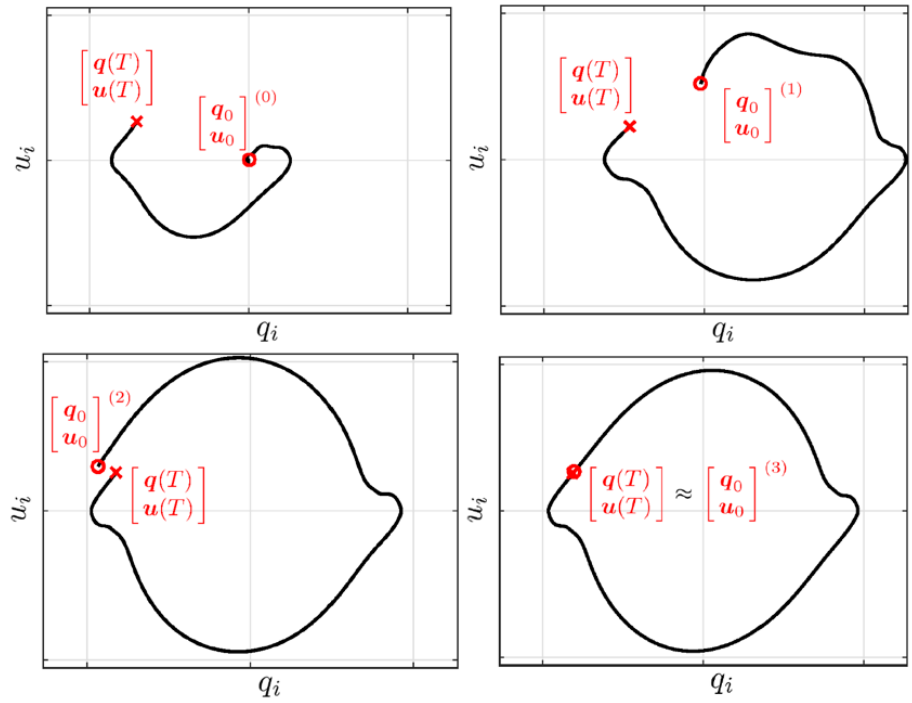

Figure 2.7: Example iterations of shooting method [51]

This method is based on direct numerical time integration. An example of a numerical procedure used in combination with the shooting method is shown in appendix C. In this procedure the direct time integration is used in combination with the Newton-Raphson algorithm. Note that this solution method is performed in time-domain.

A graphical representation of the Pseudo-arclength continuation is shown in figure 2.8. In this figure the predictor step is shown with the arrow, while the corrector step is shown in the dots. Using this method the solution is able to include bifurcations.

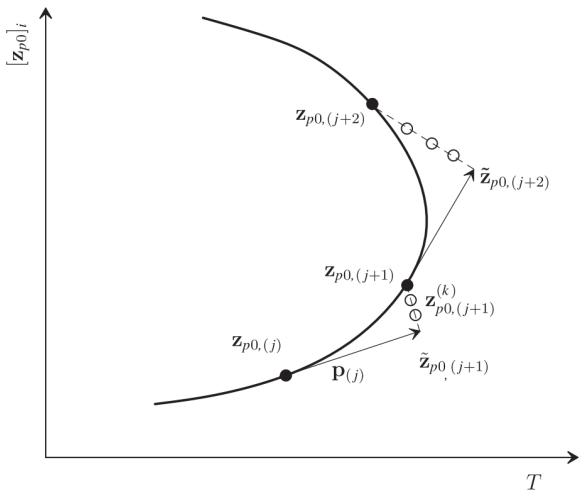

Figure 2.8: Pseudo-arclength continuation procedure for mode shape z_{p0} and eigenperiod T_j [50]

To summarize, key properties of the Shooting method are [50, 52]:

- Time-domain method, therefore able to model transient behavior

- Infeasible for large number of degrees of freedom
- Can handle strong nonlinearities accurately (friction, impact laws)

Harmonic Balance Method & Asymptotic Numerical Method

This method focuses on finding harmonic solutions for a system that is loaded periodically [51, 53]. The method could be especially of importance, as wave loads can be considered harmonic [54]. Equation 2.6 shows the differential equation system used as an example in the HB method. Here, the solution Y is assumed to be a truncated Fourier series, with a certain selected harmonic index k. This solution is implemented in the differential equation system, and then terms with a different Fourier index are dropped [53].

$$Y(t) = Y_0 + \sum_{k=1}^{H} Y_{c,k} \cos k\omega t + \sum_{k=1}^{H} Y_{s,k} \sin k\omega t \tag{2.6}$$

Note that for the non-linear case this method only yields an approximation, which converges to the exact solution if the truncation is increased to infinity [51]. When the nonlinearities are of simple polynomial form, an analytical approximation could be found. In case of more complicated nonlinearities, numerical methods should be applied. One major advantage is that the problem is solved in frequency domain. This results in the reduction of several orders of magnitude of required calculations compared to time domain analysis. Figure 2.9 shows why solving in the frequency domain for a steady-state solution is more efficient compared to the time domain. This figure also emphasizes the fact that the HB method can only be applied to the steady-state solution.

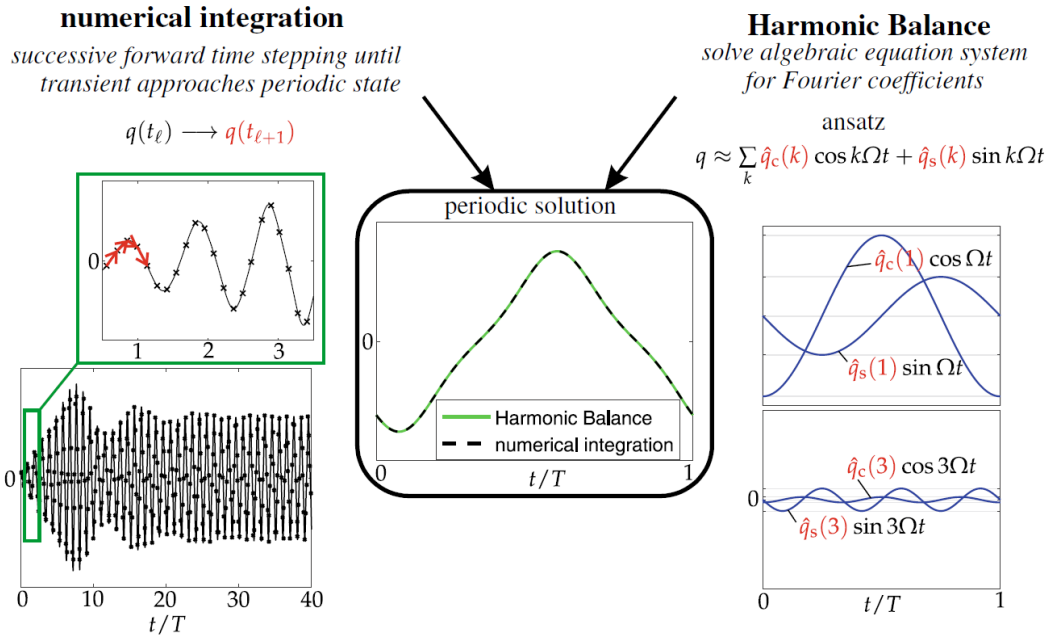

Figure 2.9: Numerical integration versus Harmonic Balance [51]

Three different algorithms are distinguished in [51].

1. Polynomial non-linear forces: solve for closed form expression.
2. For piecewise polynomial forces: determine transition times, proceed as in 1.
3. Generic non-linear forces: apply Alternating Frequency-Time (AFT) scheme

It is expected that for this situation algorithm 2 needs to be applied. This is because in the multi-body contact problem, the impact can be modeled as a unilateral spring with high stiffness. It is expected that in case of friction, it can be modeled using a polynomial description. This is then solved in algorithm 1. The Alternating Frequency-Time algorithm is discussed in the next paragraph.

In this approach, the HB method is used to solve the equation of motion and the Asymptotic Numerical Method is used to handle the bifurcation problem. The asymptotic numerical method starts by performing a Taylor expansion on the solutions found, as shown in equation 2.7. This method enables branch following, which is useful when handling bifurcation behavior. Figure 2.10 shows an example of how this method follows a branch. Note that the starting point of these solution methods is at a low energy or frequency, where the behavior can still be assumed to be linear.

$$\mathbf{U}(a) = \mathbf{U_0} + a^2\mathbf{U_1} + a^2\mathbf{U_2} + \cdots + a^N\mathbf{U_N} \tag{2.7}$$

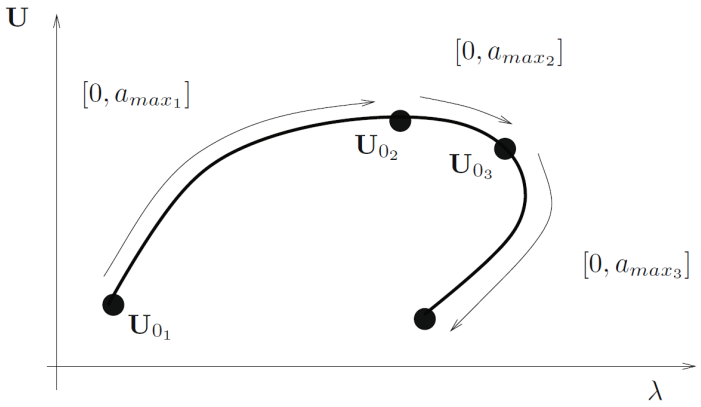

Figure 2.10: Asymptotic numerical method applied on solutions **U** [53]

In [55] a situation is analyzed in which a non-smooth impact force is considered of a U-tube with support plates. Figure 2.11 shows the considered situation with the simplified situation to a two degree of freedom system. This problem is solved using the HBM-ANM algorithm. Again, this example will be useful in order to handle the multi-body contact problem.

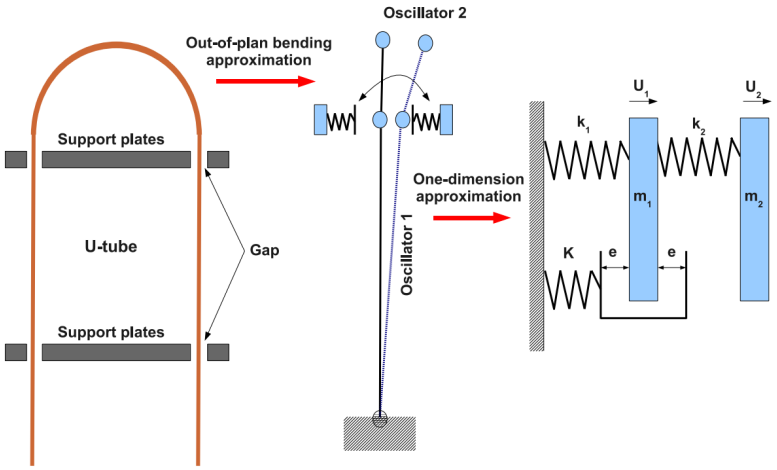

Figure 2.11: U-tube with discretization to 2 degree of freedom system [55]

Note that the Harmonic Balance Method can only fully be applied if the system can be decomposed into a piecewise linear system, as shown in [55]. There they were able to decompose the system into 4 different timesteps, for which they could derive 4 different linear equations of motion.

For the Harmonic Balance Method the main properties are [51, 52]:

- Frequency-domain method, so high numerical efficiency compared to time domain methods
- Only steady state behavior can be modeled, no non-periodic processes
- Not able to model strong nonlinearities

Alternating frequency time-domain harmonic balance method

Some time-frequency domain methods exist as well. These methods try to combine both the strong properties of the time and frequency domain methods by switching between them. A summary of the Alternating Frequency-Time (AFT) method is shown in figure 2.12. The non-linear force is evaluated in time domain and after that the Fourier coefficients are computed for this force [52].

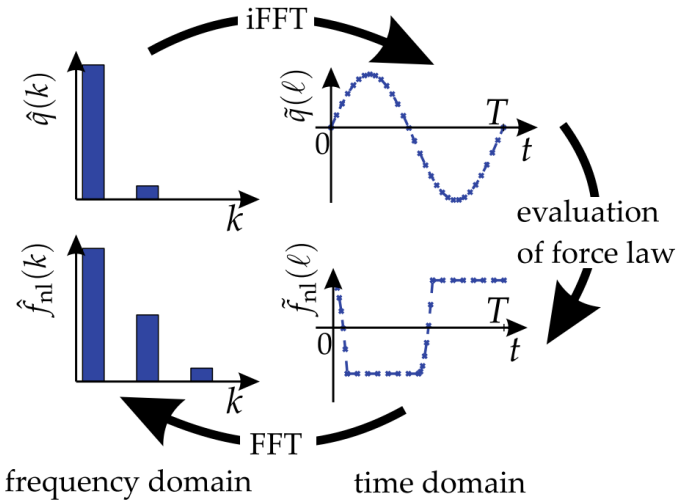

Figure 2.12: Alternating Frequency-Time domain scheme. The non-linear force $\mathbf{f_{nl}}$ is defined in time domain, using the displacement $\mathbf{q_l}$ [51]

The main difference between the AFT-HBM and HBM is how the weighted residual is handled. As stated by Krack: *"Harmonic Balance requires that the Fourier coefficients of the residual vanish, up to the truncation order, H, of the ansatz"* [51]. Equation 2.8 shows the requirement for weighted residual **r**, and the solution for the HB and AFT-HB method. In this equation, $\mathbf{h_H}$ and $\mathbf{h_H^*}$ are defined as the matrices of Fourier series and coefficients, respectively. Within the HB method, Galerkin's method is applied using the fact that the residual is orthogonal to the Fourier series, as shown in 2.8. In the AFT method this method is applied using Inverse and Forward Fourier transforms, denoted by $\mathbf{E_{HN}}$ and $\mathbf{E_{HN}^*}$ respectively.

$$\begin{aligned} \text{HB: } \hat{\mathbf{r}}_H\left(\hat{\mathbf{y}}_H\right) &= \frac{1}{T}\int_0^T \mathbf{h}_H^*(\Omega t)\mathbf{r}\left(\mathbf{h}_H(\Omega t)\hat{\mathbf{y}}_H, \mathbf{h}_H(\Omega t)\Omega\nabla\hat{\mathbf{y}}_H, t\right)\mathrm{d}t = \mathbf{0} \\ \text{AFT: } \hat{\mathbf{r}}_H\left(\hat{\mathbf{y}}_H\right) &= \mathbf{E}_{HN}^*\tilde{\mathbf{r}}_N\left(\mathbf{E}_{NH}\hat{\mathbf{y}}_H, \mathbf{E}_{NH}\Omega\nabla\hat{\mathbf{y}}_H\right) = \mathbf{0} \end{aligned} \tag{2.8}$$

Mixed Shooting - Harmonic Balance Method

In [52] a mixed shooting-harmonic balance method is proposed. This method is able to handle non-smooth contact laws as well. The results are in accordance with the results based on a purely shooting method. By combining these 2 methods, the extensiveness of the time-domain and the efficiency of frequency-domain are used. Figure 2.13 shows a comparison for an MS-HB and HB method. This figure shows that for severe stick-slip behavior, the force of the HB method is represented incorrectly.

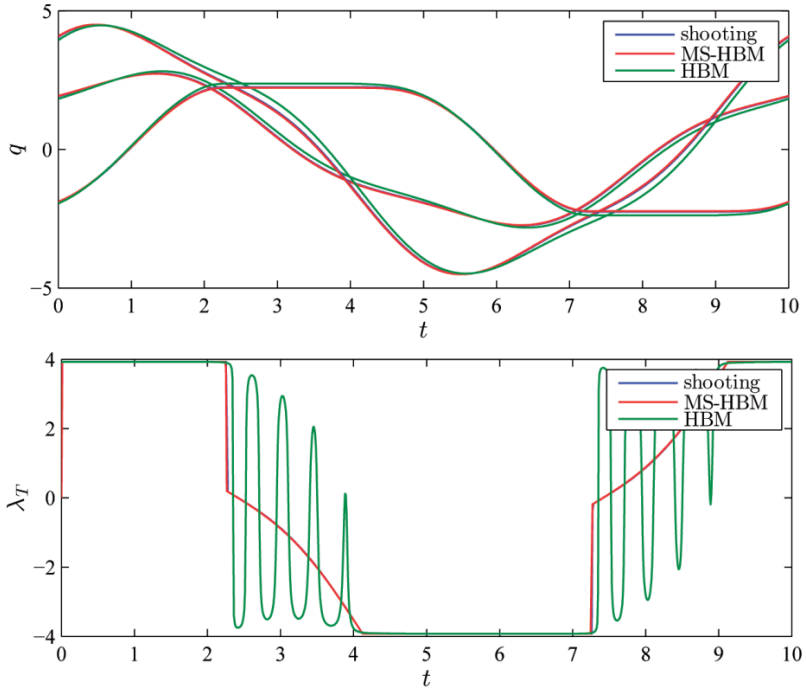

Figure 2.13: Comparison between MS-HBM and HBM method [52]

Appendix D shows an example of the numerical procedure followed in the Mixed Shooting - Harmonic Balance method.

2.2.4. Modeling of non-linear constraints

Now that the different solutions methodologies have been distinguished, further research is carried out on the different constraints. In section 2.2 two different non-linear constraints are distinguished, being the unilateral saddle constraint and the friction constraint. Both are discussed in this paragraph.

Detachment of saddles

As mentioned earlier, and shown in figure 2.4, the situation might occur that the monopile becomes disconnected from the saddles. This means that the saddles must be modeled as a unilateral constraint. This type of constraint allows for free movement in one direction, but limits it in the other [56].

Impact dynamics describes that complete disconnection and its return are characterized by short duration, high forces, fast dissipation of energy and high accelerations [57]. During an impact, a part of the energy is transferred into waves of deformation and strain, resulting in vibrations. This emphasizes that this behavior should be prevented during transport.

Some assumptions are made regarding the detachment of the monopiles:

- Impact dynamics and mechanics are not considered
- Saddles are modeled with finite stiffness, resulting in an initial compressive deflection
- The speed of the pile will be equal to the speed of the saddle if it connects again

The first element is neglected in this research because it is not relevant in this case. This study needs to define whether the monopile detaches and, if so, the order of magnitude of the detachment. What happens during and after impact of the monopile is not relevant in this case, because this research is focused only on identifying the situations of detachment. This implies that fields like plasticity, restitution coefficients and vibration due to impacts are not considered.

The initial compressive deflection results in contact preservation when the monopile is excited in higher-order modes. It is known that when the order of the bending mode increases, the deflections

resulting from this mode become significantly smaller. Therefore, these higher-order deflections will be smaller than the initial deflection caused by the weight and pretension, ensuring connection between the monopiles and saddles.

Finally, when the monopile is detached and touches the saddle again, it is assumed that the speed of the monopile is equal to the speed of the saddle again. This should be the case for small and momentarily disconnections.

Regularization of contact force

The earlier mentioned paper of Moussi et al. [55] solves the unilateral constraint using a regularization technique. Equation 2.9 shows the piecewise linear spring force, as a result of the configuration shown in figure 2.11. Parameter K represents the stiffness of the spring, U the displacement, and e the initial gap between the element and the spring.

$$F(U) = \begin{cases} K(U-e) & \text{if } e \leq U \\ 0 & \text{if } -e \leq U \leq e \\ K(U+e) & \text{if } U \leq -e \end{cases} \tag{2.9}$$

This function can be defined using an implicit polynomial, shown in equation 2.10. This function approaches the piecewise function from equation 2.9. Function $f(x;\alpha,\eta)$ can be derived from this function, and implemented into the equations of motion.

$$f(f-\alpha(x-1))(f-\alpha(x+1)) + \eta\alpha^2 x = 0 \tag{2.10}$$

Figure 2.14 shows the result of the regularization. For smaller values of η, the regularization approaches the piecewise linear function. By performing this regularization, the HBM is still able to solve the differential equations.

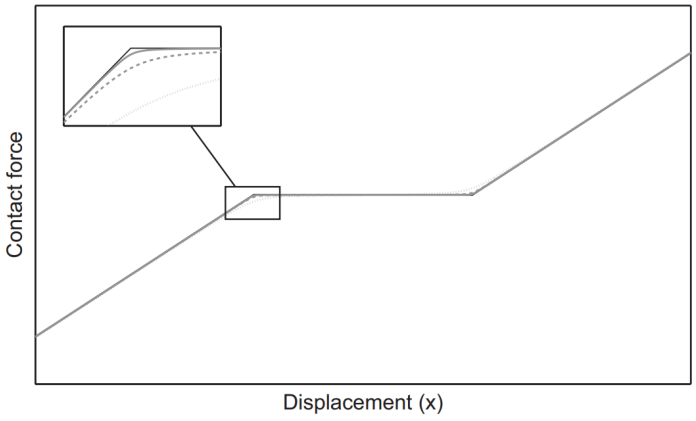

Figure 2.14: Regularization of non-smooth spring force [55]

2.2.5. Finite Element Modeling software

The problem considered in this literature review can be solved as well using Finite Element Modeling software. FEM is used to subdivide complex structures into smaller elements, which are connected by means of the beam, plate, shell or solid equations [58]. These equations of all smaller elements are then connected to each other using boundary conditions. This is the method behind the discretization shown in figure 2.5.

As shown in the book 'Non-linear Finite Element Analysis of Solids and Structures', the most common method that a commercial FEM package applies is a time domain method [59]. Different types of solvers are defined as implicit, explicit and energy conserving time integration methods. The thesis of Mikail states that performing non-linear FEM analysis is time intensive [15]. Although the model consisted only of a limited amount of beams and springs, the analysis time was still extensive.

In addition to the long computation time, some other potential troubles can also be identified. Using FEM packages results in complex postprocessing, limited by the tools presented. In addition, using these programs can give mathematical problems with respect to convergence and stability [60]. This research also states that reduced-order models reduce the computational problems.

Finally, the researcher wants to obtain a thorough understanding of the phenomena regarding this problem. This understanding is strongly enlarged by creating a finite element model in, for example, Python or Matlab. Using a FEM package, the solution method could remain ambiguous, leading to a false interpretation of the results.

Note that FEM packages could be valuable to verify the created model. This will be the primary method of verification, since comparable research is limited.

2.2.6. Conclusion

This section discussed the different models that are relevant when defining the structural and elastodynamic response within the structural model. The need for a discretization method and some non-linear boundary conditions are identified. Various different solution methods are found to solve this non-linear problem, of which a selection is made.

Based on current knowledge, the preferred method is to solve the systems response using the Harmonic Balance Method. The nonlinearities are handled using regularization techniques. The main driver of this choice is the oscillatory nature of the wave loads and the computational efficiency of this method. By creating an efficient model in Python or Matlab, the researcher has the freedom to perform parametric studies and thoroughly investigate the behavior of the system.

2.3. Definition of hydrodynamic model

This section considers the hydrodynamic part of the problem. In this section, an overview of current models applied to define the fluid-structure interaction is provided. This is reviewed in light of the properties of the structural model, to ensure that these models are compatible with each other. Note that the hydrodynamic part provides the excitation for the structural model.

Based on figure 2.1 three important elements can be defined, the ship, the fluid and the hydrodynamic interface between the two. These elements are highlighted in figure 2.15. All three are analyzed in this section, concluding with the modeling approach.

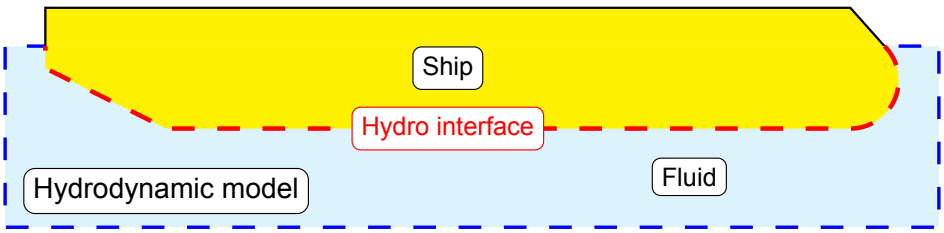

Figure 2.15: Distinguished sub-models required to analyse the total problem

2.3.1. Modeling of ship

In general, there are two approaches to analyzing the hydrodynamic loads acting on a vessel. These consist of a rigid body and a hydro-elastic approach. The rigid body approach is briefly discussed in this paragraph.

Rigid body approach

In the majority of hydrodynamic analysis, a rigid body is assumed. Programs used in industry like WAMIT, NEMOH and HAMS assume this approach, which provides fast and accurate predictions of hydrodynamic loads [61]. This type of modeling can only be applied in cases where the structural deflections due to the hydrodynamic forces of the body are limited. This approach is also referred as a one-way coupling analysis.

It is expected that due to the limited size of the vessel, and its closed hull, a rigid body approach is sufficient. This because no eigenfrequencies of the vessel will be excited based on hydrodynamic loads. Note that this also implies that the motion response amplitude operators are not affected by stiff cargo. The contribution of stiff cargo incorporated in the vessel stiffness even implies that the vessel becomes more stiff, further justifying a rigid body approach. Hydro-elastic behavior and the regions of interest are kept in mind throughout the research, especially when the eigenfrequencies approach the exciting frequency.

2.3.2. Modeling of fluid

Within the field of hydrodynamic analysis for large vessels, the most widely applied fluid model is potential theory [26, 62, 63]. This theory assumes that the fluid is irrotational and incompressible. The definition of the velocity potential Φ is shown in equation 2.11.

$$\begin{aligned} \mathbf{u} &= \boldsymbol{\nabla}\Phi \\ \boldsymbol{\nabla} &= \left[\frac{\partial}{\partial x}, \frac{\partial}{\partial y}, \frac{\partial}{\partial z}\right] \end{aligned} \tag{2.11}$$

The undisturbed wave potential can be derived using Laplace's equation, in combination with 3 boundary conditions. These boundary conditions are the impenetrability of the seabed, the dynamic and the kinematic boundary condition of the free surface. Equation 2.12 shows the general velocity potential together with the dispersion relation. In this equation ζ_a represents the wave amplitude. Parameters g and ω represent the acceleration due to gravity, and the frequency. The wave number is represented by k, the water depth by h and the position in the water by z. At last, parameter μ represents the wave direction. The dispersion relation follows from the kinematic boundary condition, and can be used to simplify the potential for shallow and deep water conditions.

$$\begin{aligned} \Phi(x, y, z, t) &= \frac{\zeta_a g}{\omega} \cdot \frac{\cosh(k(h+z))}{\cosh(kh)} \cdot \sin(kx\cos\mu + ky\sin\mu - \omega t) \\ \omega^2 &= kg\tanh kh \end{aligned} \tag{2.12}$$

2.3.3. Modeling of hydrodynamic interface

When ships show dynamic behavior in a fluid, certain elements come into existence at the interface. Examples of this are added mass **A**, hydrodynamic damping **B** and restoring stiffness **C**. In figure 2.5 this damping and stiffness is represented by dampers and springs at the bottom of the lumped mass model. These parameters are defined using matrices since they have different values for different motion directions.

Added mass is defined as the inertia of water that interacts with the vessel's hull in a dynamic state [64]. This contribution is always positive to the mass or inertia moment, resulting in lower accelerations.

Hydrodynamic damping is defined as the out-of-phase force with velocity [63]. This force is caused by waves that dissipate energy, and viscous effects such as skin friction and turbulence [65]. Note that, due to the assumption of inviscid flow, the effects of skin friction and turbulence are neglected. This type of flow can only take radiation from waves into account. The viscous part of damping is only significant for surge and roll motions, for the other motions the dissipated waves contribute most to damping [66]. Sarpkaya states that there are no numerical models that can be used at an industrial level [63]. Therefore, if the accuracy of the damping coefficients is important, empirical methods should be applied.

The restoring stiffness is defined by the stability and force balance of the vessel. This restoring stiffness coefficient is only present for the heave, roll and pitch motions [65]. Note that this restoring stiffness is a geometric parameter.

2.3.4. Hydrodynamic analysis method

Comparable to the non-linear normal modes, the solution methods for potential flow theory can be distinguished in time and frequency domain methods [67]. Time domain solvers are able to handle

transient behavior, while frequency domain methods are able to solve for periodic steady state solutions.

This research focuses primarily on the response of the vessel in regular and irregular waves. These waves consist of a linear wave or a superposition of linear waves. Therefore, a frequency domain description is sufficient.

Radiation - Diffraction theory

Within marine engineering, a widely used approach to define hydrodynamic loads on a floating object is governed by radiation-diffraction theory [65, 68, 69]. Equation 2.13 shows the identified potential consisting of the incoming Φ_w, diffraction Φ_d and radiation Φ_r potentials. Incoming and diffracted waves are represented by the potential shown in equation 2.12. The diffracted wave potential represents the diffraction of waves due to the presence of an obstacle, representing an exciting force as well.

The radiation potentials describe waves generated by a body as a result of its movement in a certain direction. Therefore, there are six radiation potentials, one for every degree of freedom. This potential is a function of the vessel's acceleration and velocity and is a resultant force. This implies that it is only present if the vessel is in motion.

$$\Phi(x, y, z, t) = \Phi_w + \Phi_d + \Phi_r \tag{2.13}$$

The pressures can be defined using the linearized Bernoulli equation, which leads to the forces and moments acting on the vessel. After some mathematical derivation, equation 2.14 can be found, it represents the equation of motion for floating vessels. The incoming and diffracted wave potential lead to the Froude-Krilov $\mathbf{F}_{FK}$ and Diffraction $\mathbf{F}_D$ forces, defined as exciting forces. The radiation forces are resultant forces of motion and are accounted for in the added mass **A** and damping matrix **B**.

$$[\mathbf{M} + \mathbf{A}]\,\ddot{\mathbf{x}} + \mathbf{B}\dot{\mathbf{x}} + \mathbf{C}\mathbf{x} = \mathbf{F}_{FK} + \mathbf{F}_D \tag{2.14}$$

Since the excitation force $\mathbf{F_{FK}}$ and $\mathbf{F_D}$ is harmonic, it is reasonable to assume that the response **x** is harmonic as well. By doing this, the response amplitude operators (RAO's) of a vessel can be defined. The RAO's is defined as the ratio between the motion amplitude x_a and the excitation amplitude ζ_a.

Numerical methods

Various different methods can be distinguished to solve the different forces and motions. Note that a numerical method is required in these types of problems, due to the geometrical complexity of ships. In general, 2 different theories are used to solve the equation of motion and the complex geometry.

At first, strip theory was proposed by Tuck and Faltinsen in 1970 [70]. Figure 2.16 shows an example of the discretization made in strip theory. The hydrodynamic properties are defined per strip, assuming that it is infinitely long. Due to this assumption, it is only valid for long and slender bodies [65]. Certain 3D interaction effects cannot be modeled as well, since all strips are computed independently of each other.

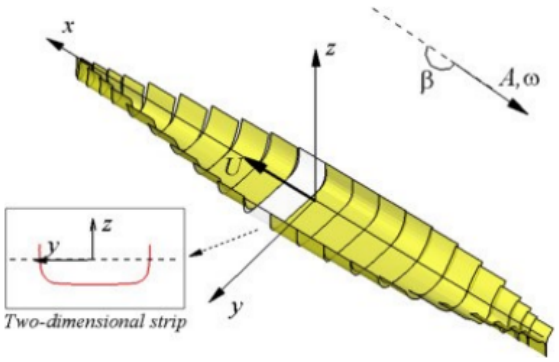

Figure 2.16: Strip theory discretization hydrodynamic analysis [71]

The other method widely used is the boundary element method [69]. In this method the hull is discretized in a certain number of panels, for which a no penetration boundary condition is applied. This is a fully 3D method and an example of program which uses this type of analysis is DELFRAC or WASIM. For heavy-lift transport, BigLift uses the frequency-domain program WASIM. Within this method, the Greens function is used to comply with Laplace's equation.

When both methods are compared, the conclusion can be drawn that the panel method has superior accuracy over strip theory [72]. Hsiung showed in his paper that strip theory overpredicts ship motions in general and that inaccuracy is especially present for the pitch motion. Note that although this observation is made, the strip theory should be kept in mind for its numerical efficiency.

2.3.5. Conclusion

This section described different models relevant for a ship's hydrodynamic analysis. The conclusion can be drawn that for this case, a rigid body approach is sufficient to incorporate hydrodynamic contributions, since the stiffness of the vessel does not allow for excitation of bending modes by waves. Furthermore, the fluid can be modeled using potential flow.

3

Description to-be-created model

This chapter defines the different model that will be created in this research. At first, the model shown at the start of the literature review is shown in figure 3.1 (A). Figure 3.1 (B) shows the to-be-created models in more detail. The hydrodynamic model defines 2 different responses for the vessel, based on a wave load applied shown in blue. This response consists of a rigid body motion shown in red, and a bending deflection shown in green. Both these responses are then used as input in the structural model, creating a displacement-based excitation. The monopile is discretized using a finite element formulation, as represented in the gray beam. At certain locations of the monopile sea-fastening elements are applied, represented by the linear and unilateral springs. These locations correspond to node locations where the beam is discretized. Finally, the figure shown in (C) shows the degrees of freedom considered for every node.

Note that this model, as depicted here, only applies a one-way coupling between the ship and the monopile. This implies that forces created in the response of the cargo, are not applied back onto the vessel again. Note that this assumption decreases the complexity of the model, by creating 2 models which are independent. In this manner, troubleshooting and debugging becomes more straightforward. This comes at the cost of making an error with respect to the deflections observed for both the ship and monopile, which becomes pronounced when the forces within the sea-fastening system become large. This can be the result of large weights within the system, or by forces caused by the stiffness of the cargo. This assumption should be kept in mind during the research, and furthermore, the results presented in the report define an upper limit. Section 3.1 describes a different approach attempted at an earlier stage in the thesis.

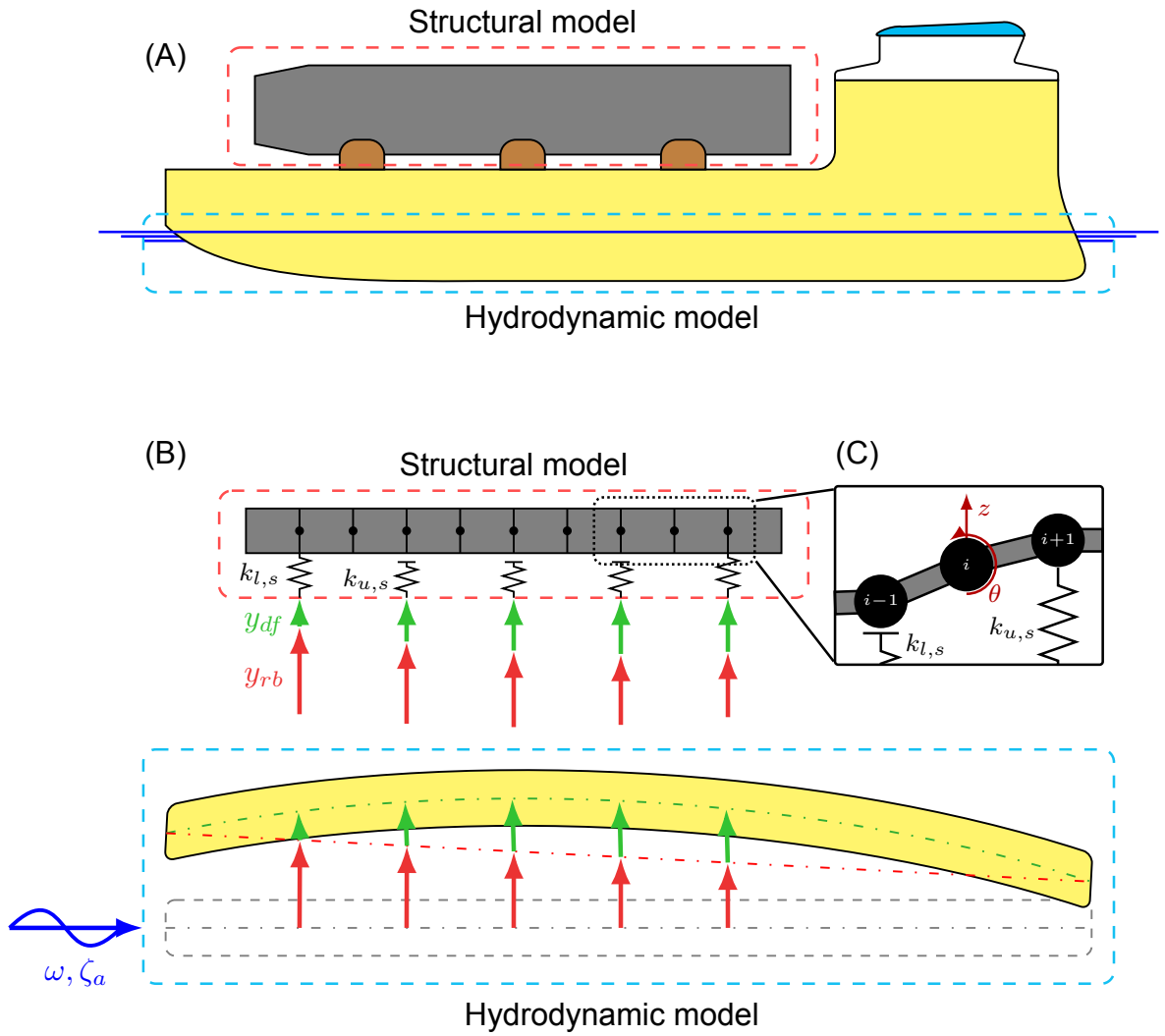

Figure 3.1: Sketch of the identified models (A) and further details on these in (B). The hydrodynamic model is excited by a certain wave load with frequency ω and amplitude ζ_a. The response of the ship consists of a rigid body motion, shown in red and represented by y_{rb}, and a bending deflection, shown in green and represented by y_{df}. This response is then used as input for the structural model. Right now an arbitrary sea-fastening system is used, consisting of linear springs with stiffness $k_{l,s}$ and unilateral springs with stiffness $k_{u,s}$. Note that the nodes are modeled with the degrees of freedom z and θ.

3.1. Two-way coupling approach

Initially a model where two-way coupling is applied was attempted at an earlier stage in the thesis. For some mathematical problems, no feasible solution was found which could be applied within the time limits of a thesis. Although no working model was obtained here, valuable insights were obtained with respect to linear structural, non-linear structural and linear hydrodynamic modeling. Based on these insights recommendations are provided for future research. More details on this approach are provided in appendix E. Note that some information, verification and validation is related to multi-models, which originated from this approach. Since in essence both approaches are based on the same theory, it is still used to validate the one-way coupling approach.

3.2. Research strategy

Figure 3.2 shows a graphical representation of the desired model, with more detail on the flow of analysis and input and output parameters. The orange blocks represent the input required to run the model. Examples of parameters related to the hydrodynamic load case are the wave amplitude ζ_a or the wave frequency ω. Parameters defined for the vessel, sea-fastening and cargo have a structural

origin, and examples of these are length L or stiffness distribution $EI(x)$.

The desired functionality of the hydrodynamic model is to define the response based on a hydrodynamic loadcase and properties of the MC-class vessel. This response consists of a certain deflection and rigid body accelerations. Both these responses are results of the hydrodynamic model, but an input for the structural model. Therefore they are represented in green and orange.

The structural model should be able to define the response of the coupled ship-cargo system, based on structural parameters and excitation. Examples of these results are represented in green, the bending moments, deflections and forces present in the system.

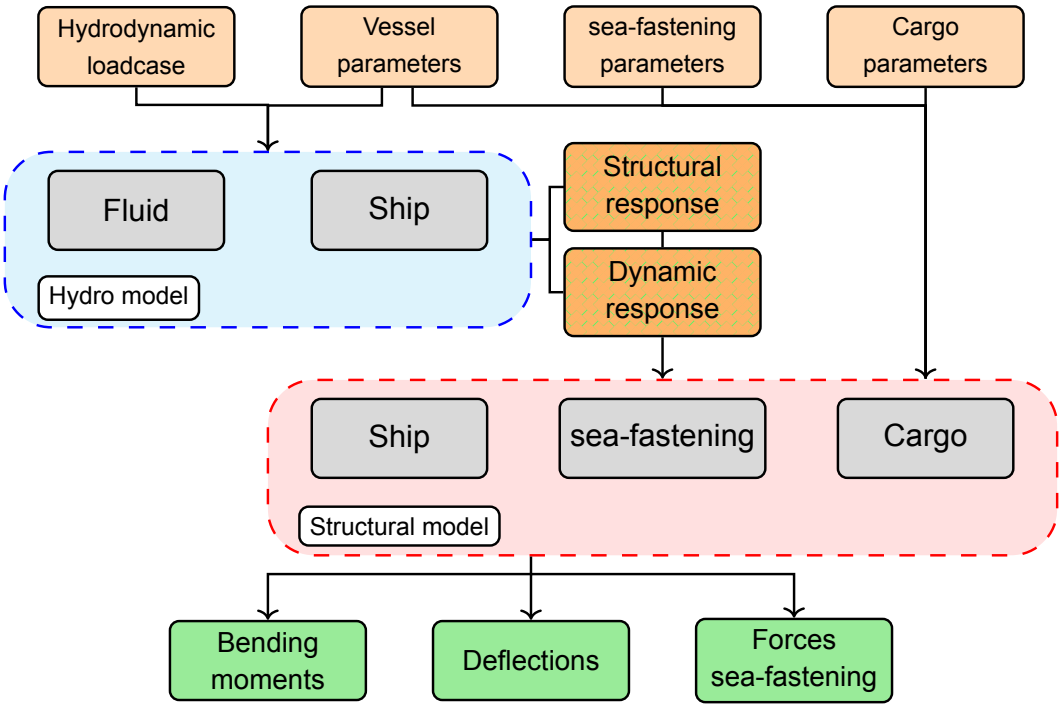

Figure 3.2: Flow of analysis and information in the to-be-created model. The orange blocks represent input based on structural and hydrodynamic parameters. The hydrodynamic model result should provide the structural and dynamic response of the ship, based on the properties of the fluid and the ship. These responses are then used as excitation for the structural model. Finally, the main results that the model should provide are shown in green.

This model is then used to give an answer to the research question and sub-questions. A brief description of the different cases is described here.

Dynamic case with non-linear behavior

With respect to the first, second and last sub-question, it is important to analyze a certain case in depth where non-linear behavior is present. To do so, a loadcase should be defined where the dynamic behavior becomes so large that the behavior shown in figure 2.4 becomes present. This figure showed the multi-body contact problem, where detachment between the sea-fastening system and the monopile occurs. A conclusion can be drawn with respect to this loadcase, to check the applied wave amplitude ζ_a and wave frequency ω could be encountered here in reality. In addition, this case makes it possible to check if modeling of unilateral constraints and the resulting non-linear behavior is performed correctly. Finally, a comparison can be made between a linear and non-linear approach, how this would influence the observed structural response of the cargo and sea-fastening system.

Parametric analysis

A parametric analysis with the main structural parameters for the cargo and sea-fastening system is of importance to give an answer to the third sub-question. By performing this analysis, the influence of these parameters can be defined on the structural response, providing an answer on this question. This analysis is performed in a linear and non-linear manner, to analyze how the modeling influences the observed results. This then helps to formulate an answer on the fourth sub-question.

4

Hydrodynamic model

This chapter discusses the mathematical formulation of the hydrodynamic model. The main objective of this model is to define a loadcase which is based on the hydrodynamic behavior of the vessel, and to translate this into loads which can serve as input for the structural model.

4.1. Deflective based loads

Using in-house software of BigLift deflections for a certain wave length and wave amplitude can be defined. In this software the deflections resulting from the hydrodynamic pressures acting on the vessel are solved in a quasi-static manner. The deflection of the vessel consists of 2 parts, which are the static and dynamic deflections. Figure 4.1 shows these deflections for the vessel, for a wave length of 171 meters and a wave amplitude of 1 meter. This loadcase is selected since it causes a high deflective response of the vessel.

The static part is based on the weight distribution of the vessel. The dynamic part based on the pressures caused by the wave. Note that this bending deflection consists of a in-phase and an out-of-phase part in comparison to the static deflection, based on if the wave causes a hogging or sagging deflection.

At last, the deflections are retrieved for a situation in which the monopile is included in the weight distribution of the vessel. By doing this the error resulting from considering one-way coupling is minimized.

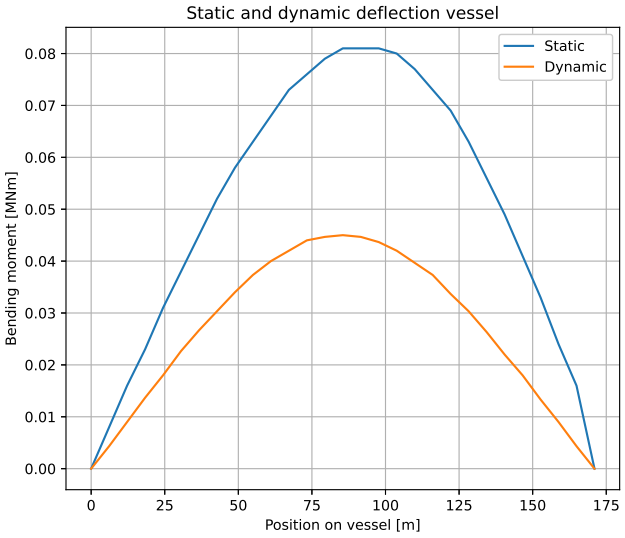

Figure 4.1: Comparison of static and dynamic deflection of vessel for a wave amplitude $\zeta_a = 1m$

The wave length of 171 meter corresponds to a wave frequency of 0.6 rad/s, given by the dispersion relation as shown in equation 4.1. Note that this dispersion relation is valid in case of a deep water wave assumption.

$$\begin{aligned} \omega^2 &= kg \\ \lambda &= \frac{2\pi}{k} \end{aligned} \tag{4.1}$$

4.2. Inertial loads

Hydrodynamic data for the MC-class vessels is obtained through BigLift. In order to connect the hydrodynamic and structural models, an important difference between the two is identified. Figure 4.2 shows the defined degrees of freedom for a ship, considered in diffraction analysis. These degrees of freedom are defined in **x**, in equation 4.2. This equation represents the equation of motion of a vessel, modeled as a rigid body. Parameters **A**, **B** and **C** represent the added mass, hydrodynamic damping and hydrostatic stiffness respectively. Parameter **M** represents the inertia of the vessel. The incoming and diffracted wave potential lead to the Froude-Krilov $\mathbf{F}_{FK}$ and diffraction $\mathbf{F}_D$ forces, defined as exciting forces.

$$[\mathbf{M} + \mathbf{A}]\,\ddot{\mathbf{x}} + \mathbf{B}\dot{\mathbf{x}} + \mathbf{C}\mathbf{x} = \mathbf{F}_{FK} + \mathbf{F}_D \tag{4.2}$$

This implies that the results of this analysis are defined for a vessel in a global coordinate system. The structural model is only able to define loads on a local level, indicating the accelerations need to be specified for entire length of the vessel. Another important difference is that the structural model is defined for a 2-dimensional situation. Therefore, only contributions and behavior relevant for surge, heave and pitch motion are considered in this analysis.

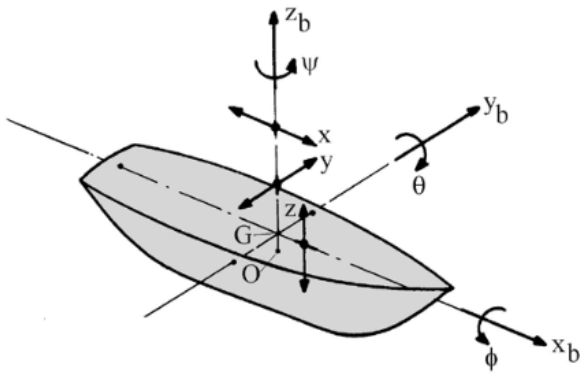

Figure 4.2: Definition ship motions in six degrees of freedom [65]

The response amplitude operators (RAO's) of a vessel can be defined using the results of the diffraction analysis. The RAO's are defined as the ratio between the motion amplitude $x_{i,a}$ and the excitation amplitude ζ_a. Figure 4.3 shows the response amplitude operators in heave and pitch direction for a MC-class vessel. Here the frequency of the considered loadcase is represented as the red dashed line.

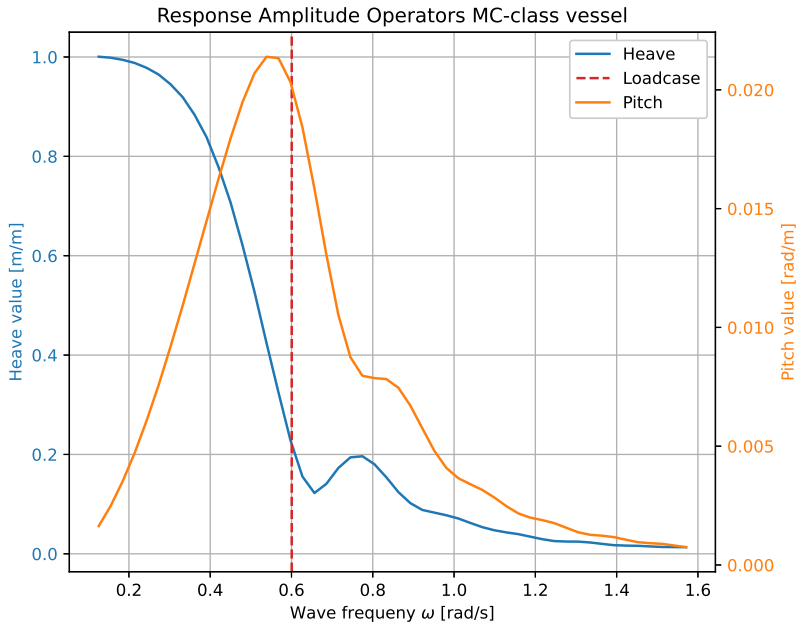

Figure 4.3: Response amplitude operators for MC-class heavy-lift vessel

The RAO in a certain direction needs to be multiplied with the wave amplitude ζ_a considered in the loadcase to obtain the global displacement of the vessel. Equation 4.3 shows the relation between the displacement and accelerations. Note that this relation is only true when considering harmonic excitation. The accelerations of the vessel cause inertial loads to which the cargo and sea-fastening system are subjected. These accelerations are transferred through the sea-fastening system, indicating that the accelerations at these specific locations need to be defined. How the displacements can be translated over the length of the vessel is shown in the second line of equation 4.3. Note that the small angle assumption $\tan(\theta) \approx \theta$ is applied here.

$$\ddot{z}_{loc} = \omega^2 \cdot z_{loc}$$
$$z_{loc} = z_{rb} - x_{loc} \cdot \theta \tag{4.3}$$

4.3. Hydrodynamic load evaluation

The following analysis is made for the system with both displacement and deflection as input for the cargo model, as shown in figure 4.4. Here the length of the cargo spans the whole ship, and the sea-fastening system consists of three pinned supports at the beginning, middle and end of the vessel. Further theoretical background on the structural model is presented in chapter 5.

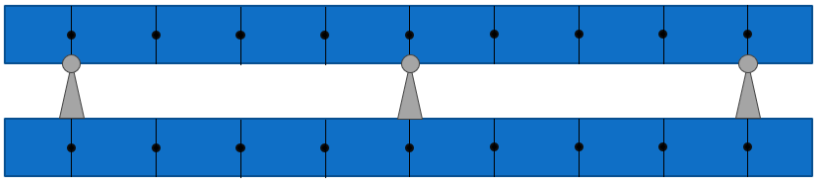

Figure 4.4: Considered example with sea-fastening system

Figure 4.5 shows a comparison between the bending moment observed for the applied bending deflection and the forced displacement resulting from the rigid body motions. These results are observed for a wave amplitude of 1 meter with a wave frequency of 0.6 rad/s. The figure also shows that the loads induced by bending far exceed the loads caused by accelerations.

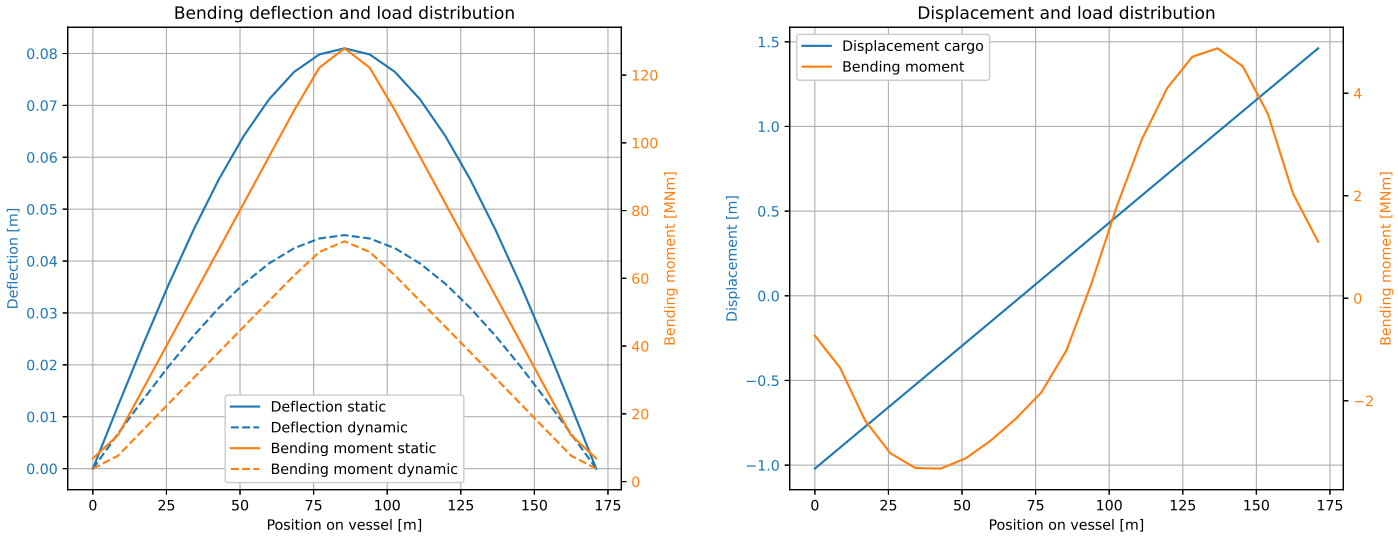

Figure 4.5: Loads based on deflection and acceleration loads

5

Structural model

This chapter defines the mathematical representation of the cargo and sea-fastening in a structural model, as shown in figure 2.1. The model is created in linear and non-linear domain, to investigate any differences between the two. At first the linear modeling is discussed, note that this has a large analogy with the non-linear model.

5.1. Linear structural model

The fundamentals of the finite element method is used in combination with Timoshenko beam theory to discretize the cargo into a number of elements. Beam theory can be applied for monopiles because their length is far greater compared to their diameter. Equation 5.1 shows the finite element matrices used in this research. Parameters E, G, I, and L_e represent the Young's modulus, shear modulus, area moment of inertia, and element length, respectively. Parameter ρA represents the weight per unit length. At last, parameter δ_s represents the shear correction factor that follows from the formulation of the Timoshenko beam equations. Please note that in this equation the total beam length is used, denoted by L_{tot}. The equations represent Euler-Bernoulli beam theory if this factor has a value of 0. Figure 5.1 shows how the global mass and stiffness matrices can be constructed from both element matrices.

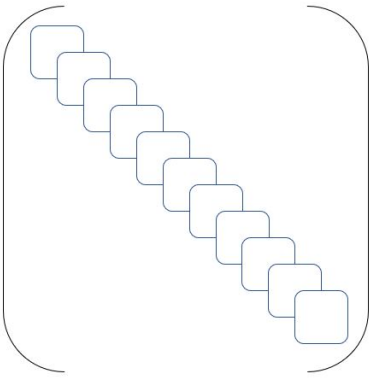

Figure 5.1: Construction of global matrix from element mass and stiffness matrix

$$\delta_s = \frac{6}{5}\frac{12 \cdot EI}{GA \cdot L_{tot}^2}$$

$$K_e = \begin{bmatrix} \frac{12EI}{(1+\delta_s)L_e^3} & \frac{6EI}{(1+\delta_s)L_e^2} & -\frac{12EI}{(1+\delta_s)L_e^3} & \frac{6EI}{(1+\delta_s)L_e^2} \\ \frac{6EI}{(1+\delta_s)L_e^2} & \frac{(4+\delta_s)EI}{(1+\delta_s)L_e} & -\frac{6EI}{(1+\delta_s)L_e^2} & \frac{(2-\delta_s)EI}{(1+\delta_s)L_e} \\ -\frac{12EI}{(1+\delta_s)L_e^3} & -\frac{6EI}{(1+\delta_s)L_e^2} & \frac{12EI}{(1+\delta_s)L_e^3} & -\frac{6EI}{(1+\delta_s)L_e^2} \\ \frac{6EI}{(1+\delta_s)L_e^2} & \frac{(2-\delta_s)EI}{(1+\delta_s)L_e} & -\frac{6EI}{(1+\delta_s)L_e^2} & \frac{(4+\delta_s)EI}{(1+\delta_s)L_e} \end{bmatrix} \quad (5.1)$$

$$M_e = \frac{\rho A \cdot L_e}{420} \cdot \begin{bmatrix} 156 & 22L_e & 54 & -13L_e \\ 22L_e & 4L_e^2 & 13L_e & -3L_e^2 \\ 54 & 13L_e & 156 & -22L_e \\ -13L_e & -3L_e^2 & -22L_e & 4L_e^2 \end{bmatrix}$$

Equation of motion

The equation governing the elastodynamic calculations within a Finite Element Method (FEM) model is expressed in equation 5.2 [73]. This equation of motion is a system of equations, due to the division of the structure into elements. Parameters **M**, **D** and **K** represent the global mass, damping, and stiffness

matrix, respectively. Note that parameter **x** represents the degrees of freedom in the system, equal to the number of elements times the degrees of freedom z and θ. At last, parameter **f** represents the external excitation forces in the system.

$$[\mathbf{M}]\ddot{\mathbf{x}} + [\mathbf{D}]\dot{\mathbf{x}} + [\mathbf{K}]\mathbf{x} = \mathbf{f}_{ex}(t) \tag{5.2}$$

The response **x** can assumed to be harmonic, because of the harmonic nature of wave loads. The equation can therefore be translated into frequency domain, as shown in equation 5.3. Parameter ω represents the excitation frequency of the forced displacement. The external harmonic forcing $\mathbf{f}_{ex}(t)$ is in this case equal to **0**, since a forced displacement situation is considered.

$$\begin{aligned} x_i &= x_{i,a} \cdot \sin(\omega t) \\ \left(-\omega^2[\mathbf{M}] + \omega[\mathbf{D}] + [\mathbf{K}]\right)\mathbf{x} &= \mathbf{0} \end{aligned} \tag{5.3}$$

Responses to forced displacement load cases can be evaluated using matrix partitioning. The partition of the equation of motion is shown in equation 5.4. Note that the matrices used in equation 5.3 are summarized into a dynamic stiffness matrix K_{dyn}.

Matrix partitioning

The equation of motion is divided into submatrices corresponding to the known displacement vector $\mathbf{x}^o$ and the unknown vector $\mathbf{x}^c$. The unknown displacement vector $\mathbf{x}^c$ can be solved based on the known displacement vector $\mathbf{x}^o$ and the known force vector $\mathbf{f}^c$, as shown in the third step. Here a prerequisite is that the forces $\mathbf{f}^c$ applied on the unknown displacement degrees of freedom $\mathbf{x}^c$ are known. The last step shows how the unknown forces $\mathbf{f}^o$ are obtained, required to force the displacement.

$$\begin{aligned} \mathbf{K}_d &= \left(-\omega^2[\mathbf{M}] + \omega[\mathbf{D}] + [\mathbf{K}]\right) \\ \begin{bmatrix} \mathbf{f}^c \\ \mathbf{f}^o \end{bmatrix} &= \begin{bmatrix} \mathbf{K}_d^{cc} & \mathbf{K}_d^{co} \\ \mathbf{K}_d^{oc} & \mathbf{K}_d^{oo} \end{bmatrix} \begin{bmatrix} \mathbf{x}^c \\ \mathbf{x}^o \end{bmatrix} \\ \mathbf{x}^c &= [\mathbf{K}_d^{cc}]^{-1}\left[\mathbf{f}^c - \mathbf{K}_d^{co}\mathbf{x}^o\right] \\ \mathbf{f}^o &= \mathbf{K}_d^{oc}\mathbf{x}^c - \mathbf{K}_d^{oo}\mathbf{x}^o \end{aligned} \tag{5.4}$$

The static deflections resulting from gravitational forces of the monopile and sea-fastening system are also obtained using equation 5.3. This equation can also be solved in a static manner, resulting in $\mathbf{f}_{ex} = [\mathbf{K}]\mathbf{x}$. Note that in this situation the exciting force is equal to the gravitational forces acting on the monopile, distributed over its length. The resulting deflections can be superimposed on the dynamic deflections to obtain the total response.

Appendix F represents the verification performed on the linear structural model. In there an analytical model is developed, and modal analysis is considered.

5.2. Non-linear structural model

The non-linear solution method is required to handle the nonlinearities introduced by the saddles, modeled as unilateral springs. The fundamental equation of motion behind non-linear vibrations is shown in equation 5.5 [51]. Please note the analogy to the equation shown in 5.3, the parameters shown here are equal to the linear fundamental equation. The solution here is represented by **q** instead of **x**, to highlight the difference between the linear and non-linear solution. The only difference here is that there is a non-linear force term present, which is $\mathbf{f}_{nl}(\mathbf{q}, \dot{\mathbf{q}})$. This vector defines the non-linear force for non-linear elements within the system, being dependent on the displacement **q** or velocity $\dot{\mathbf{q}}$. The nonlinearity can also originate from the excitation term $\mathbf{f}_{ex}(t)$ [47], but this is not true for the considered case.

$$\begin{aligned} &[\mathbf{M}]\ddot{\mathbf{q}} + [\mathbf{D}]\dot{\mathbf{q}} + [\mathbf{K}]\mathbf{q} + \mathbf{f}_{nl}(\mathbf{q}, \dot{\mathbf{q}}) = \mathbf{f}_{ex}(t) \\ &\mathbf{f}_{ex}(t) = \mathbf{f}_{ex}(t+T) \end{aligned} \tag{5.5}$$

This equation of motion can be solved numerically using various different solution techniques, for example the shooting method, harmonic balance method and intermediate methods as identified in the literature review. The assumption is made that the non-linear forces and responses can be represented as summation of harmonics, as stated by the harmonic balance method. This assumption is based on the fact that the main excitation source is harmonic and on other studies that solve for unilateral constraints using this method [55].

Equation 5.6 shows the equation of motion rewritten in frequency domain, with the solution rewritten as a truncated Fourier series. Note that the periodic part has been dropped for the last equation. This equation shows that rewriting this equation in this form results in a system of $n \cdot (2H+1)$. Parameter n represents the number of degrees of freedom present in the discretized system, for which a zero frequency term, a sine and a cosine term is present. The sine and cosine term are present for every harmonic, up to the harmonic H. Parameter k represents the harmonic considered in the summation.

$$\begin{aligned} \mathbf{q}(t) &= \mathbf{Q}_0 + \sum_{k=1}^{H} \mathbf{Q}_{c,k} \cos k\omega t + \sum_{k=1}^{H} \mathbf{Q}_{s,k} \sin k\omega t \\ &= \Re\{\sum_{k=0}^{H} \mathbf{Q_k} \mathrm{e}^{\mathrm{i}k\omega t}\} \\ \Re\{\sum_{k=0}^{H} \left(\left[-(k\omega)^2[\mathbf{M}] + \mathrm{i}k\omega[\mathbf{D}] + [\mathbf{K}]\right] \mathbf{Q_k} + \mathbf{f}_{\mathrm{nl},k}\right) &= \mathbf{f}_{\mathrm{ex},k} \end{aligned} \tag{5.6}$$

Description of non-linear force

The nonlinear force vector $\mathbf{f}_{\mathrm{nl},k}$ is analyzed in more depth. The force deflection curve for a unilateral linear spring is shown in figure 5.2 . The desired curve is shown in blue, and the regularized curve in green [74]. Important to understand here is that the function shown in equation 5.6 is solved using numerical solvers. For these solvers a smooth function, and a smooth derivative are desired. Therefore, it is necessary to apply force regularization on the original force deflection curve, shown in blue. The regularized curve, shown in green is smooth, as is its derivative. Note that k in this function is the regularization parameter. This value has been set to 1000 in order to have sufficient accuracy around 5 millimeters. Later on in paragraph 6.1 an analysis is presented why an accurate saddle force deflection curve is important.

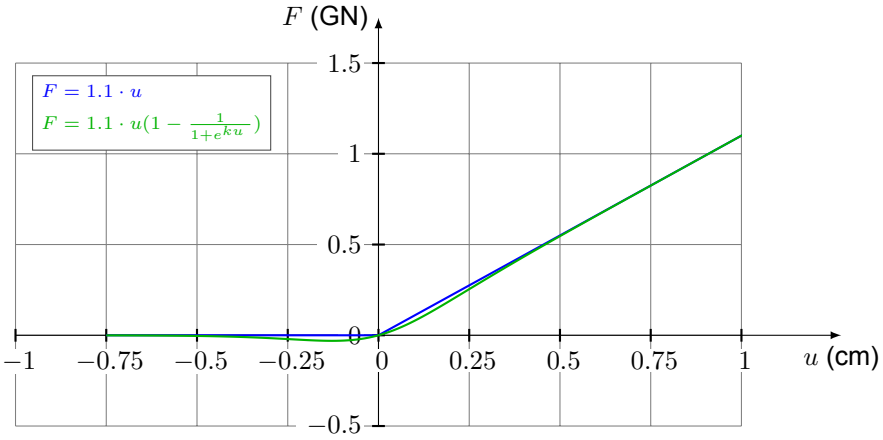

Figure 5.2: Force deflection curves for different saddle formulations

As stated in [51], the quality of the solution highly depends on to what extent the nonlinear force can be described using harmonics. Three different solution strategies are identified to define the non-linear force harmonics $\mathbf{f}_{\mathrm{nl,k}}$ [51]:

1. Polynomial non-linear forces: solve for closed-form expression

2. For piecewise polynomial forces: determine transition times, proceed as in 1
3. Generic non-linear forces: apply Alternating Frequency-Time (AFT) scheme

Within this problem the usage of Alternating Frequency-Time is selected to be most suitable to define the non-linear force harmonics. Due to the unilateral constraints present in the problem, it is hard to define the transition times between different states. Figure 5.3 shows an example of the AFT procedure applied for this case. This figure shows that the green curve is defined in time domain, based on the deflection of the saddle shown in blue. The definition in time domain is based on a certain number of samples N.

The green curve is then approximated by a number of harmonics using the Fourier Transform, as shown by the red curve. Note that this red curve is an approximation, which improves with a higher number of harmonics. Important to observe here is the slight tensile force present for the saddle, shown for the green curve. This is due to the regularization of the force shown in figure 5.2. This figure also shows that an appropriate number of harmonics needs to be chosen to represent the non-linear force.

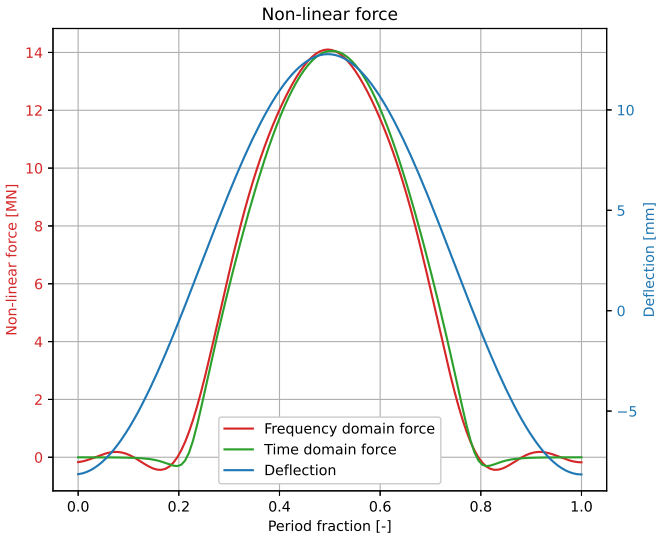

Figure 5.3: Example Alternating Frequency-Time procedure for saddle stiffness formulation

After some analysis, some valuable insights are obtained:

1. The number of samples in time domain N should be based on the magnitude of nonlinearity.
2. A trade-off should be made in the accuracy generated by the number of harmonics and the efficiency of the model.
3. Strong nonlinearities can cause the Gibbs phenomenon to become pronounced.

Not taking these main points into account could lead to false results or convergence errors.

Definition of sea-fastening elements

Figure 5.4 shows an example of a sea-fastening system applied when transporting monopiles.

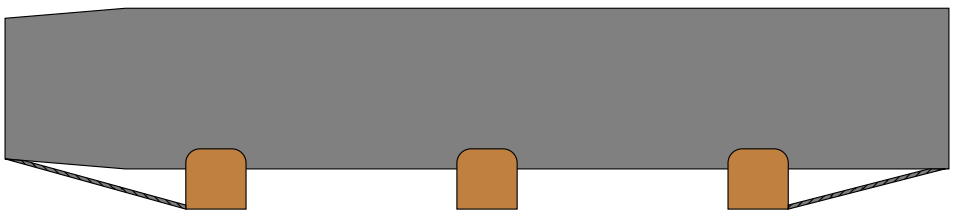

Figure 5.4: Schematic overview sea-fastening system applied at monopiles

This figure shows a number of saddles applied, in combination with lasting wires at the outer ends of the monopiles. Figure 5.5 shows a detailed version of these outer ends of the monopiles. The implementation of these different sea-fastening elements requires some attention in detail. This figure shows how a combination of lashing wires and saddles is modeled. Important to note here is that both the saddle and lashing wire act in a unilateral manner, only providing reaction force in compression and tension respectively. A combination of both can be modeled in a linear manner with spring stiffness k_z.

Furthermore, since the stiffness of the saddle is much greater than that of the lashing wire, a unilateral spring with the remaining stiffness k_s is added. At last, the lashing wire also provided some rotational resistance around the saddle. This is modeled as a linear rotational spring with stiffness k_θ. The assumption is that the lashing wire is always in tension by applying pre-tension, allowing the rotational spring to be modeled in a linear manner. Note that for the saddle located in the middle of the monopile only a unilateral spring with the total saddle stiffness is applied. At last, it is important to note that within the linear model the unilateral spring stiffness k_s is linearized, and added to the linear stiffness k_z.

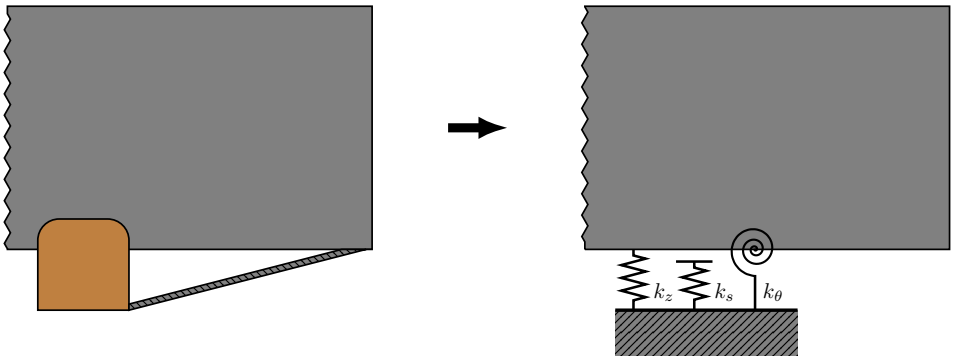

Figure 5.5: Detailed version of monopile aft end with implementation of spring stiffnesses

At last, attention should be paid to the fact that additional elements in the global stiffness and mass matrix should be added for the sea-fastening elements. Here a separate approach exists for the linear and non-linear model. For the linear model, all sea-fastening elements are linearized and included in the stiffness matrix. For the non-linear model, only the linear elements are added in the stiffness matrix. This is due to the formulation shown in 5.6, the forces resulting from non-linear elements is included in $\mathbf{f}_{nl,k}$. Note that the implementation in the mass matrix is equal for both models, here the mass and rotary inertia of the saddle are included.

Figure 5.6 shows a graphical representation in the linear stiffness matrix. The stiffness of the saddle and the lashing is exaggerated to ensure visibility in the matrix. Rows and columns are appended at the end of the matrix, with values connecting the sea-fastening element to the corresponding location on the monopile. By doing this, the forced displacement can be applied on the bottom of the saddle, ensuring that deflections of the saddles can also be evaluated.

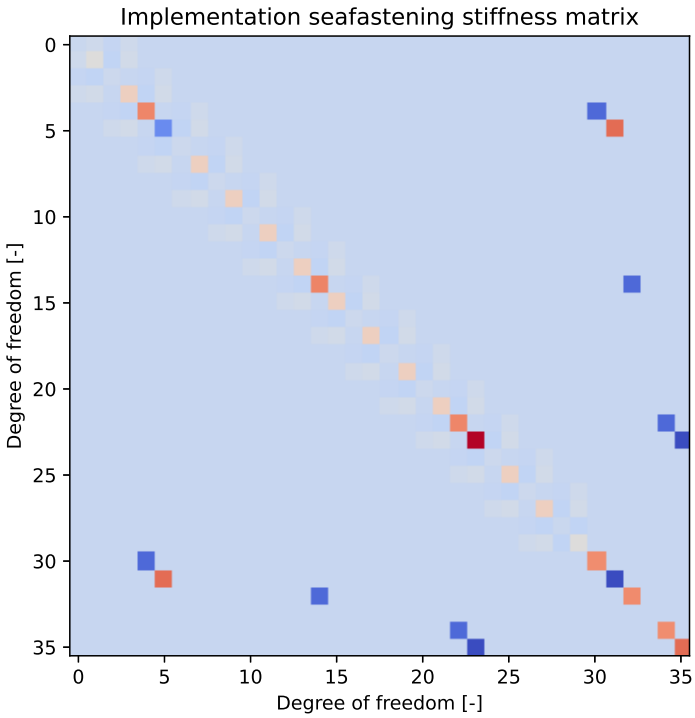

Figure 5.6: Implementation of sea-fastening elements in global stiffness matrix

Residual function & solver

Within the mathematical description of the model, one final step is required to be able to apply a forced displacement situation. The formulation is shown in equation 5.7. Matrix partitioning is applied again in combination with the definition of the dynamic stiffness matrix $\mathbf{K}_d$. The function is rewritten in residual form, and this function represents the residual of all harmonics. The exciting force $\mathbf{f}_{\text{ex}}$ only has a value for the zeroth harmonic $k = 0$, here the gravitational forces are distributed over the length of the monopile.

$$\begin{aligned} \mathbf{K}_d &= \left[-(k\omega)^2[\mathbf{M}] + (\mathrm{i}k\omega)[\mathbf{D}] + [\mathbf{K}]\right] \\ \mathbf{R} &= [\mathbf{K}_d^{cc}]\,\mathbf{q}^c + [\mathbf{K}_d^{oc}]\,\mathbf{q}^o + \mathbf{f}_{\text{nl}} - \mathbf{f}_{\text{ex}} = \mathbf{0} \end{aligned} \tag{5.7}$$

This residual function is then used in numerical solvers, in combination with an analytical Jacobian of this function. The Jacobian ensures efficient solving of this function.

Definitions structural response

Two main results can be obtained from equation 5.7, which is the excitation force $\mathbf{f}_{ex}$ required to obtain the response and the resulting harmonic displacements $\mathbf{q}$. The resulting deflections can be obtained by subtracting the rigid body displacements from the resulting displacement. From there, equation 5.8 can be applied to obtain the bending moment $\mathbf{M}_b$. This bending moment is defined over the length of the cargo x. Parameter $\mathbf{w}_{xx}$ represents the displacement of the cargo in z-direction for every degree of freedom, for which the derivative needs to be taken twice with respect to the length direction. Parameter I represents the moment of inertia of the monopile.

$$\mathbf{M}_b = -EI \cdot \mathbf{w}_{xx} \tag{5.8}$$

The bending moment can then be used to compute the resulting bending stress using equation 5.9. In this equation parameter y is equal to the outer fiber distance.

$$\sigma_b = \frac{\mathbf{M_b} \cdot y}{I} \tag{5.9}$$

Continuation method

In conventional non-linear vibration analysis the solution method is applied together with a continuation method. Examples of these are the Asymptotic Numerical Method (ANM) [53] and pseudo-arclength continuation [50]. Within this considered case, no continuation method is applied, since only a single loadcase is considered. Based on a pinned situation, an eigenfrequency of 25 rad/s can be defined for the considered monopile. Since the excitation only has an eigenfrequency of 0.6 rad/s, the conclusion can be drawn that this loadcase remains in a low-energy situation. Therefore, behavior related to bifurcations, bending and jumping is not expected.

This concludes the modeling sections present within this problem. A modeling method has been found to transform a hydrodynamic load into displacements at the locations of the saddles. A structural model is created in which the responses of the monopile and sea-fastening system can be evaluated using a displacement-based load.

Verification and validation of the structural non-linear model is presented in appendix G. Note that some verification is also performed when analyzing the results, presented in chapter 6.

6

Results

This chapter presents the findings based on the research carried out using the model. The results are based on a number of different cases. The first paragraph introduces the considered case with the related parameters defined for the cargo. Afterwards, there is continued with a static, linear dynamic, and a non-linear dynamic analysis. The response of the system is analyzed in depth for these cases, to better understand and verify the observed behavior. With this knowledge different parametric analyses are performed. These analyses define the influence of certain cargo and sea-fastening parameters on the behavior of the total system.

6.1. Implementation in case

In order to verify the modeling method a realistic case is modeled. This case is based on a project performed by BigLift and shown in figure 6.1. In this project 4 large monopiles were transported, using saddles and lashing wires as the sea-fastening system.

Figure 6.1: Considered example case used in this analysis

For the monopiles the parameters shown in table 6.1 are identified. The total lateral area and moment of inertia can be obtained by multiplying the value by 4. For this particular project the deflections of the vessel can be retrieved. At first, a static case is analyzed and linear modeling is applied.

Table 6.1: Structural parameters example monopile

Parameter		Value	Unit
Length	L	74	m
Diameter	D	8	m
Thickness	t	8	mm
Moment of inertia	I_m	15.6	m^4
Lateral area	A_m	2.00	m^2
Weight monopile	W_m	11.3	MN

Figure 6.2 shows a schematic overview of the sea-fastening system applied in this project. At either end of the monopile lashing wires are present to prevent the monopile from sliding in axial direction. The brown elements represent saddles, located at $0.2L$, $0.5L$ and $0.8L$ of the length of the monopile.

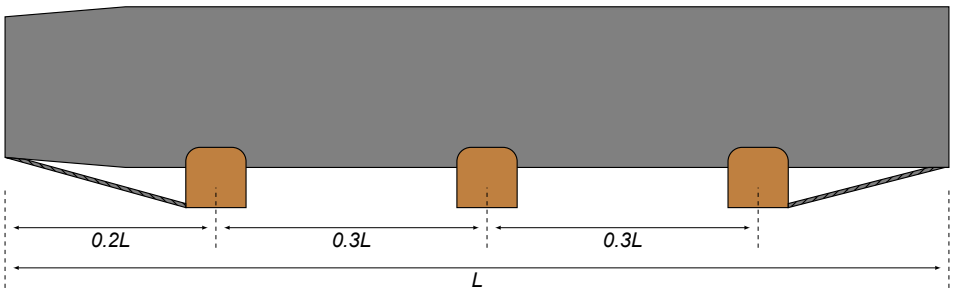

Figure 6.2: Schematic overview sea-fastening system applied at monopiles

Table 6.2 shows the properties of the elements present in the sea-fastening system. The definition of the stiffnesses is presented in figure 5.5. The stiffness of the saddle is evaluated using information from a finite element analysis, which was performed in the project. Figure 6.3 shows a detailed example of the saddles applied. This figure shows that in addition to the axial stiffness, the bending stiffness is also important in this situation. In this report, a force of 8.6 MN was stated to lead to a deflection of 8 mm. Therefore, the stiffness of the saddle has a value of 1.1 GN/m.

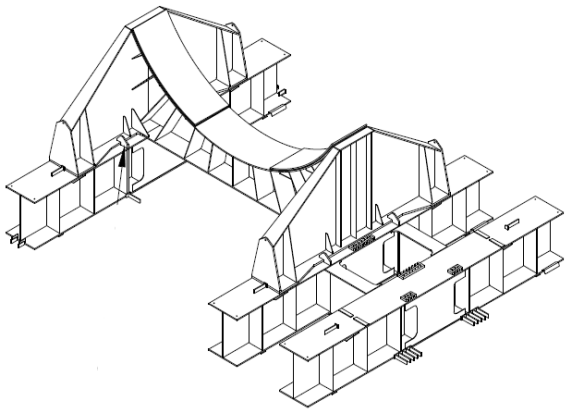

Figure 6.3: Example of saddle used in sea-fastening system

The lashing stiffness is obtained using equation 6.1, and it is retrieved from OrcaFlex documentation. In this equation parameter d represents the wire diameter and L the wire length. Parameter E represents the Young's modulus. The total stiffness of the lashing is obtained by multiplying the stiffness with the number of wires applied. Information from BigLift indicates that usually a pre-tension of 1-2 mT is applied per lashing wire. This comes down to 10 kN per wire, so for the example case the total pretesion would be 210 kN. Note that table 6.2 shows the properties for all combined lashing wires.

$$A = 0.455 \cdot \frac{\pi d^2}{4}$$
$$k = \frac{EA}{L} \tag{6.1}$$

Table 6.2: Structural parameters sea-fastening system, as defined in fiugre 5.5

Parameter		Value	Unit
Saddle stiffness	k_s	1.1	GN/m
Lashing stiffness	k_{lash}	37.5	kN/m
Linear stiffness	k_z	6.5	kN/m
Rotational stiffness	k_θ	1.46	MNm/rad
Lashing pre-tension	T_{lash}	210	kN

6.1.1. Static analysis

Figure 6.4 shows the results of the linear model, for a static case. This implies that only the static deflection of the vessel is applied as a forced displacement and that gravity acting on the monopile is taken into account. The deflection of the cargo is defined relative to its own position, indicated by the beginning and end of the cargo having a deflection of 0. The deflection of the vessel is presented relative to the deflection of the cargo. In addition, the difference in deflection between the two curves represents the deflection of the saddles, at the corresponding locations.

This figure shows that the maximum deflection of the cargo has a value of 6 millimeters. The deflection of the vessel shows the deflection that is enforced on the cargo at $0.2L$, $0.5L$ and $0.8L$ of the monopile. The figure on the right shows the forces and bending moment distribution. For the force where no saddles are present a slight offset below 0 is observed, this is caused by the gravity acting on the monopile.

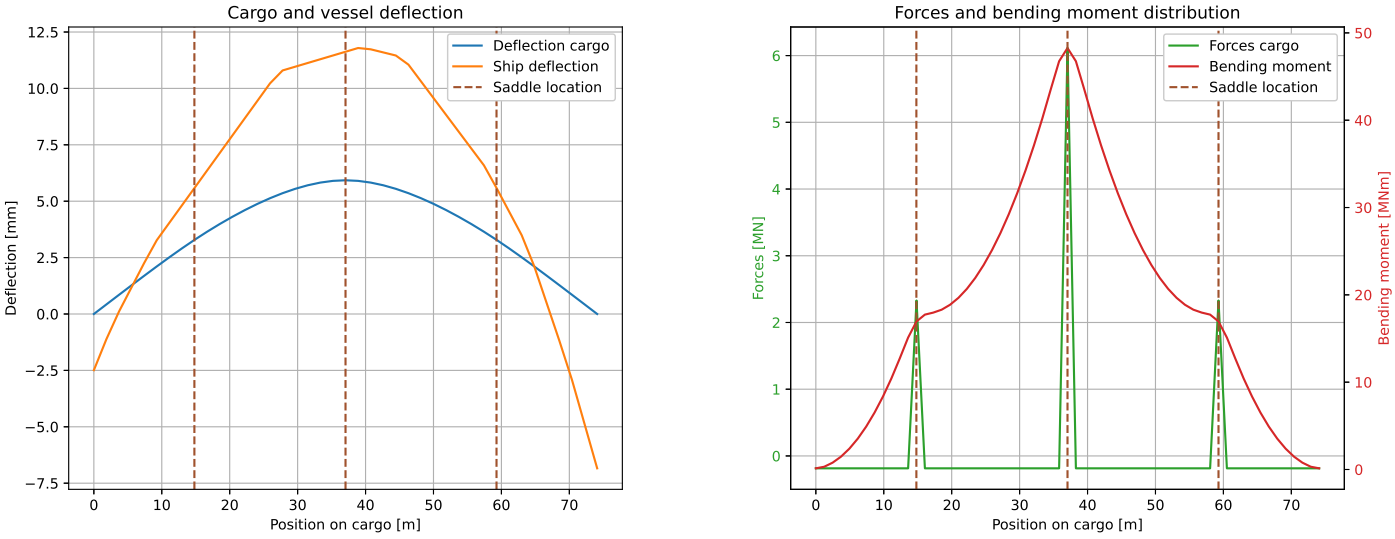

Figure 6.4: Deflection and forces in sea-fastening system with static loadcase for linear analysis

Table 6.3 shows the resulting deflections and structural response. What draws attention here is that the deflection of the saddle located at $0.5L$ is significant compared to the deflection of the monopile.

In addition, the maximum force applied by the sea-fastening system is equal to half the weight of the monopile. The bending of the monopile results in the middle saddle carrying more load compared to the outer two saddles. The bending moment causes a bending stress of 12.6 MPa. Compared to the yield stress this stress is small, but it is expected that failure occurs earlier due to buckling or local damage around the saddle. Further research should investigate what the implications are of high internal bending moments or high saddle forces on damage onto the monopile.

Table 6.3: Results for static loadcase

Parameter		Linear	Unit
Deflection mon. max.	$u_{c,max}$	5.9	mm
Deflection sad. max.	$u_{d,max}$	5.7	mm
Force max	F_{max}	6.3	MN
Bending mom. max.	$M_{b,max}$	49.3	MNm
Stress max.	$\sigma_{b,max}$	12.6	MPa

The static deflection of the monopile is evaluated to verify that this case is indeed linear. This is done by using the beam tool of HES[1], which results in a monopile deflection of 12 millimeters. In this situation the assumption is made that the monopile only rests on the middle saddle, shown in figure 6.5. The deflection of the monopile under its own weight is larger than the deflection shown in 6.3, indicating that contact is preserved. The figures shown in 6.5 show that the applied saddle force is equal to the monopile weight, as expected. This case will be used as a reference case in the further analysis.

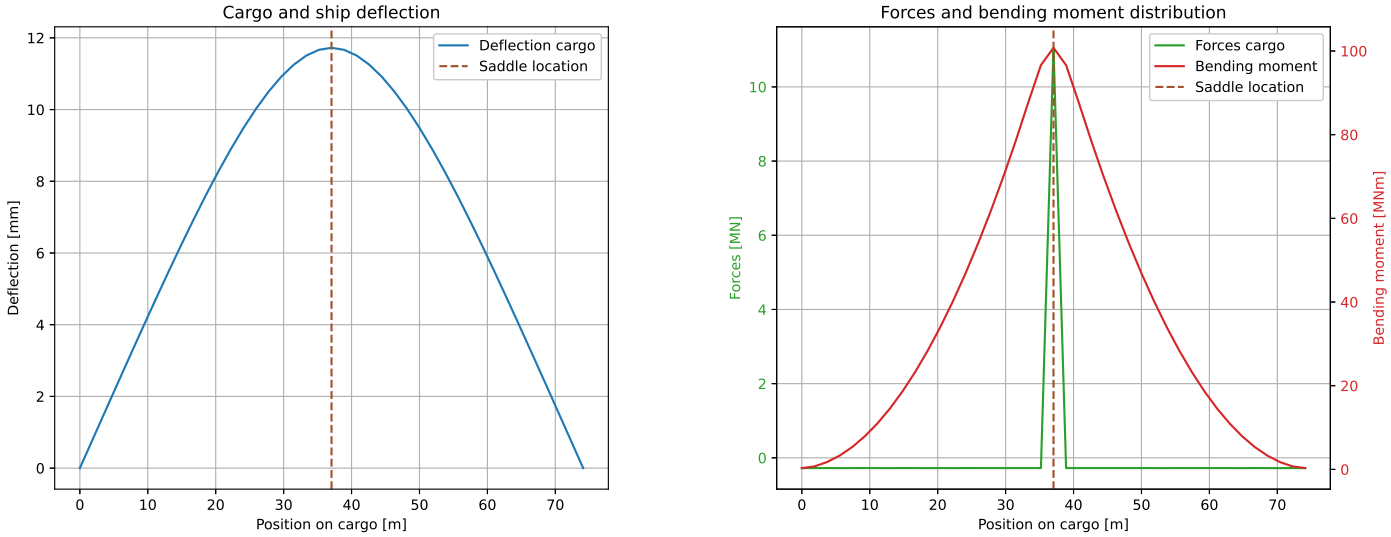

Figure 6.5: Deflection and forces in monopile due to bending under own weight

Another conclusion that can be drawn is that the deflections are small compared to the length this monopile overspans, this deflection of 12 millimeters is present over a length of 37.5 meters. It should be emphasized here that the analysis now navigates to areas where the production and design tolerances become important. These tolerances are present in, for example, saddle height, monopile diameter, deck height, etc. In reality, the loss of contact would be resolved by applying shim plates with variable thickness, of which an example is shown in figure 6.6.

[1] https://www.heerema.com/heerema-engineering-solutions/beam-tool

Figure 6.6: Shim plates applied to support structure at saddle

Sensitivity study

The sensitivity of the system to changes in deflections is emphasized by the following analysis. Figure 6.7 shows an analysis in which the stiffness of the saddle is assumed to be half the actual value. If compared to the results shown in figure 6.4, a large difference in deflection, force and bending moment distribution can be observed.

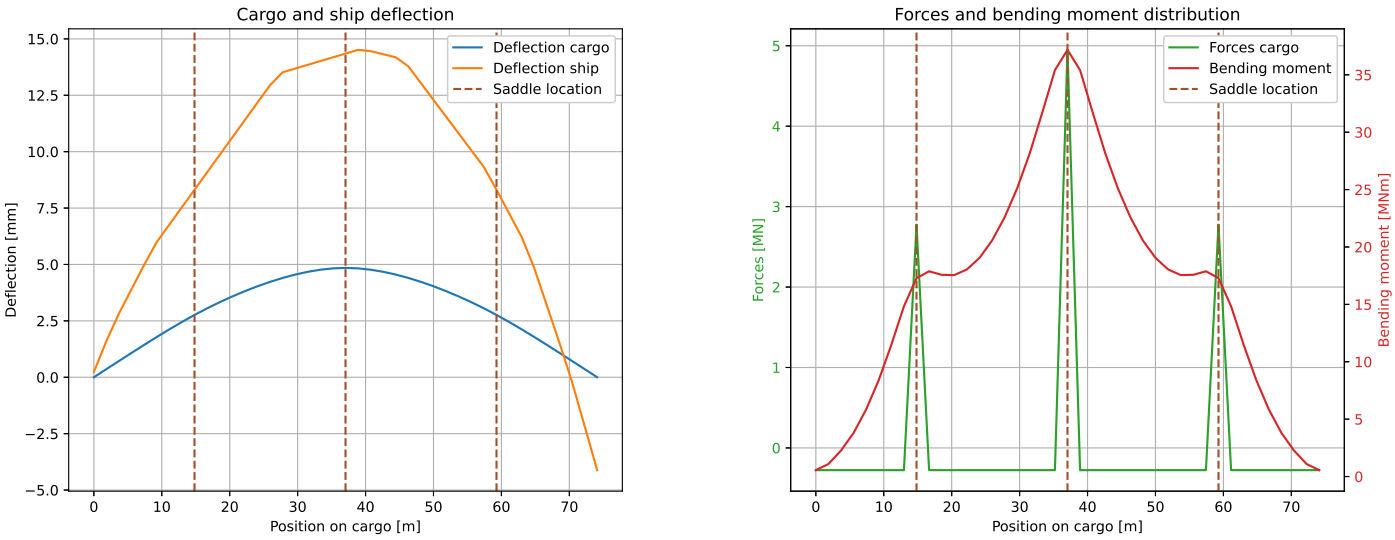

Figure 6.7: Deflection and forces in sea-fastening system with static loadcase for too weak saddles

This is supported by the results shown in table 6.4. This table shows that for a decreased saddle stiffness, the axial deflection of the saddle increases, but as a result, the deflection of the monopile decreases. The opposite is true as well, as shown for a case with double saddle stiffness. The observation is made that the bending moment and force distribution get influenced by these deflections significantly. The conclusion can be drawn that the deflections of the saddle strongly influence the response of the monopile.

Table 6.4: Maxima for static loadcase using different saddle stiffnesses

Parameter		Linear 1 K_{sad}	Linear 0.5 K_{sad}	Linear 2 K_{sad}	Unit
Deflection monopile	u_m	5.9	4.8	7.6	mm
Deflection saddle	u_s	5.7	9.5	3.4	mm
Force sea-fastening	F	6.3	4.9	7.3	MN
Bending moment	M_b	49.3	37.2	62.0	MNm
Bending stress	σ_b	12.6	9.5	15.9	MPa

Note that in this situation the deflections of the saddles are varied using the saddle stiffness, other sources of a different force distribution can also be imagined. For example, local plate bending of the cargo deck is not taken into account, but this can reach an order of magnitude of centimeters. Futhermore, production tolerances related to the saddles also influence these results.

These examples highlight the sensitivity of the system with respect to the forced deflection of the ship, the axial deflection of the saddles and the resulting bending deflection of the monopile. All three parameters have an influence on the observed force en bending moment distribution.

At last, this emphasizes as well to model the saddle stiffness properly. Figure 6.8 shows the initial implemented force deflection curve in red compared to the linear force deflection curve in blue and the regularized function in green. The assumption for the red curve originated at the beginning of this research, when there was no knowledge of the influence of deflection on the bending moments experienced within the cargo. Note that although not being interested in the axial deflection of the saddle, it is crucial to model it correctly within this problem.

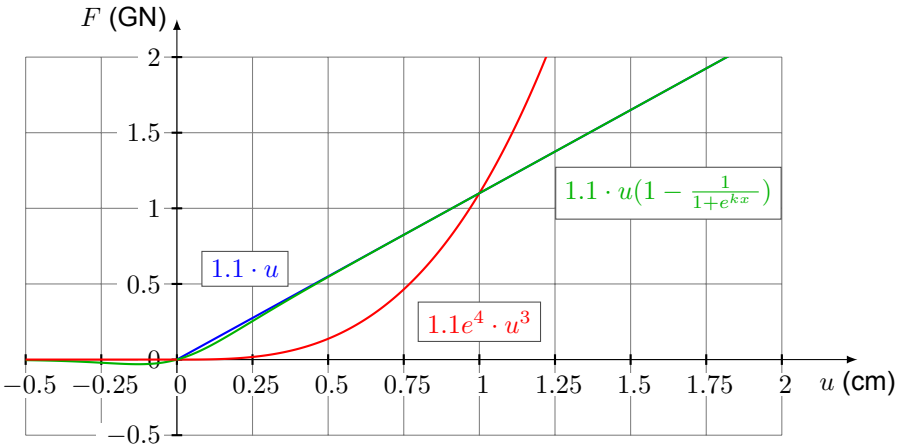

Figure 6.8: Force deflection curves for different stiffness formulations

6.1.2. Dynamic analysis with linear behavior

Within the dynamic analysis, first a linear dynamic situation is evaluated. This case is used to verify the non-linear modeling method. Table 6.5 shows the loadcase related parameters. For this particular wave length the dynamic deflections of the vessel are taken into account as well.

Table 6.5: Parameters used in hydrodynamic loadcase

Parameter		Value	Unit
Wave frequency	ω	0.6	rad/s
Wave length	L_w	171	m
Wave amplitude	ζ_a	1	m

Figure 6.9 shows the results for the linear dynamic loadcase. Now an oscillatory force is present; therefore, the timestep within the oscillation is shown on the y-axis. These figures show the influence

of the dynamic load on the forces observed in the sea-fastening system. Throughout the whole period, the forces remain positive, indicating that contact between the saddles and the monopile is preserved.

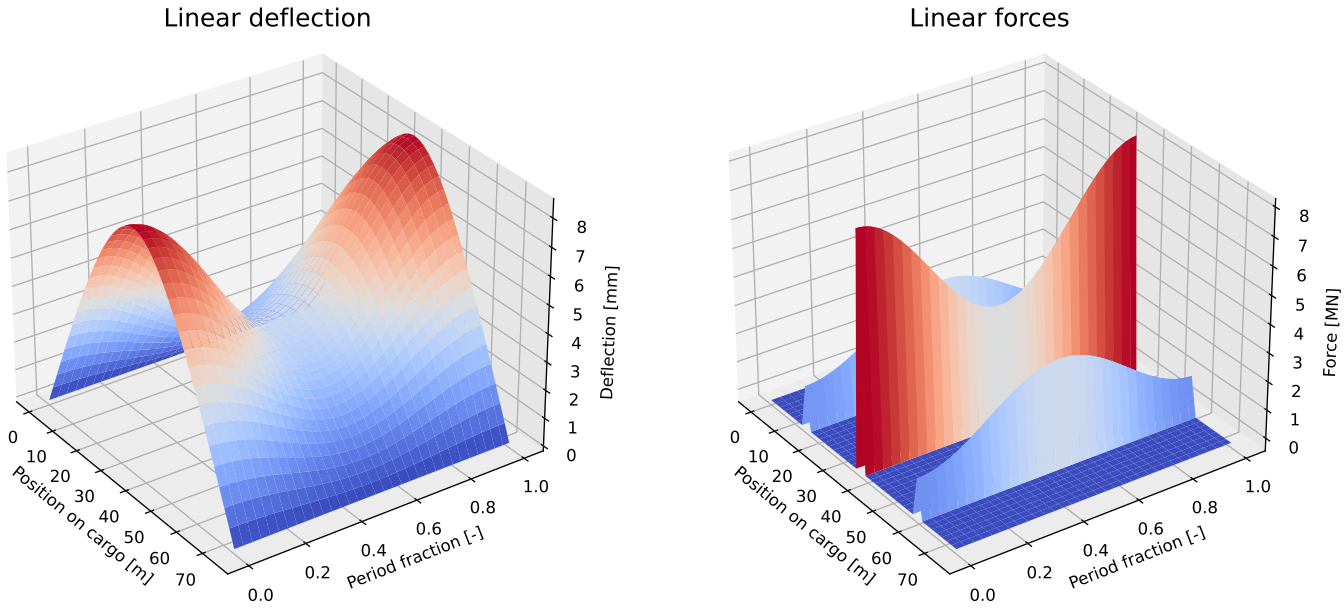

Figure 6.9: Deflection and forces in monopile over time

Figure 6.10 shows the results observed for the same loadcase, but analyzed using the non-linear model. These figures good accordance with the results for the linear model.

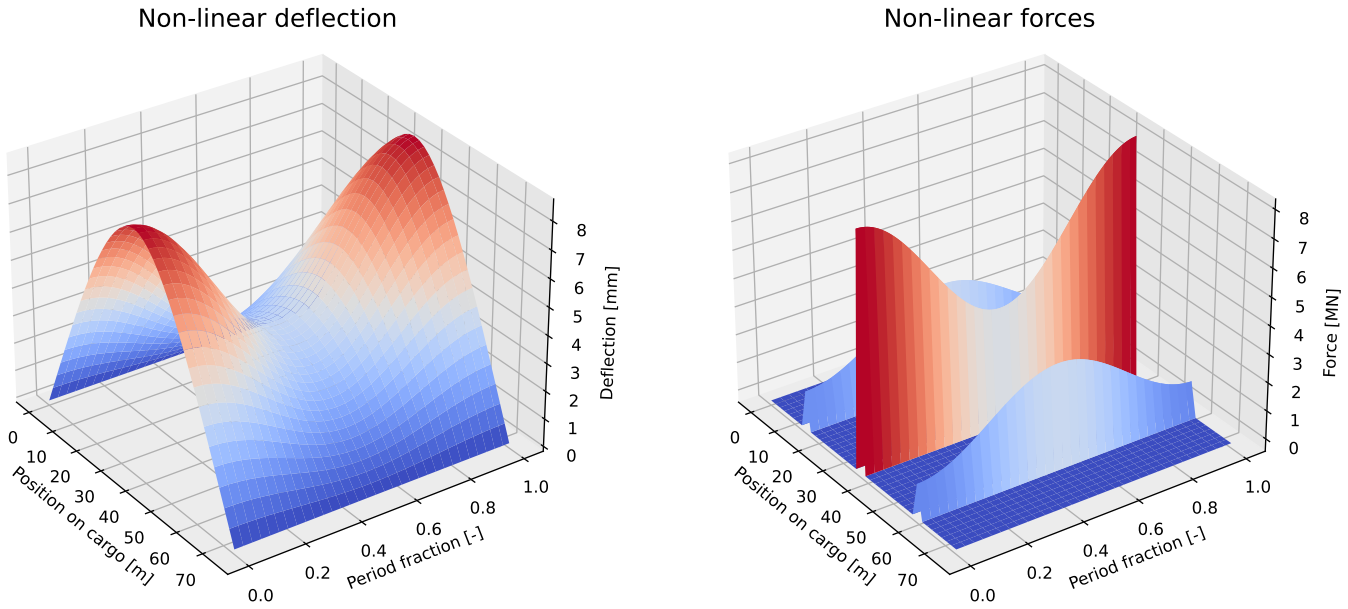

Figure 6.10: Deflection and forces in monopile over time analysed using the non-linear model

Table 6.6 shows a comparison between the linear and the non-linear results. This table shows good accordance between the linear and the non-linear model. Slight differences are present due to the force deflection formulation for the non-linear model.

Table 6.6: Maxima for linear dynamic loadcase using different saddle stiffnesses

Parameter		Linear	Non-linear	Unit
Deflection monopile	u_c	8.5	8.6	mm
Deflection saddle	u_s	7.6	7.7	mm
Detachment	u_d	-	0	mm
Force sea-fastening	F_{sf}	8.1	8.2	MN
Bending moment	M_b	70.5	71.6	MNm
Bending stress	σ_b	18.1	18.3	MPa

Another comparison is made in figure 6.11. The percentual difference figure for the deflection of the monopile shows a limited error, staying below 2 percent. This error originates from the saddle force deflection formulation, causing the error shown in the right figure. Note that this error only becomes pronounced for small forces, in the region where small deflections are present. This indicates that the effect on the structural response is limited, because of the force being small where the error becomes pronounced.

At last, the shape of the deflection error can be explained again by the deflections of the saddles. Figures 6.9 and 6.10 show that where the error in deflection is smallest, corresponds with the location where the forces of all three saddles is pronounced. This indicates that the deflections of the saddles are also significant.

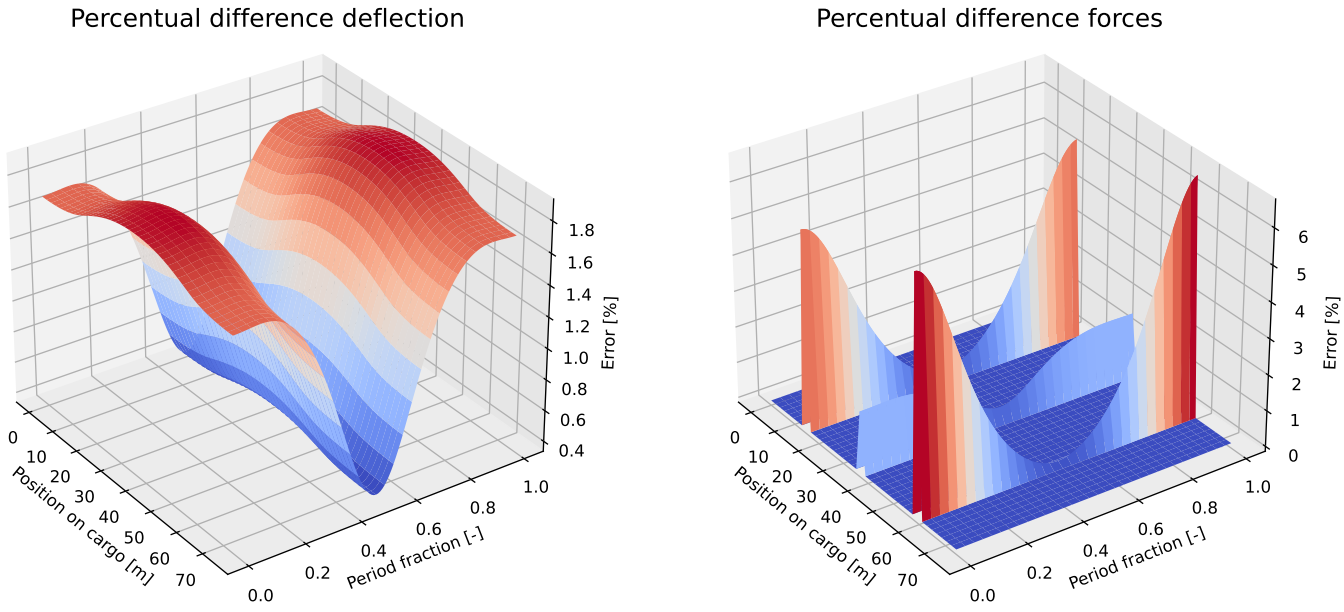

Figure 6.11: Percentual difference between deflections and forces using linear and non-linear analysis

6.1.3. Dynamic analysis with non-linear behavior

For this analysis, a load amplitude is chosen where nonlinearities, or loss of contact, occurs at one of the saddles. Therefore, the wave amplitude is increased to 3 meters, while keeping the other parameters shown in table 6.5 the same. This analysis starts with analyzing the forces and deflections in the sea-fastening system. The figures shown in figure 6.12 show these forces for the linear and non-linear analysis, for which a difference starts to originate. The figure on the left shows the linear analysis, where a negative normal force is observed for the saddles located at $0.2L$ and $0.8L$ of the monopile at the beginning of the oscillation. This implies that over there contact would be lost with the saddle.

For the non-linear analysis a different force distribution within the sea-fastening system is observed. Here a positive normal forces are observed for the saddles located at $0.2L$ and $0.5L$, but a normal force of zero is observed for the saddle located at $0.8L$ of the monopile. Because this saddle is not able to apply a negative force on the monopile, it results in the situation where it rotates and rests on the first two saddles.

Furthermore, these figures also show that a lower force is observed for the non-linear analysis. This confirms that modeling this particular case in a linear manner would indeed overconstrain the problem and justifies a non-linear approach.

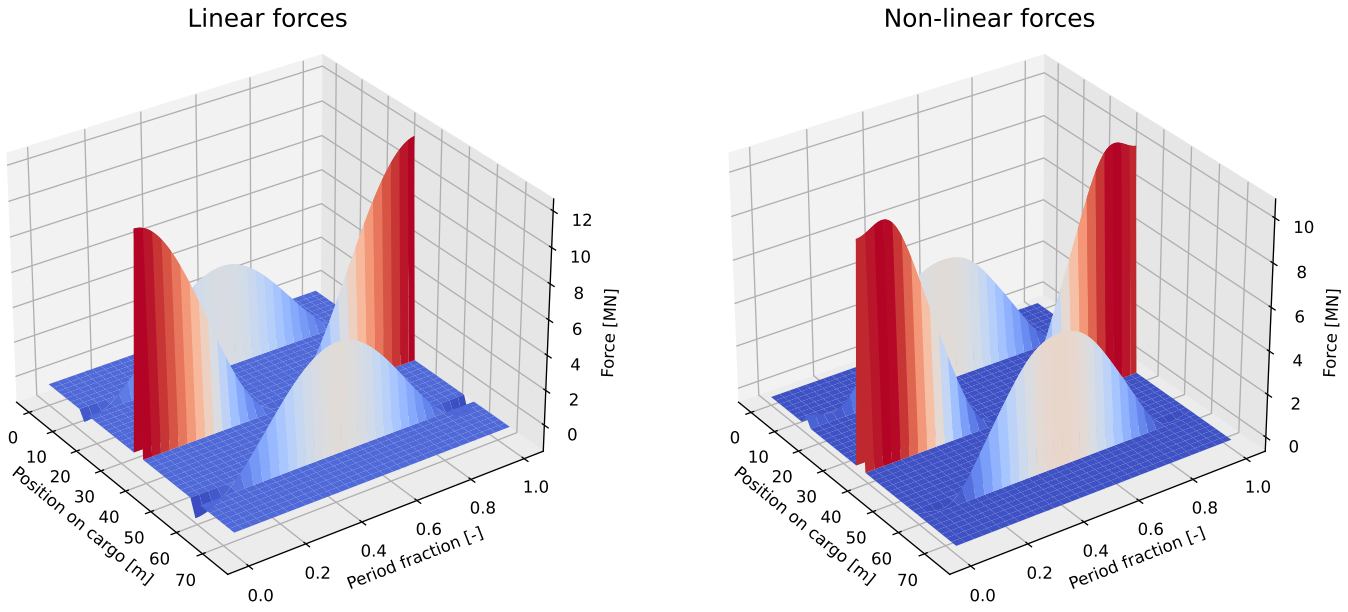

Figure 6.12: Forces in sea-fastening system for linear and non-linear analysis

Table 6.7 shows a summary of the results for the non-linear dynamic analysis. The results show that for the non-linear dynamic case a linear approach leads to a 20 percent increase in the observed maximum bending moment in the cargo. The observed detachment however is relatively small compared to the dimensions of the saddles. Therefore, it is assumed that the effect of this detachment is limited with respect to impact dynamics. The effect of this loss of contact could have a large effect on the friction constraint of the monopile. It is not clear whether this loss of contact area is compensated for by the increase in normal force in the other saddles.

Table 6.7: Maxima for dynamic loadcase using different models

Parameter		Linear	Non - Linear	Unit
Deflection monopile	u_m	13.4	11.4	mm
Deflection saddle	u_s	11.5	9.9	mm
Detachment	u_d	-	8.4	mm
Force	F	12.4	10.6	MN
Bending moment	M_b	115.6	97.4	MNm
Bending stress	σ_b	29.6	25.0	MPa

Figure 6.13 shows a comparison between the linear and non-linear defined deflection and forces. In this situation the choice is made to plot the absolute difference, because for some areas of the solution the deflection and forces are close to 0. This creates artificial peaks in the percentual difference graphs.

Both the deflection and the force graph show that the difference becomes pronounced for the areas where the linear solution overconstrains the problem, at the beginning and end of the period. In the area where contact between the cargo and saddles is preserved, the absolute difference is observed to drop to a low level. An oscillation of a small magnitude is visible there, caused by the non-linear force and deflection formulation using harmonics.

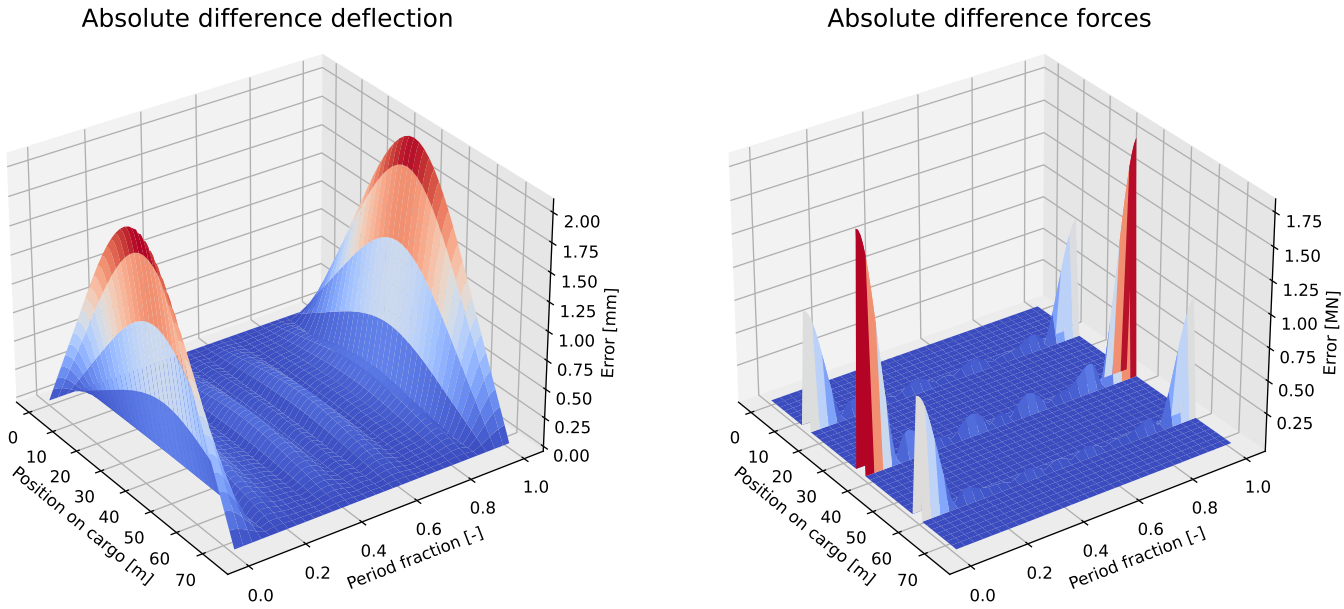

Figure 6.13: Absolute difference between deflections and forces using linear and non-linear analysis

Analysis negative non-linear forces

When analyzing figure 6.12 in more detail, it can be observed that just after the beginning and before the end of the oscillation a slight increase of the normal force of the middle saddle is observed. After analysis it became clear that this is caused by the formulation of the spring stiffness. Figure 6.14 illustrates this problem, here the deflections, time and frequency domain force of the saddle located at $0.8L$ of the monopile is shown. Due to the regularization of the spring force, it is still allowed to have a tensile normal force for a small negative deflection. Note that to obtain this result a summation of five harmonics was required.

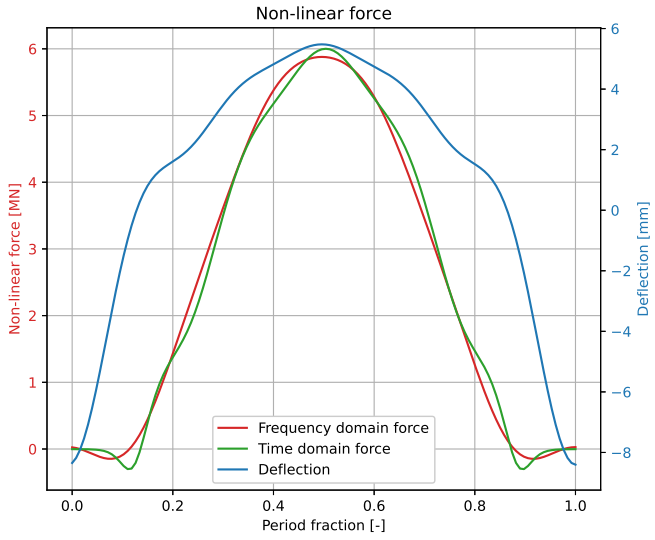

Figure 6.14: Forces and deflection observed at saddle located at $0.8L$ of monopile

Note that due to this tensile normal force observed the maximum force and bending moment for the non-linear analysis shown in table 6.7 are overestimated. The same conclusion can be drawn based on only a one-way coupling being considered in the model.

Analysis detachment

With the behavior observed in the force distribution of the sea-fastening system the deflections observed in the system can be analyzed. Figures 6.15 show the dynamic deflections of the cargo, for the linear and non-linear analysis. The linear analysis shows the negative deflection at the front and aft saddles, leading to the observed tensile normal force. The non-linear deflection shows the magnitude of detachment for the saddle located at $0.8L$ of the monopile.

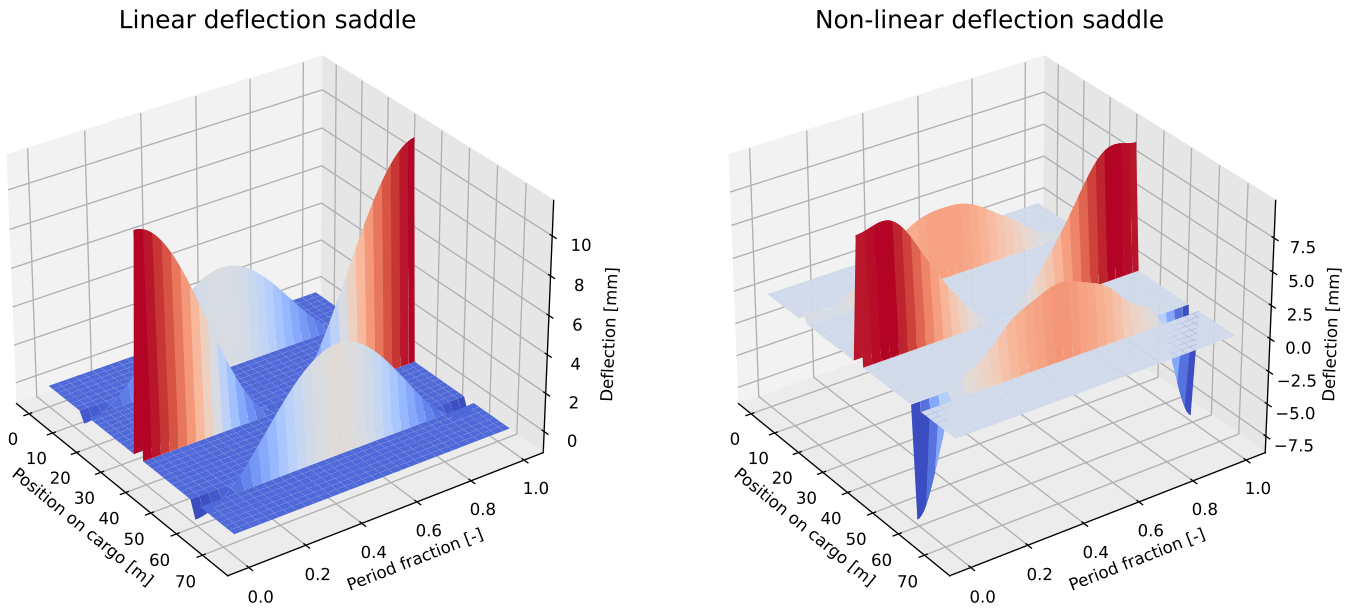

Figure 6.15: Deflection of saddles in sea-fastening system for linear and non-linear analysis

The situation regarding the disconnection is analyzed more thoroughly at the time instance $t = 0$, so at the beginning of the oscillation. This is because the magnitude of the disconnection directly becomes pronounced, being almost equal to the saddle deflection. Figure 6.16 shows the deflection of the vessel and cargo at time instance $t = 0$. These figures show that in the linear system the contact at the saddle located at $0.8L$ is preserved by rotation and additional bending of the cargo. The rotation of the beam in particular causes the magnitude of detachment observed for the non-linear model, as shown in the right figure for the most right saddle.

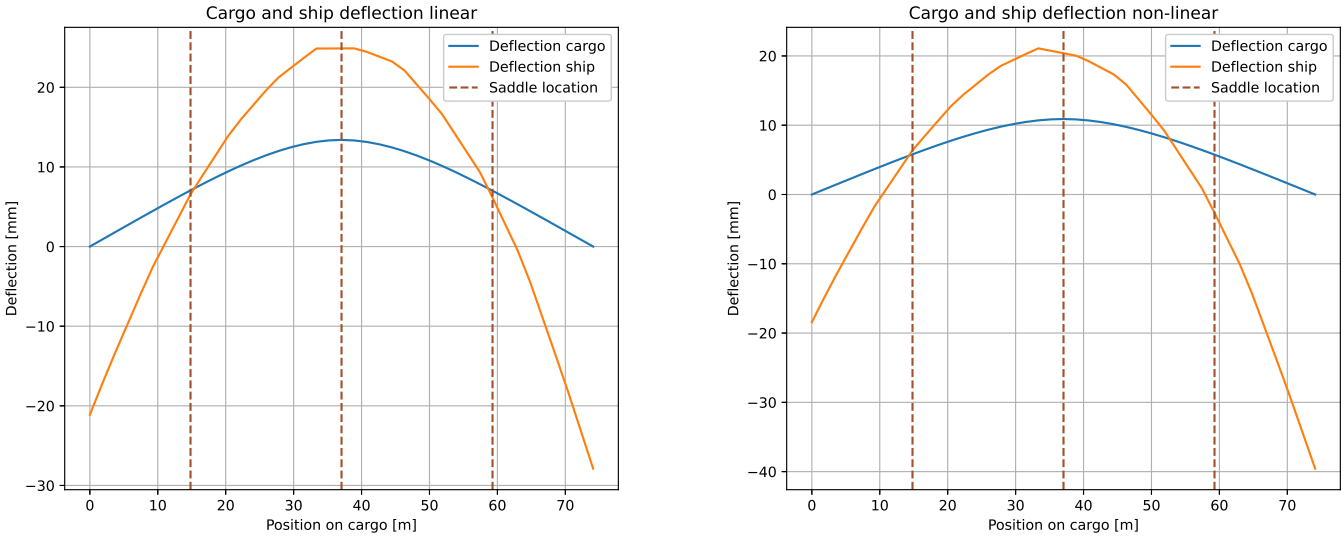

Figure 6.16: Deflection of ship and cargo for the linear and non-linear analysis at time instance $t = 0$

The main conclusions drawn from the analysis up to now are summarized as follows:

- The hydrodynamic model showed that the loads caused by the deflection of the vessel exceed the loads caused by accelerations.
- The static analysis shows that the deflections are small in comparison to the dimensions of the cargo and saddles.
- The static analysis also shows that slight changes in forced deflection can lead to a large difference in force distribution.
- The non-linear dynamic analysis shows that for dynamic situations with large deflections nonlinearities indeed occur and that a linear approach leads to an overconstrained situation.

6.2. Parametric analysis sea-fastening system

In order to better understand the response of the cargo and the distribution of forces within the sea-fastening system, some different cases will be investigated. The influence of the sea-fastening system is first analyzed. Within this analysis, the cargo is kept constant, being equal to the monopile considered in paragraph 6.1. A certain sea-fastening system is selected based on this analysis, which is used after in a further investigation. Within this analysis the dimensions of the cargo are varied, with the sea-fastening system being kept constant.

6.2.1. Parametric analysis saddles

Table 6.8 shows the different cases considered with the variations applied on the sea-fastening system. At first, the number of saddles and saddle stiffness is varied over a certain range. During this analysis the loadcase and lashing properties are kept constant.

Table 6.8: Loadcases considered

Parameter		Min. value	Max. value	Unit
Number of saddles	$N^o sad$	2	7	-
Saddle stiffness	k_{sad}	10^{-2}·1.1	10^{1}·1.1	GNm

Within this analysis the saddles are placed using equidistant spacing over the length of the monopile. An example of this is shown in figure 6.17 for 3 saddles.

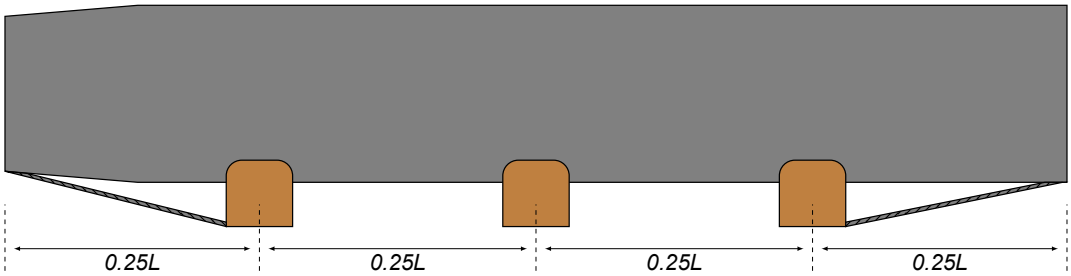

Figure 6.17: Schematic overview sea-fastening system with equidistant saddle configuration

Figure 6.18 shows the results of the analysis for the forces in the sea-fastening system and bending moment in the cargo. The brown area shown in the plot shows the region of saddles and saddle stiffness where contact for all saddles is preserved, indicating that linear theory can still be applied. Note that for 2 saddles no detachment is present for any stiffness, indicating that this situation can be described by linear theory. This is in accordance with the expected behavior.

These figures show that for an increasing saddle stiffness the forces in the sea-fastening system and bending moment in the cargo increases. For 5 saddles in combination with the highest saddle stiffness, some strange behavior is observed. This case shows a normal force of 14 MN compared to 12.8 MN, found for the linear model. This situation is analyzed further in depth in appendix I. The main conclusion here is that the error made by the regularization, as shown in figure 6.14, is amplified by increasing the spring stiffness. This increases the tensile force applied by the saddle, resulting in this increased normal force.

Another observation are the peaks in maximum normal force and maximum bending moment for an odd number of saddles. This is a result of the equidistant saddle definition. For an odd number of saddles there will be one located at $0.5L$ of the monopile, resulting in it carrying the largest load.

At last, another trend is shown that for an increasing number of saddles the non-linear behavior starts to occur at an earlier stiffness. This is in accordance with the expected behavior, since the monopile overspans a shorter length between the saddles. Therefore, the deflections of the monopile under its own weight start to become small, indicating that loss of contact occurs earlier.

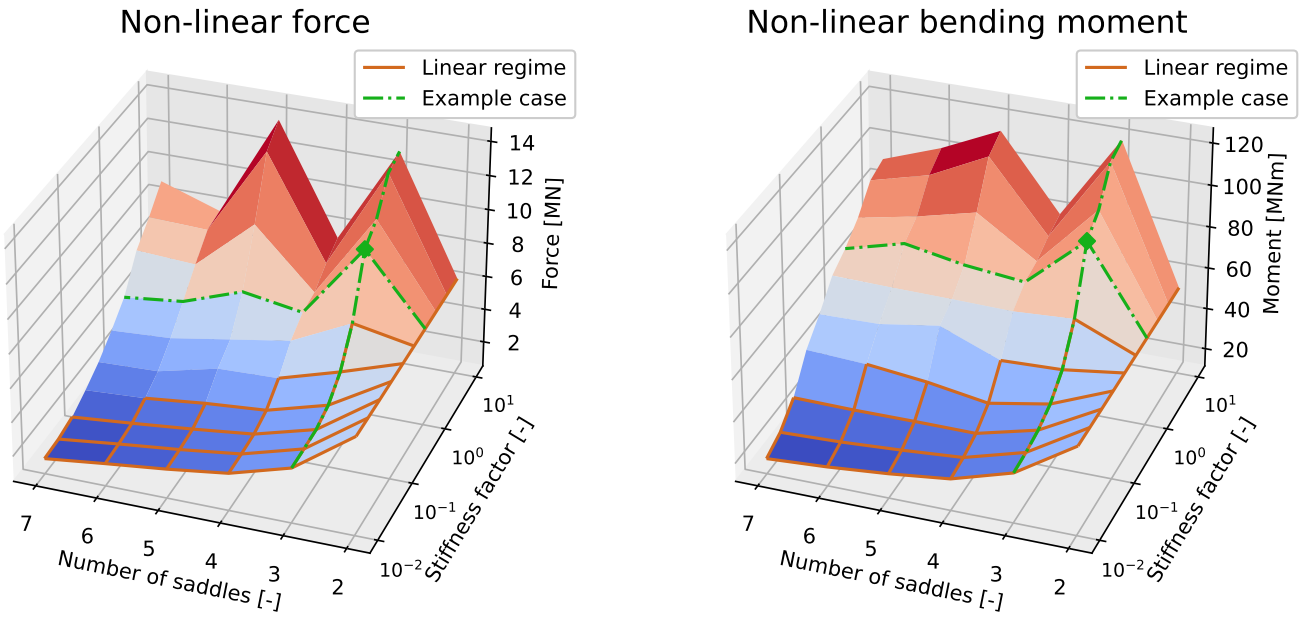

Figure 6.18: Influence of number of saddles and saddle stiffness on maximum force in sea-fastening system and maximum bending moment in cargo using non-linear model. Brown area indicates domain where contact is preserved and linear theory applies.

From a structural integrity and fatigue damage point of view it is desired to have a large number of saddles in combination with a low saddle stiffness. The weight of the monopile can be spread by a large number of saddles, leading to lower forces. Low saddle stiffness is desired to compensate for the bending deflections of the vessel, to ensure that a limited amount is transferred to the cargo. This has a significant effect on the loads in the cargo, which is in accordance with the analysis performed in section 4.3. This analysis showed that the loads experienced by the cargo are dominated by bending induced loads of the vessel in comparison to inertial loads resulting from accelerations.

Lower structural response case

Figure 6.19 shows a comparison between force distribution for the base case and a situation where 4 saddles are applied, at 10 percent of the stiffness of the original saddles. Note that in the situation with 4 saddles contact between the monopile and saddles is preserved, which implies that linear modeling can be applied. The results related to the force distribution and other results are summarized in table 6.9. Based on the figures and table two main conclusions can be drawn. At first, the maximum force in the sea-fastening system drops by almost 70%, from 10.6 to 3.3 MN. This decrease in force comes at the cost of an increased deflection, which increases approximately by 300 %.

Table 6.9: Comparison of maxima for example case to case with 4 saddles and 10 % saddle stiffness

Parameter		**3 Saddles - 1 k$_{sad}$**	**4 Saddles - 0.1 k$_{sad}$**	**Unit**
Deflection monopile	u_m	11.4	6.0	mm
Deflection saddle	u_s	9.9	32.6	mm
Detachment	u_d	8.4	0	mm
Force	F	10.6	3.3	MN
Bending moment	M_b	97.4	37.7	MNm
Bending stress	σ_b	25.0	9.6	MPa

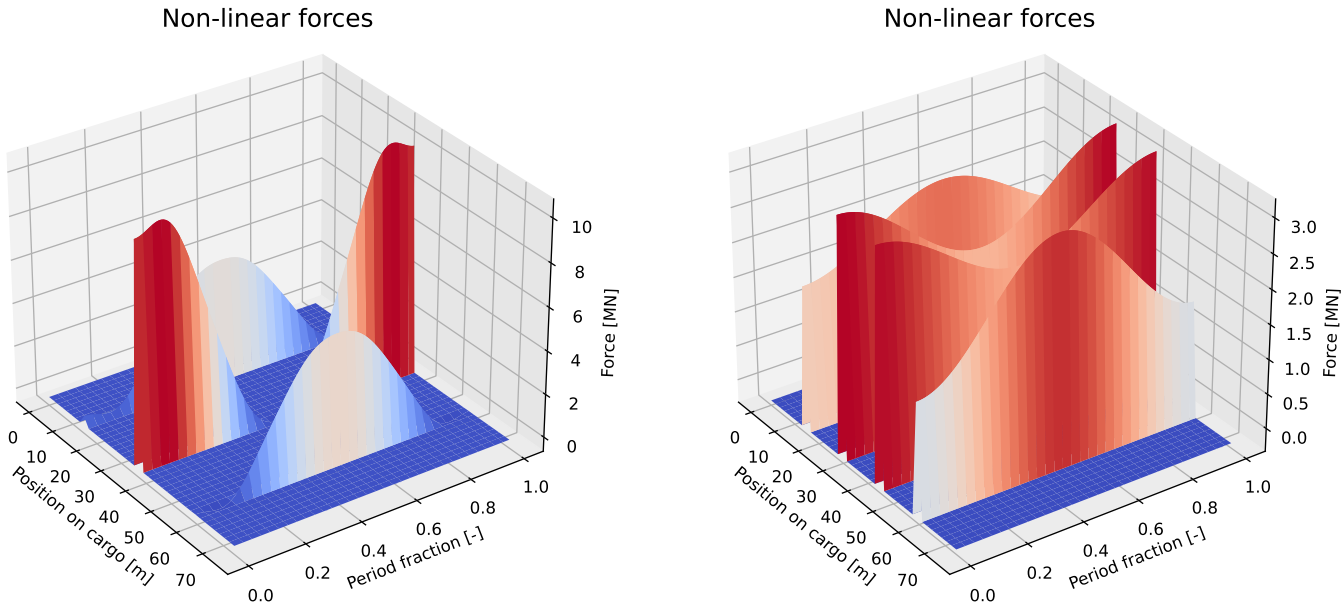

Figure 6.19: Comparison of forces for example case using 3 saddles with 100 % saddle stiffness to situation using 4 saddles in combination with 10 % saddle stiffness

Limit case

One final case which has been investigated is the limit case, so where 7 saddles are used in combination with 0.006 stiffness factor. The results are shown in figure 6.20. This figure shows that, for this case, almost no bending is present anymore for the monopile. The forces in the system are more defined by the inertial forces, instead of the forced bending deflections. Appendix J shows additional results for this case. Using this saddle stiffness the axial deflections of the saddles navigate into the same order of magnitude as the bending deflections of the vessel.

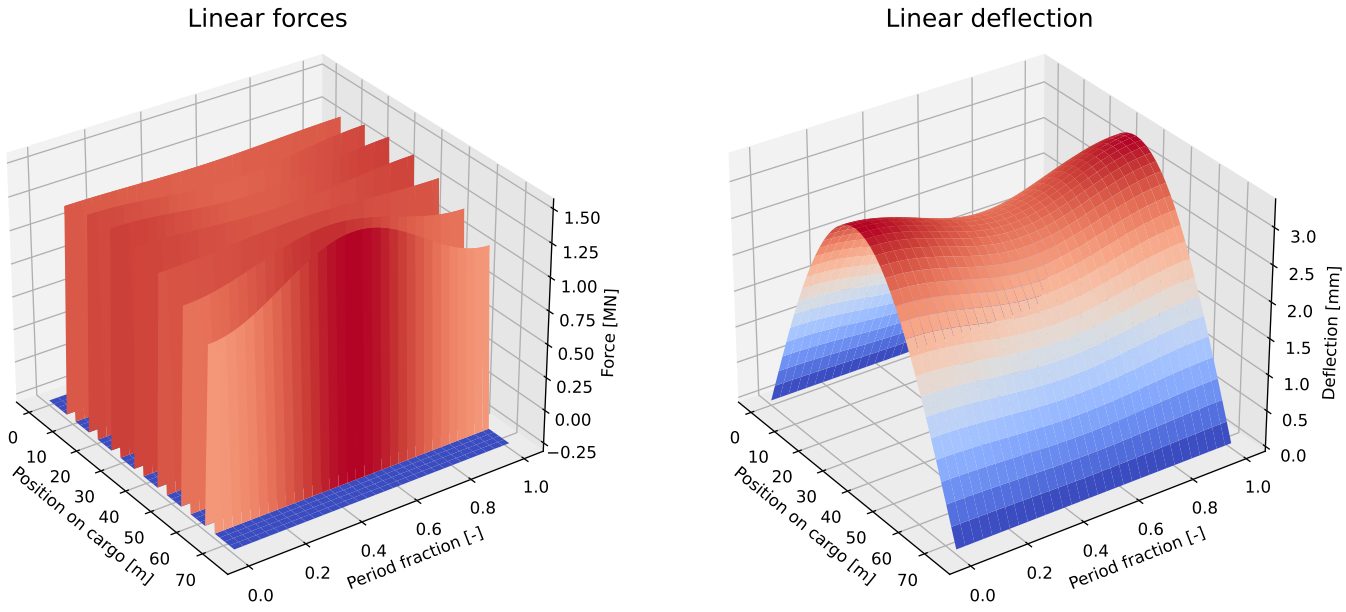

Figure 6.20: Behavior of system for 7 saddles in combination with a 0.006 stiffness factor

Appendix H shows additional results for this parametric analysis. Here the difference between a linear and a non-linear approach becomes visible for the situation where detachment occurs, and it shows that this difference becomes significant. Figure 6.18 shows that for the considered domain there exists a maximum around a force of 14 MN and a bending moment of 120 MNm. For the linear analysis this force increases to 25 MN, and the bending moment to 250 MNm.

Based on the saddle parametric analysis the following can be concluded:

- In general, a large number of saddles leads to better force distribution within the sea-fastening.
- For a constant saddle stiffness a larger number of saddles can lead to detachment of the monopile at certain locations in the sea-fastening system.
- A lower saddle stiffness leads to bending loads from the vessel being compensated by the deflection of the saddle. This results in lower loads experienced by the cargo.

6.2.2. Parametric analysis lashing

Another parametric study is performed to investigate the influence of lashing on the dynamic behavior of the cargo. To do this, the number of saddles and the stiffness of the saddles are kept constant, equal to the sea-fastening system presented in section 6.1. Table 6.10 shows the range for which the parametric study is performed.

Table 6.10: Loadcases considered

Parameter		Min. value	Max. value	Unit
Lashing stiffness	k_{lash}	1e4	1e7	N/m
Pre-tension applied	T_{lash}	1e4	1e8	N

Figure 6.21 shows the non-linear maximum force and the bending moment for the parametric analysis considered. Note that based on visibility considerations the x- and y-axis for the non-linear force plot are flipped. Both figures show that for a large part of the domain the lashing stiffness and pre-tension does not influence the forces and bending moment in a significant manner. The domain spans approximately

10^4 to 10^6 N and N/m. This behavior can be explained by the resulting lashing forces being small in comparison to the normal forces present in the system.

In addition, the figure also shows that for larger stiffness and pretension values the monopile becomes more constrained, leading to smaller saddle forces and a larger maximum bending moment. It seems counterintuitive that the maximum normal force decreases, but this is caused by the bending induced by the lashing wires. This causes the monopile to bend to such an extent that the contact with the first and last saddle is restored again. Further details and an example case are presented in appendix L.

The non-linear normal force plot shows a slight increase for higher stiffness and pretension values. After investigation it became clear that this is caused by the spring formulation for the saddles, here a small negative deflection is present leading to a small tensile force. This causes the normal force in the middle saddle to increase by 5 percent, which is visible in the force plot.

Finally, it should be emphasized that it is unlikely that the domain of stiffness and pretension around 10^7 and 10^8 will be reached in reality. This would indicate a lashing stiffness that is 300 times higher and a pretension that is 500 times higher than applied in this project. Still, it is useful to see what happens when the limits of pretension and stiffness are reached and what type of behavior could be expected there.

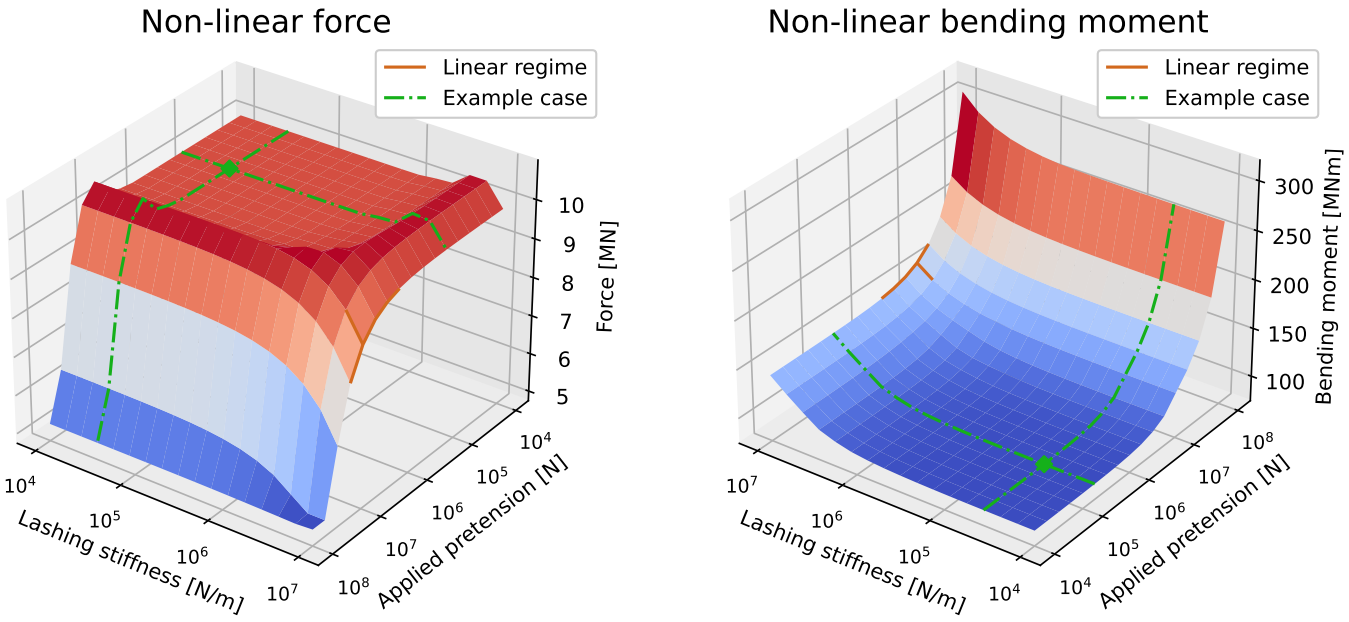

Figure 6.21: Influence of applied lashing stiffness and pretension on maximum force in sea-fastening system and maximum bending moment in cargo based on non-linear model. The brown area indicates again where contact is preserved and linear theory applies.

Appendix K shows additional results for this parametric analysis. These results highlights the difference between the linear and the non-linear results.

To summarize the following conclusion can be drawn from the lashing parametric analysis:

- Lashing stiffness and pretension does not have a significant influence on results, because of its resulting forces being small in comparison with other forces in the system.
- Extremely high stiffness and pretension values lead to a large amount of loads transferred to the cargo.

6.2.3. Parametric analysis cargo

At last, a parametric study is performed with respect to the dimensions of the cargo. In this analysis, the sea-fastening system is kept the same as presented in paragraph 6.1. The cargo considered in paragraph 6.1 is used as a starting point, and length and diameter is increased from there as shown in table 6.11. The length of the cargo is limited by the length of the cargo deck, while the maximum diameter of the cargo is chosen to be around the current maximum. Monopile producer Sif states that their maximum has a value of 11.5 meters.

For this analysis a diameter thickness ratio of 1/110 is chosen. The monopile considered in paragraph 6.1 has a ratio of 1/100, while classification societies limit this value to 1/120 [2]. For simplicity of the analysis the lashing parameters are kept the same. The prior analysis showed that its effect is limited on the response of the monopile.

Table 6.11: Cargo's considered in parametric analysis

Parameter		Min. value	Max. value	Unit
Cargo length	L_c	75	115	m
Cargo diameter	D_c	8	12	m

Figures 6.22 show the maximum force in the sea-fastening system and the maximum bending stress present in the cargo. Within this analysis, the bending stress is a better parameter to compare different cases instead of the maximum bending moment, due to the increase of inertia by an increasing diameter. Note that the axis with the diameter of the monopile is flipped for the bending stress figure, because of visibility reasons.

The figure shows that both force and stress increase with increasing monopile length. This behavior is expected since the weight of the monopile is larger. For the bending stress this was expected as well, because of the increased distance between saddles. For an increase in diameter, different behavior is identified for the forces and stress. The increase in force is again due to the increase in weight of the monopile. But an increase in diameter leads to a decrease in stress, because the increase in inertia exceeds the increase in weight.

At last, the increase in weight for a combination of a large length and a large diameter leads to the deflection of the monopile becoming large. Therefore, it is observed that, for this part, linear theory is again valid, because of the deflections of the monopile becoming so large that contact is preserved.

[2] https://www.empireengineering.co.uk/how-far-can-we-push-d-t-ratios/

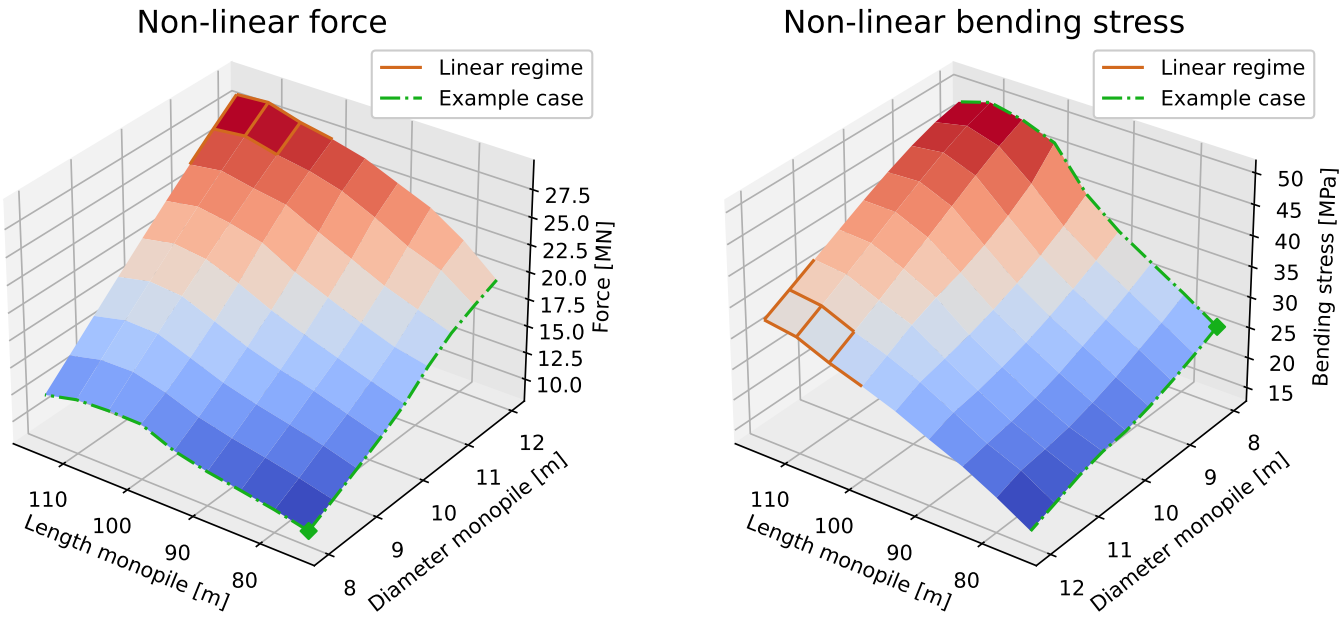

Figure 6.22: Influence of length and diameter of cargo on the forces observed in the sea-fastening system and the bending stress in the cargo. The brown area indicates again where contact is preserved and linear theory applies.

The main conclusions that can be drawn here is that the forces in the sea-fastening system grow according to the weight of the monopile, caused by increase in length or diameter. The stresses in the cargo increase proportionally to the distance between the saddles, but decrease with an increase in the cargo's diameter.

Further results corresponding to this analysis are shown in appendix M. These plots show the area where the detachment is largest and the area where the difference between the linear and non-linear results is most pronounced.

Case analysis

Based on these conclusions, two additional cases are identified to further analyze in detail. For these 2 cases the parametric saddle analysis is performed again, in order to evaluate to what extent the behavior identified there still holds for longer and more stiff cargo. The selected cases are the situation that leads to the highest force and stress, shown in table 6.12.

Table 6.12: Monopile cases selected to perform parametric saddle analysis

Parameter		Case 1	Case 2	Unit
Monopile length	L_c	115	115	m
Monopile diameter	D_c	8	12	m

In addition, some constraints are posed. For example, the vessel operator could set an upper limit for the maximum force transferred by the saddles. This could be based on deck strength considerations. The requirement could also originate from a maximum local force which can be applied at the monopile. This requirement is influenced by the trend of lower diameter-to-thickness ratios observed for monopiles. Another example of an upper limit could be related to the bending stress in the cargo. The origin of this requirement can be related to fatigue damage to the monopile resulting from transport.

Table 6.13 shows the maximum values identified for the forces in the sea-fastening system together with the maximum bending stress in the monopile. The maximum normal force is based on the example

project considered. Here in the analysis a maximum around 7 MN was identified. This analysis should define if these maxima can be attained for longer and larger monopiles.

Furthermore, the maximum bending stress is set to approximately 10 percent of the yield stress, for mild steel.

Table 6.13: Upper limits for structural response parameters

Parameter		Value	Unit
Saddle force max.	F_{max}	7	MN
Bending stress max.	$\sigma_{b,max}$	20	MPa

Figure 6.23 shows the results for a diameter of meters, with a length of 115 meters. If compared to figures 6.18 a similar trend is visible, being that the structural response decreases for an increased number of saddles in combination with a decrease in saddle stiffness.

In addition, this figure shows that it is possible to use many different saddle configurations to comply with the above mentioned upper limits. Note that the number of configurations in this situation is limited by the bending stress. This implies that more cases can be identified where the forces in the sea-fastening system stay below 7 MN, but there the bending stress becomes larger than 20 MPa. Based on this information an optimum configuration can be selected, related to material or production costs or other factors.

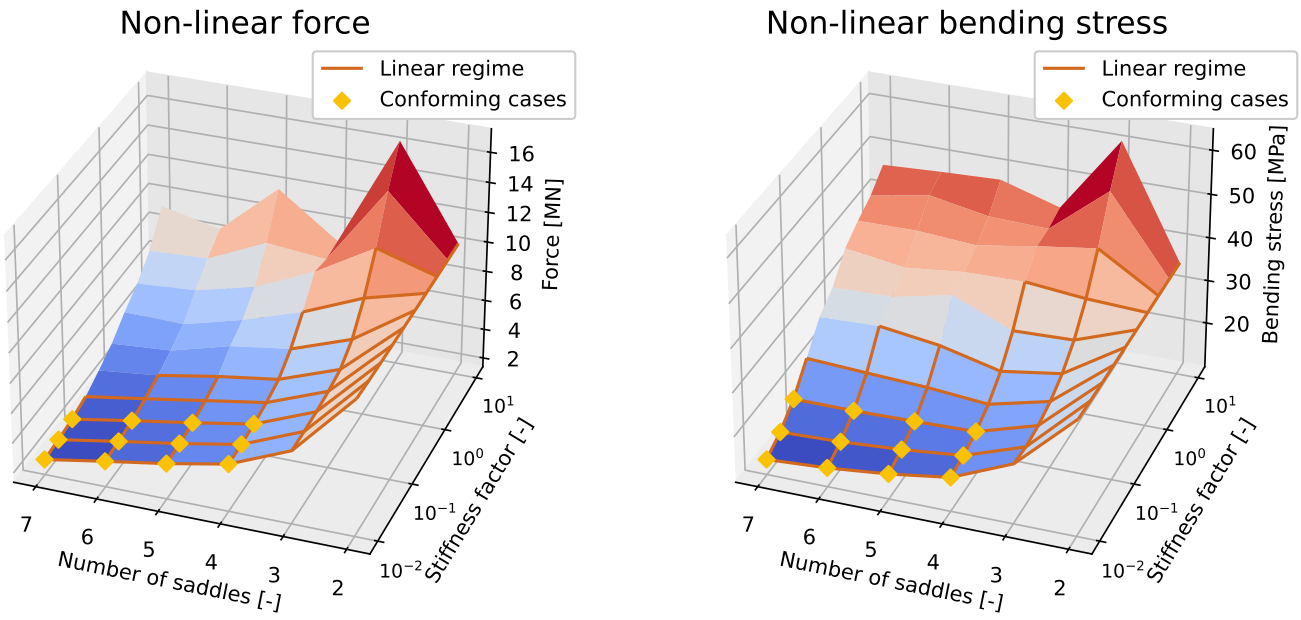

Figure 6.23: Influence of number of saddles and saddle stiffness on maximum force in sea-fastening system and maximum bending moment in monopile with a diameter of 8 meter using non-linear model. The brown area indicates domain where contact is preserved and linear theory applies. The yellow dots represent the cases where both the forces in sea-fastening system and bending stress in the monopile stays below the limits defined in table 6.13.

Figure 6.24 shows the same results, but then for a monopile diameter of 12 meters. Here the same behavior is observed, but a lower variety in configurations can be selected. This indicates that to comply with the force upper limit, more saddles are required to carry the weight. The higher normal force is caused by the increase in weight of the monopile. The bending stress figure shows that cases are not limited by the imposed bending stress criterion, caused by the increased inertia of the monopile.

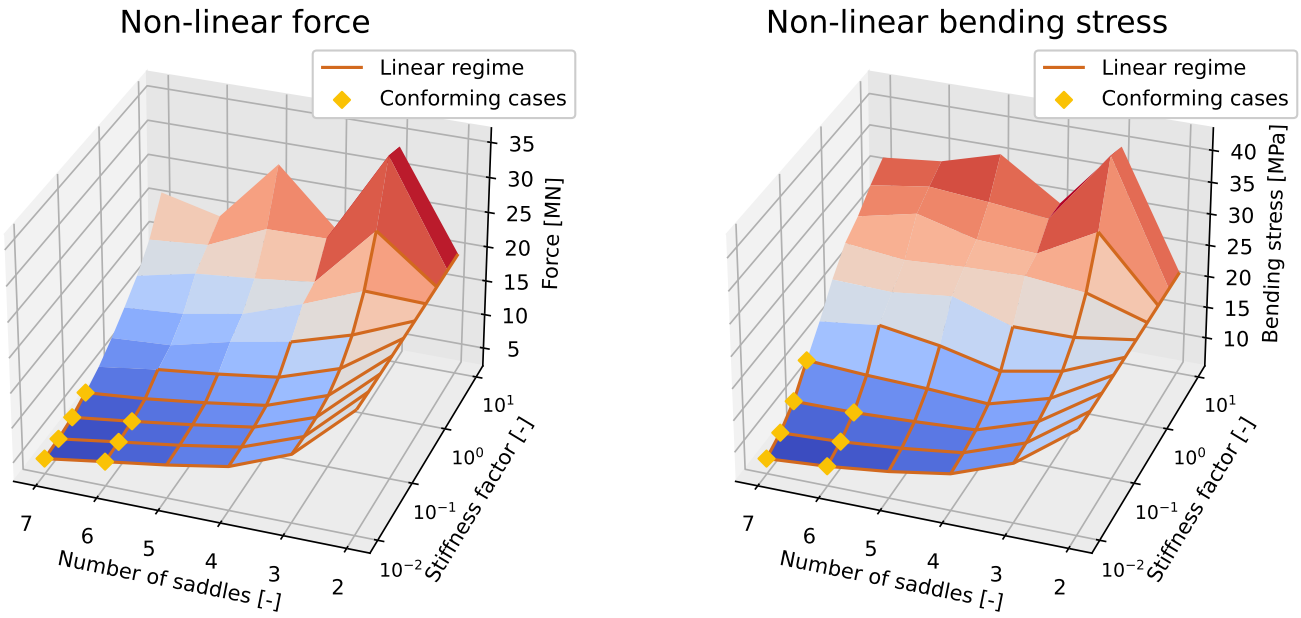

Figure 6.24: Influence of number of saddles and saddle stiffness on maximum force in sea-fastening system and maximum bending moment in monopile with a diameter of 12 meter using non-linear model. The brown area indicates the domain where contact is preserved and linear theory applies. The yellow dots represent the cases where both the forces in sea-fastening system and bending stress in the monopile stays below the limits defined in table 6.13.

Note that the analysis performed here is intended to identify and highlight behavior related to the sea-fastening system. Further research should identify cargo cases, hydrodynamic loadcases and structural response criteria, which would be worth investigating. The main conclusions that can be drawn from the cargo parametric analysis are summarized as follows:

- Increasing cargo length and diameter showed that the same behavior can be observed for longer and more stiff cargo as in the saddle analysis.
- The model is able to identify sea-fastening arrangements for which the structural response complies to certain upper limits.

6.3. Informed sea-fastening design

This section presents a brief description of how the observed behavior in the static, dynamic, and parametric analysis can help design sea-fastening arrangements. For this sea-fastening design procedure maximum saddle force and maximum bending stress are chosen to be the design limitations. Figure 6.25 shows a flow chart which should aid in decision making when designing sea-fastening arrangements.

This figure shows that if the bending stress constraint is not met, at first an attempt should be made by creating a more equidistant saddle spacing. If the limits are reached here, the saddle stiffness should be lowered. This has to be done iteratively until the limit, to identify if a solution exists here. In case no solution exists and the limit of the saddle stiffness is reached, an extra saddle should be added. This iteration should be performed until a solution is found. Note that in case when boundary conditions are posed to strict no solution may exist.

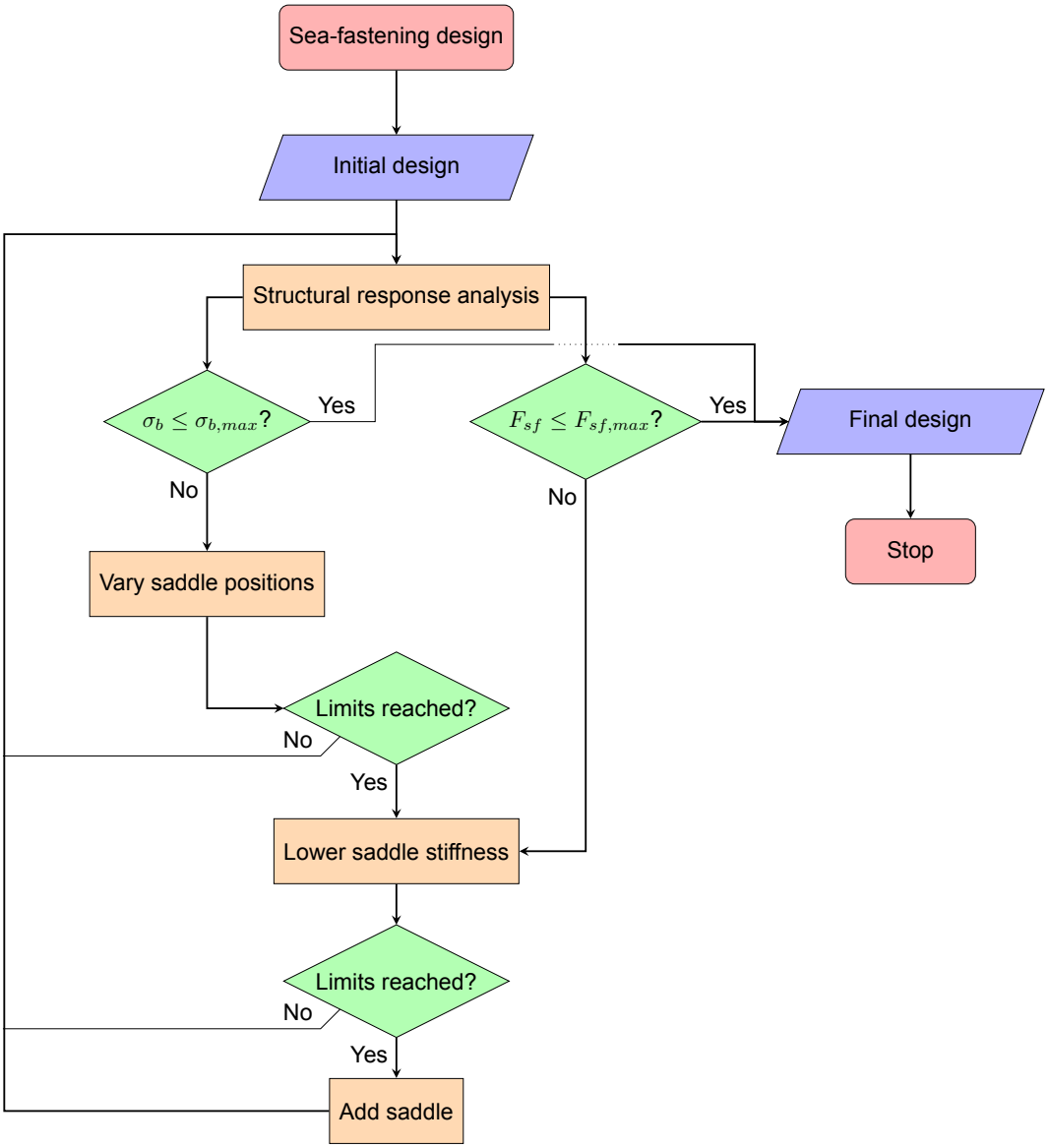

Figure 6.25: Example of workflow that could be applied when designing sea-fastening arrangements. A structural response analysis should define whether the system complies with a maximum bending moment and force. In case the maximum bending moment does not comply, the saddle positions could be changed to a more equidistant spacing. If this is not sufficient to meet the posed boundary condition, the saddle stiffness should be lowered. When both the limits of the equidistant saddle spacing and saddle stiffness are reached, a saddle should be added. This iteration should be performed until both constraints are satisfied.

7

Conclusion and Recommendations

The main findings, conclusions, and recommendations are presented in this chapter. At first, a concise answer is presented on the sub-questions and the research question. After that, some recommendations are presented for future work related to improving the modeling and related to better understanding related behavior.

7.1. Conclusions related to sub-questions

At first, an answer is presented for every sub-question, leading to the formulation of an answer to the main research question. The answers to the sub-questions are as follows:

1. In what manner can the interactions between the vessel and cargo be modeled using non-linear constraints imposed by the sea-fastening system?

The static analysis showed that the structural response in the ship-cargo system is highly influenced by the axial deflection of the saddles. This indicates that the quality of the results is defined by the accuracy of modeling a correct force corresponding to a correct deflection. Different force-deflection formulations showed that a regularization approach gives the most accurate results in combination with good convergence behavior.

2. How does the bending of the cargo contribute to additional loads experienced in the ship and sea-fastening system?

The system is sensitive to the bending deflection of the ship, the axial deflection of the saddles and bending deflection of the monopile under its own weight. Important to note here is that the loads become pronounced when the bending deflection of the vessel is greater compared to the bending deflection of the cargo under its own weight. This results in large forces in the sea-fastening system, which are transferred to the ship. For the example case a limit of approximately the own weight of the monopile can be identified. The inertial contribution due to accelerations was small.

3. What is the influence of sea-fastening on the structural dynamic response of the cargo and sea-fastening and how can connection be ensured?

The parametric analysis showed that the most influential parameters are the saddles in combination with their stiffness. This in assumption that the combination of the stiffness and weight of the cargo cause it to have very small deflections. These paramaters define the magnitude of the bending moment in the cargo, the magnitude of the forces in the sea-fastening system and whether detachment occurs. However, Lashing stiffness and pre-tension do not influence the observed structural dynamic response, given that these stay within reasonable orders of magnitude of properties currently being applied. At last, varying these properties in an informed manner showed that certain design criteria

can be met for longer and more stiff cargo.

4. To what extent does non-linear modeling influence the observed response compared to a linear approach?

The dynamic analysis showed that for three saddles loss of contact occurs and that a linear approach overconstrains the model, leading to larger forces and bending moments. The parametric analysis showed that for a large number of sea-fastening arrangements detachment occurs, requiring a non-linear modeling approach. Note that non-linear behavior is reached earlier for a combination of a larger number of saddles with larger saddle stiffness leads. It should be emphasized that this behavior is greatly dependent on the bending properties of the vessel, the bending properties of the cargo and the applied hydrodynamic loadcase. This indicates that this behavior should be evaluated independently for every case.

"How does the interaction between a vessel and large, stiff cargo affect the structural dynamic behavior, considering the influence of non-linear constraints posed by sea-fastening?"

The structural dynamic behavior of the cargo and sea-fastening system is significantly influenced by the interactions between the ship and the cargo, as well as by the influence of the constraints posed by the sea-fastening system. The structural dynamic response is defined by the interaction of the bending deflection of the ship, the axial deflection of the saddles and bending deflection of the monopile.

This research quantifies the sensitivities of certain parameters in the sea-fastening system with respect to deflections, forces, bending moments and stresses. Differences in results for a linear or a non-linear approach are analyzed in depth.

7.2. Recommendations for future work

This section presents recommendations for future research. These recommendations are divided into recommendations to be used in continuation and for improvement of this research. At first, some recommendations are presented that are relevant when continuing with the conclusions of this research.

Continuation on conclusions

At first, an important next step could be investigating the influence of frictional constraints. This study showed that the normal force of saddles can vary significantly in dynamic situations, with even loss of contact occuring between the saddle and cargo. It would be valuable to better understand this behavior by extending the model with the axial direction of the cargo, and by implementing friction constraints present at the saddles. Understanding of structural dynamic response of the system would help identify critical situations and aid in sea-fastening arrangement design.

Furthermore, applied research should investigate the possibilities of how saddle stiffness can be decreased, while maintaining structural integrity and fatigue lifetime. This research should include how this can be achieved by only changing the stiffness in height direction, while the properties in port-starboard direction stay the same.

At last, by lowering the saddle stiffness caution should be paid to the sub-system is created where the monopile acts as a rigid body attached to multiple springs. This system can be defined as a mass-spring-damper system, where the monopile acts as the mass and the sea-fastening elements as the springs. The expectation is that by lowering the saddle stiffness too much the possibility exists that the eigenfrequency of the mass-spring-damper system can be excited.

Improvement of modeling

The accuracy of the results would be increased if a two-way coupling between the ship and cargo is applied. This implies that the forces created by exciting the cargo are applied again on the vessel at the location of the saddles. Note that the modeling method of the vessel should be non-linear as well, since the resulting forces of the cargo model are non-linear. These forces cause vessel deflections, lowering the load applied to the cargo. This would enable one to study the influence of large and stiff cargo on the structural dynamic response of the vessel, and the influence on the eigenfrequencies.

In addition, another part that would increase the accuracy of the model is modeling the bending deflection of the cargo deck. Knowledge from practice from BigLift states that the bending deflection of the cargo deck can be of the order of magnitude of centimeters. With the sensitivity of the dynamic response on based on deflection this could influence the observed results.

An investigation should be conducted to determine whether the regularization of the saddle force deflection curve can be performed in a more accurate manner. This research shows that, for some situations, the error can become pronounced, especially if saddles with a larger stiffness are used. An alternative approach could also be to change the solution method. The literature review showed that a mixed shooting-harmonic balance method could improve accuracy of the cargo-saddle interactions, by being able to model a non-smooth force deflection curve.

At last, improvements on the redundancy of the model could help in analyzing more complex situation. Now the model has trouble converging for some highly non-linear situation. A different solution method or better mathematical formulation could improve redundancy, enabling for more extensive research.

References

[1] "H-BLIX Offshore wind vessel availability until 2030: Baltic Sea and Polish perspective-Offshore wind vessel availability until 2030: Baltic Sea and Polish perspective Final Report," Tech. Rep., 2022. [Online]. Available: www.h-blix.com.pl.

[2] A. Fernández-Guillamón, K. Das, N. A. Cutululis, and Á. Molina-García, "Offshore wind power integration into future power systems: Overview and trends," *Journal of Marine Science and Engineering*, vol. 7, no. 11, p. 399, 2019, ISSN: 2077-1312.

[3] M. Shadlou and S. Bhattacharya, "Dynamic stiffness of monopiles supporting offshore wind turbine generators," *Soil Dynamics and Earthquake Engineering*, vol. 88, pp. 15–32, 2016, ISSN: 0267-7261. DOI: https://doi.org/10.1016/j.soildyn.2016.04.002. [Online]. Available: https://www.sciencedirect.com/science/article/pii/S0267726116300069.

[4] K. H. Chua, Y. Zhang, and D. Konovessis, "Cargo Liquefaction and Influence on Ship Stability," in *International Conference on Offshore Mechanics and Arctic Engineering*, vol. 58776, American Society of Mechanical Engineers, 2019, V002T08A054, ISBN: 0791858774.

[5] W. Chen, A. Roberts, A. Katterfeld, and C. Wheeler, "Modelling the stability of iron ore bulk cargoes during marine transport," *Powder Technology*, vol. 326, pp. 255–264, 2018, ISSN: 0032-5910. DOI: https://doi.org/10.1016/j.powtec.2017.12.006. [Online]. Available: https://www.sciencedirect.com/science/article/pii/S0032591017309610.

[6] Y. Chen, Y. Zhang, X. Tian, X. Guo, X. Li, and X. Zhang, "A numerical framework for hydroelastic analysis of a flexible floating structure under unsteady external excitations: Motion and internal force/moment," *Ocean Engineering*, vol. 253, p. 111 288, 2022, ISSN: 0029-8018. DOI: https://doi.org/10.1016/j.oceaneng.2022.111288. [Online]. Available: https://www.sciencedirect.com/science/article/pii/S0029801822006825.

[7] T. P. Rocha, R. Dotta, D. P. Vieira, P. C. d. Mello, E. B. Malta, and K. Nishimoto, "Experimental investigation on the influence of liquid cargo in floating vessels motions," in *OTC Brasil*, OnePetro, 2015.

[8] J. J. Park, H. Kawabe, M.-S. Kim, B. W. Kim, and M. K. Ha, *Numerical sloshing assessment including tank sloshing and ship motion coupling effect*. Jun. 2010, vol. 3, pp. 237–243.

[9] S. Mitra, C. Z. Wang, J. N. Reddy, and B. C. Khoo, "A 3D fully coupled analysis of nonlinear sloshing and ship motion," *Ocean Engineering*, vol. 39, pp. 1–13, 2012, ISSN: 0029-8018. DOI: https://doi.org/10.1016/j.oceaneng.2011.09.015. [Online]. Available: https://www.sciencedirect.com/science/article/pii/S0029801811002095.

[10] H.-W. Lee and M.-I. Roh, "Review of the multibody dynamics in the applications of ships and offshore structures," *Ocean Engineering*, vol. 167, pp. 65–76, 2018, ISSN: 0029-8018. DOI: https://doi.org/10.1016/j.oceaneng.2018.08.022. [Online]. Available: https://www.sciencedirect.com/science/article/pii/S0029801818315178.

[11] N. Ku and M.-I. Roh, "Dynamic response simulation of an offshore wind turbine suspended by a floating crane," *Ships and Offshore Structures*, vol. 10, no. 6, pp. 621–634, 2015, ISSN: 1744-5302.

[12] H. Hatecke, S. Krüger, J. Christiansen, and H. Vorhölter, "A fast sea-keeping simulation method for heavy-lift operations based on multi-body system dynamics," in *International Conference on Offshore Mechanics and Arctic Engineering*, vol. 45370, American Society of Mechanical Engineers, 2014, V01AT01A032, ISBN: 0791845370.

[13] O. Solovey, A. Ben, S. Dudchenko, and P. Nosov, "Development of control model for loading operations on Heavy Lift vessels based on inverse algorithm," *Восточно-Европейский журнал передовых технологий*, vol. 5, no. 2-107, pp. 48–56, 2020, ISSN: 1729-3774.

[14] M. A. Hannan and W. Bai, “Nonlinear hydrodynamic responses of submerged moving payload in vicinity of a crane barge in waves,” *Marine Structures*, vol. 41, pp. 154–179, 2015, ISSN: 0951-8339. DOI: https://doi.org/10.1016/j.marstruc.2015.01.002. [Online]. Available: https://www.sciencedirect.com/science/article/pii/S0951833915000118.

[15] D. Mikail, “Thesis Ship-Monopile Interaction in combination with Lashings and Friction contacts Jumbo Maritime,” Tech. Rep., 2022.

[16] H. Hazim, “Vibrations of a beam with a unilateral spring. Periodic solutions-Nonlinear normal modes,” Universit{\’e} Nice Sophia Antipolis, Tech. Rep., 2010.

[17] K. Jens, “Master thesis: Fatigue Analysis of Temporary Offshore Structures using Monte Carlo Simulations,” 2022.

[18] G. Storhaug, S. Malenica, B.-K. Choi, S. Zhu, and O. A. Hermundstad, “Consequence of whipping and springing on fatigue and extreme loading for a 13000TEU container vessel based on model tests,” in *11th International Symposium on practical design of ships and other floating structures, Rio de Janeiro, Brazil*, 2010, pp. 1201–1209.

[19] S. Nordenham, *Beyond XXL–Slim Monopiles for Deep-Water Wind Farms*, 2020.

[20] S. Chartron, Z. ZHANG, X. JIN, Y. LI, and Z. ZHANG, “Evaluating and Improving Logistics Costs During Offshore Wind Turbine Construction,” *International Journal of Transportation Engineering and Technology*, vol. 4, no. 4, pp. 65–74, 2018.

[21] B. R. Sarker and T. I. Faiz, “Minimizing transportation and installation costs for turbines in offshore wind farms,” *Renewable Energy*, vol. 101, pp. 667–679, 2017, ISSN: 0960-1481. DOI: https://doi.org/10.1016/j.renene.2016.09.014. [Online]. Available: https://www.sciencedirect.com/science/article/pii/S0960148116308035.

[22] M. F. P. Jimenez, “Application of Root Cause Analysis in Marine Accident Investigation: Case Study SMIT Transport & Heavy Lift Europe,” 2010.

[23] P. Trucco, E. Cagno, F. Ruggeri, and O. Grande, “A Bayesian Belief Network modelling of organisational factors in risk analysis: A case study in maritime transportation,” *Reliability Engineering & System Safety*, vol. 93, no. 6, pp. 845–856, 2008, ISSN: 0951-8320. DOI: https://doi.org/10.1016/j.ress.2007.03.035. [Online]. Available: https://www.sciencedirect.com/science/article/pii/S0951832007001214.

[24] A. Labuschagne, N. F. van Rensburg, and A. J. van der Merwe, “Comparison of linear beam theories,” *Mathematical and Computer Modelling*, vol. 49, no. 1-2, pp. 20–30, Jan. 2009, ISSN: 0895-7177. DOI: 10.1016/J.MCM.2008.06.006.

[25] E. Carrera, A. Pagani, M. Petrolo, and E. Zappino, “Recent developments on refined theories for beams with applications,” *Mechanical Engineering Reviews*, vol. 2, no. 2, pp. 14–298, 2015, ISSN: 2187-9753.

[26] S. Hirdaris and P. Temarel, “Hydroelasticity of ships: recent advances and future trends,” *Proceedings of the Institution of Mechanical Engineers, Part M: Journal of Engineering for the Maritime Environment*, vol. 223, no. 3, pp. 305–330, 2009, ISSN: 1475-0902.

[27] G. Kastratović, N. Vidanović, V. Bakić, and B. Rašuo, “On finite element analysis of sling wire rope subjected to axial loading,” *Ocean Engineering*, vol. 88, pp. 480–487, 2014, ISSN: 0029-8018.

[28] S. S. Rao and F. F. Yap, *Mechanical vibrations*. Addison-Wesley New York, 1995, vol. 4.

[29] T. B. Ismaila, M.-J. E. Salami, R. Akmeliawati, and H. M. Alfaro, “Artificial intelligent based friction modelling and compensation in motion control system,” 2011.

[30] S. Hylarides, T. Bosman, and H. Vredeveldt, *Dictaat MT3402 Scheepstrillingen en Geluid*, Delft, 2013.

[31] R. Davis, R. D. Henshell, and G. B. Warburton, “A Timoshenko beam element,” *Journal of Sound and Vibration*, vol. 22, no. 4, pp. 475–487, 1972, ISSN: 0022-460X.

[32] L. Majkut, “Free and forced vibrations of Timoshenko beams described by single difference equation,” *Journal of Theoretical and Applied Mechanics*, vol. 47, no. 1, pp. 193–210, 2009, ISSN: 1429-2955.

[33] H. P. Gavin, “Structural Element Stiffness, Mass, and Damping Matrices,” Tech. Rep., 2020.

[34] Z. Rizvi, “Lattice Element Method and it’s application to Multiphysics,” Ph.D. dissertation, May 2019.

[35] J. E. Bolander, J. Eliáš, G. Cusatis, and K. Nagai, “Discrete mechanical models of concrete fracture,” *Engineering Fracture Mechanics*, vol. 257, p. 108 030, 2021, ISSN: 0013-7944. DOI: https://doi.org/10.1016/j.engfracmech.2021.108030. [Online]. Available: https://www.sciencedirect.com/science/article/pii/S0013794421004501.

[36] M. Attar, A. Karrech, and K. Regenauer-Lieb, “Free vibration analysis of a cracked shear deformable beam on a two-parameter elastic foundation using a lattice spring model,” *Journal of Sound and Vibration*, vol. 333, no. 11, pp. 2359–2377, 2014, ISSN: 0022-460X. DOI: https://doi.org/10.1016/j.jsv.2013.11.013. [Online]. Available: https://www.sciencedirect.com/science/article/pii/S0022460X13009267.

[37] F. van Keulen, *Advanced Mechanics Part: Continuum Mechanics*, Delft, 2018.

[38] Z. Friedman and J. B. Kosmatka, “An improved two-node timoshenko beam finite element,” *Computers & Structures*, vol. 47, no. 3, pp. 473–481, 1993, ISSN: 0045-7949. DOI: https://doi.org/10.1016/0045-7949(93)90243-7. [Online]. Available: https://www.sciencedirect.com/science/article/pii/0045794993902437.

[39] J. Reddy, “On the dynamic behaviour of the Timoshenko beam finite elements,” *Sadhana*, vol. 24, pp. 175–198, 1999, ISSN: 0256-2499.

[40] D. Caillerie, P. Kotronis, and R. Cybulski, “A Timoshenko finite element straight beam with internal degrees of freedom,” *International Journal for Numerical and Analytical Methods in Geomechanics*, vol. 39, no. 16, pp. 1753–1773, 2015, ISSN: 0363-9061.

[41] G. Kerschen, M. Peeters, J.-C. Golinval, and A. F. Vakakis, “Nonlinear normal modes, Part I: A useful framework for the structural dynamicist,” *Mechanical systems and signal processing*, vol. 23, no. 1, pp. 170–194, 2009, ISSN: 0888-3270.

[42] R. Rosenberg, “The Normal Modes of Nonlinear n-Degree-of-Freedom Systems,” *Journal of Applied Mechanics*, vol. 29, no. 1, pp. 7–14, 1962.

[43] R. M. Rosenberg, “On nonlinear vibrations of systems with many degrees of freedom,” *Advances in applied mechanics*, vol. 9, pp. 155–242, 1966, ISSN: 0065-2156.

[44] S. Shaw and C. Pierre, “Non-linear normal modes and invariant manifolds,” *Journal of sound and Vibration*, vol. 150, no. 1, pp. 170–173, 1991.

[45] S. W. Shaw and C. Pierre, “Normal Modes for Non-Linear Vibratory Systems,” *Journal of Sound and Vibration*, vol. 164, no. 1, pp. 85–124, 1993, ISSN: 0022-460X. DOI: https://doi.org/10.1006/jsvi.1993.1198. [Online]. Available: https://www.sciencedirect.com/science/article/pii/S0022460X83711983.

[46] W. Szemplinska, *The Behaviour of Nonlinear Vibrating Systems: Volume II: Advanced Concepts and Applications to Multi-Degree-of-Freedom Systems*. Springer Science & Business Media, 1990, vol. 12, ISBN: 0792303695.

[47] S. W. Shaw, “Invariant manifold representations of nonlinear modes of vibration,” *Modal Analysis of Nonlinear Mechanical Systems*, pp. 47–74, 2014, ISSN: 3709117909.

[48] O. V. Gendelman, “Nonlinear normal modes in damped forced systems,” *Modal Analysis of Nonlinear Mechanical Systems*, pp. 161–213, 2014, ISSN: 3709117909.

[49] C. Touzé, “Normal form theory and nonlinear normal modes: theoretical settings and applications,” *Modal analysis of nonlinear mechanical systems*, pp. 75–160, 2014, ISSN: 3709117909.

[50] M. Peeters, R. Viguié, G. Sérandour, G. Kerschen, and J. C. Golinval, “Nonlinear normal modes, Part II: Toward a practical computation using numerical continuation techniques,” *Mechanical Systems and Signal Processing*, vol. 23, no. 1, pp. 195–216, Jan. 2009, ISSN: 0888-3270. DOI: 10.1016/J.YMSSP.2008.04.003.

[51] M. Krack and J. Gross, *Harmonic balance for nonlinear vibration problems*. Springer, 2019, vol. 1.

[52] F. Schreyer and R. I. Leine, “A mixed shooting-harmonic balance method for unilaterally constrained mechanical systems,” *Archive of mechanical engineering*, vol. 63, no. 2, pp. 297–314, 2016, ISSN: 0004-0738.

[53] B. Cochelin, “Numerical computation of nonlinear normal modes using HBM and ANM,” *Modal Analysis of Nonlinear Mechanical Systems*, pp. 251–292, 2014, ISSN: 3709117909.

[54] M. Karimirad, C. Michailides, and A. Nematbakhsh, *Offshore mechanics: structural and fluid dynamics for recent applications*. John Wiley & Sons, 2018, ISBN: 1119216621.

[55] E. H. Moussi, S. Bellizzi, B. Cochelin, and I. Nistor, “Nonlinear normal modes of a two degrees-of-freedom piecewise linear system,” *Mechanical Systems and Signal Processing*, vol. 64-65, pp. 266–281, 2015, ISSN: 0888-3270. DOI: https://doi.org/10.1016/j.ymssp.2015.03.017. [Online]. Available: https://www.sciencedirect.com/science/article/pii/S0888327015001430.

[56] R. I. Leine and N. Van de Wouw, *Stability and convergence of mechanical systems with unilateral constraints*. Springer Science & Business Media, 2007, vol. 36, ISBN: 3540769757.

[57] G. Gilardi and I. Sharf, “Literature survey of contact dynamics modelling,” *Mechanism and Machine Theory*, vol. 37, no. 10, pp. 1213–1239, 2002, ISSN: 0094-114X. DOI: https://doi.org/10.1016/S0094-114X(02)00045-9. [Online]. Available: https://www.sciencedirect.com/science/article/pii/S0094114X02000459.

[58] B. Szabó and I. Babuška, “Finite Element Analysis: Method, Verification and Validation,” 2021, ISSN: 1119426421.

[59] R. De Borst, M. A. Crisfield, J. J. C. Remmers, and C. V. Verhoosel, *Nonlinear finite element analysis of solids and structures*. John Wiley & Sons, 2012, ISBN: 1118376013.

[60] M. Attar, A. Karrech, and K. Regenauer-Lieb, “Non-linear analysis of beam-like structures on unilateral foundations: A lattice spring model,” *International Journal of Solids and Structures*, vol. 88, pp. 192–214, 2016, ISSN: 0020-7683.

[61] W. Sheng *et al.*, “Hydrodynamic studies of floating structures: Comparison of wave-structure interaction modelling,” *Ocean Engineering*, vol. 249, p. 110 878, Apr. 2022, ISSN: 0029-8018. DOI: 10.1016/J.OCEANENG.2022.110878.

[62] A. Francescutto, T. Hirayama, B. S. H. Center, M. K. McCreight, S. Naito, and O. G. A. Rutgersson, “Seakeeping Committee Final Report and,” 1995.

[63] T. Sarpkaya, *Wave forces on offshore structures*. Cambridge university press, 2010, ISBN: 0521896258.

[64] A. I. Korotkin, *Added masses of ship structures*. Springer Science & Business Media, 2008, vol. 88, ISBN: 1402094329.

[65] J. M. J. Journée and W. W. Massie, “Offshore hydromechanics,” *Delft University of Technology*, 2001.

[66] J. Gerritsma, *Hydromechanica 4 - Scheepsbewegingen, sturen en manoeuvreren*, Delft.

[67] Y. Li, B. Xu, D. Zhang, X. Shen, and W. Zhang, “Numerical analysis of combined wave radiation and diffraction on a floating barge,” *Water*, vol. 12, no. 1, p. 205, 2020, ISSN: 2073-4441.

[68] J. N. Newman, *Marine hydrodynamics*. The MIT press, 2018, ISBN: 0262534827.

[69] H. de Koning Gans, *Introduction of Numerical Methods in Ship Hydromechanics*, Delft, Nov. 2012.

[70] N. Salvesen, E. O. Tuck, and O. Faltinsen, “Ship motions and sea loads,” 1970.

[71] S. Hirdaris, *Lecture 7 – Seakeeping methods*, Aalto, 2021.

[72] C.-C. Hsiung, “Comparison of the Strip Theory and the Panel method in computing ship motion with forward speed,” in *Technical University of Nova Scotia, Department of Mechanical Engineering, Halifax, Symposium on Selected Topics of Marine Hydrodynamics, National Research Council of Canada, St. John’s, Newfoundland*, 1991.

[73] G. N. Wells, “The Finite Element Method: An Introduction,” Tech. Rep., 2009, pp. 113–125.

[74] Z. Hamid, W. Mtalaa, J. Brunelot, and M. Potier-Ferry, “Asymptotic Numerical Method for strong nonlinearities,” *Revue Europeenne des Elements Finis*, vol. 2004, pp. 97–118, Apr. 2012. DOI: 10.3166/reef.13.97-118.

[75] M. Kwarta and M. S. Allen, “Nonlinear Normal Mode backbone estimation with near-resonant steady state inputs,” *Mechanical Systems and Signal Processing*, vol. 162, p. 108 046, 2022, ISSN: 0888-3270. DOI: https://doi.org/10.1016/j.ymssp.2021.108046. [Online]. Available: https://www.sciencedirect.com/science/article/pii/S0888327021004362.

[76] M. Hall and A. Goupee, “Validation of a lumped-mass mooring line model with DeepCwind semisubmersible model test data,” *Ocean Engineering*, vol. 104, pp. 590–603, 2015, ISSN: 0029-8018. DOI: https://doi.org/10.1016/j.oceaneng.2015.05.035. [Online]. Available: https://www.sciencedirect.com/science/article/pii/S0029801815002279.

[77] W. Wei, S. Fu, T. Moan, Z. Lu, and S. Deng, “A discrete-modules-based frequency domain hydroelasticity method for floating structures in inhomogeneous sea conditions,” *Journal of Fluids and Structures*, vol. 74, pp. 321–339, 2017, ISSN: 0889-9746. DOI: https://doi.org/10.1016/j.jfluidstructs.2017.06.002. [Online]. Available: https://www.sciencedirect.com/science/article/pii/S0889974616304856.

[78] X. Zhang, D. Lu, Y. Gao, and L. Chen, “A time domain discrete-module-beam-bending-based hydroelasticity method for the transient response of very large floating structures under unsteady external loads,” *Ocean Engineering*, vol. 164, pp. 332–349, 2018, ISSN: 0029-8018. DOI: https://doi.org/10.1016/j.oceaneng.2018.06.058. [Online]. Available: https://www.sciencedirect.com/science/article/pii/S0029801818311399.

[79] F.-K. Benra, H. J. Dohmen, J. Pei, S. Schuster, and B. Wan, “A Comparison of One-Way and Two-Way Coupling Methods for Numerical Analysis of Fluid-Structure Interactions,” *Journal of Applied Mathematics*, vol. 2011, E. Swim, Ed., p. 853 560, 2011, ISSN: 1110-757X. DOI: 10.1155/2011/853560. [Online]. Available: https://doi.org/10.1155/2011/853560.

[80] K. Heo, W. Koo, I.-K. Park, and J. Ryue, “Quadratic strip theory for high-order dynamic behavior of a large container ship with 3D flow effects,” *International Journal of Naval Architecture and Ocean Engineering*, vol. 8, Feb. 2016. DOI: 10.1016/j.ijnaoe.2015.11.001.

[81] D. S. Holloway, G. A. Thomas, and M. R. Davis, “Added mass of whipping modes for ships at high Froude number by a free surface boundary element method coupled with strip theory,” *ANZIAM Journal*, vol. 45, pp. C831–C844, 2003, ISSN: 1445-8810.

[82] K. H. Chua, D. Clelland, S. Huang, and A. Sworn, “Model experiments of hydrodynamic forces on heave plates,” in *International Conference on Offshore Mechanics and Arctic Engineering*, vol. 41952, 2005, pp. 943–948, ISBN: 0791841952.

[83] J. K. Sharma, “Theoretical and experimental modal analysis of beam,” in *Engineering Vibration, Communication and Information Processing: ICoEVCI 2018, India*, Springer, 2019, pp. 177–186, ISBN: 9811316414.

[84] Z. R. Lu, M. Huang, J. K. Liu, W. H. Chen, and W. Y. Liao, “Vibration analysis of multiple-stepped beams with the composite element model,” *Journal of Sound and Vibration*, vol. 322, no. 4, pp. 1070–1080, 2009, ISSN: 0022-460X. DOI: https://doi.org/10.1016/j.jsv.2008.11.041. [Online]. Available: https://www.sciencedirect.com/science/article/pii/S0022460X08009462.

[85] G. Y. Wang and G. T. Zheng, “Vibration of two beams connected by nonlinear isolators: analytical and experimental study,” *Nonlinear Dynamics*, vol. 62, pp. 507–519, 2010, ISSN: 0924-090X.

A

Example energy dependance non linear normal modes

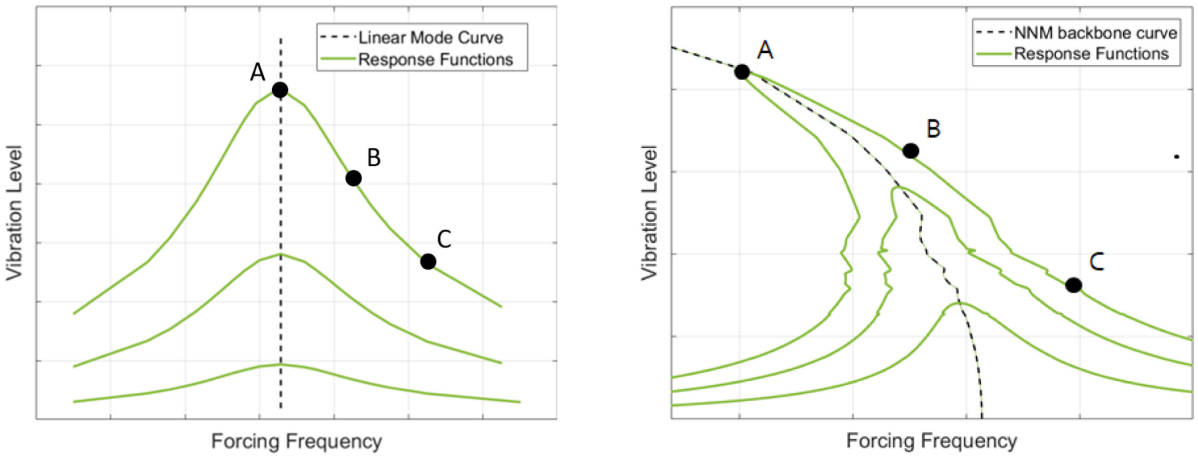

(a) (b)

Figure A.1: Example energy dependance non linear normal modes [75]

B

Modal interactions and mode bifurcations

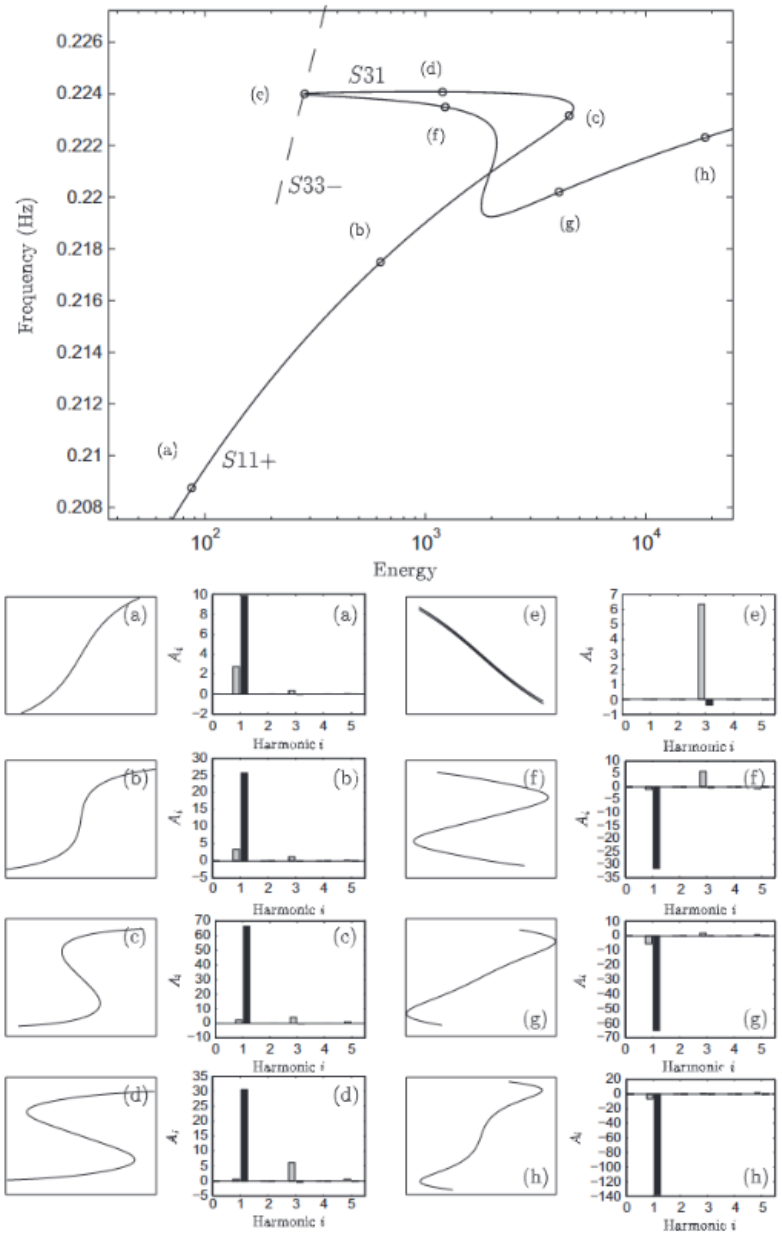

Figure B.1: Example of internal resonance in non linear normal mode systems [41]

C

Shooting procedure example

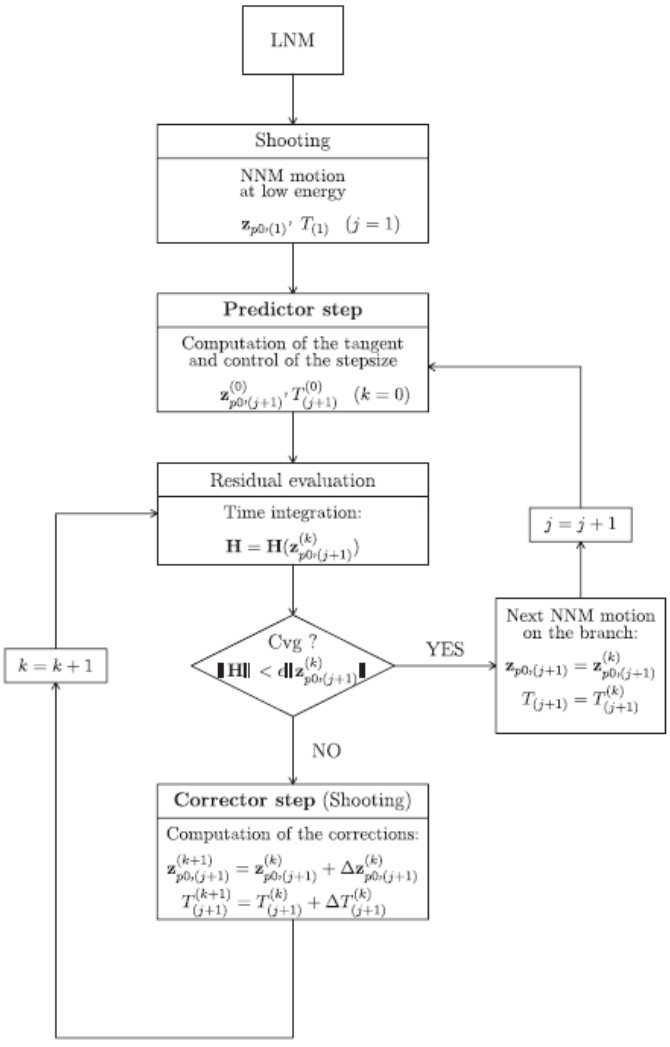

Figure C.1: Non-linear Normal Mode numerical procedure. As a starting point the Linear Normal Mode (LNM) solution $\boldsymbol{z_{P0,(1)}}$ with corresponding period $T_{(1)}$ is solved in the first step. Next up, the residual is evaluated, which is then checked for convergence. If not, the Newton-Raphson method is used to correct the initial guess for $\boldsymbol{z_{p0}}$ and T_j. This step is repeated until convergence. After that, the next non-linear normal mode is defined using the last defined $\boldsymbol{z_{p0}}$ and T_j. [50]

D

Algorithm mixed shooting-harmonic balance method

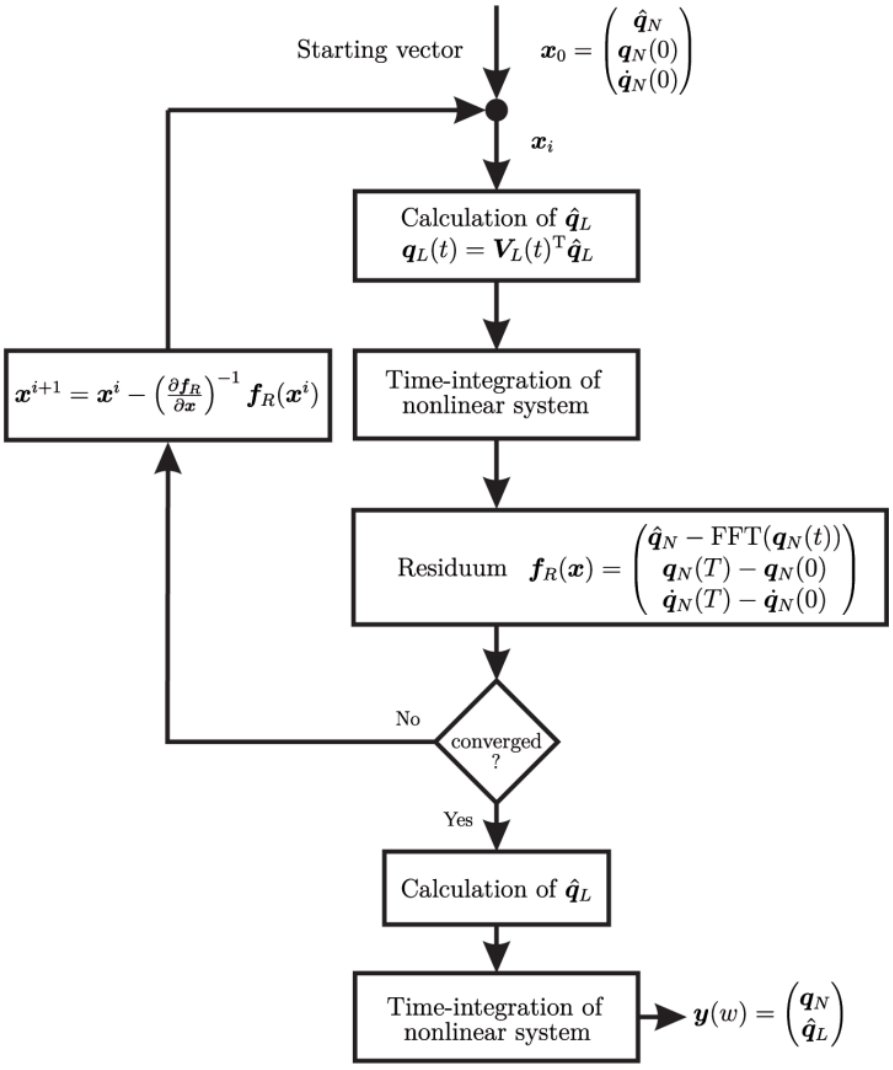

Figure D.1: Algorithm mixed shooting-harmonic balance method [52]

E

Additional research related to two-way coupling

This appendix provides additional research which is performed in relation to the initial two-way coupled model. Figure E.1 shows a simplified graphical representation of the initial approach of the model. Figure E.1a shows that now both the ship and the cargo are discretized using the finite element method. The excitation is provided by the wave pressures, depending on the position on the vessel and time, and is represented by $p(x,t)$.

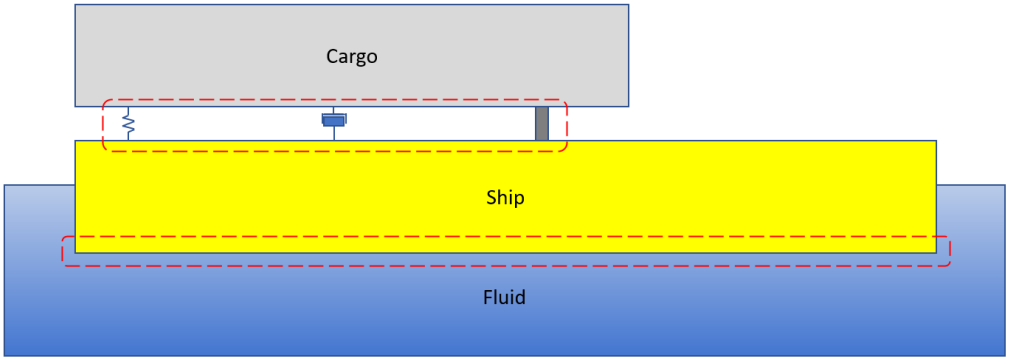

(a) Distinguished models and interfaces. The stiffness is modeled as a spring as shown on the left, the damping factors as a damper which is shown in the middle and a rigid connection is shown on the right. These elements emphasize the variability in elements required to model a sea-fastening system.

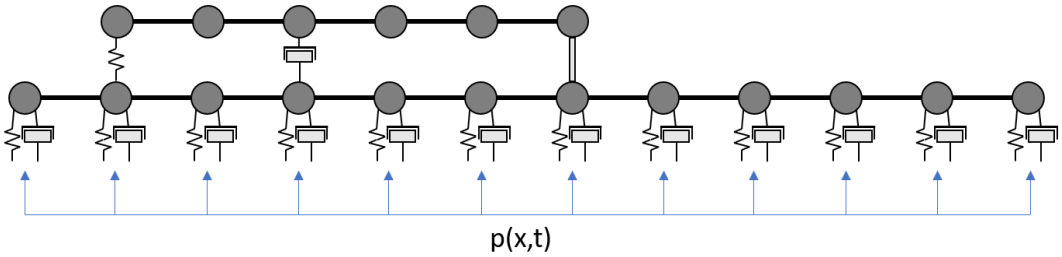

(b) Discretization of ship-cargo-fluid system using the finite element method. The boundary conditions between the ship and the cargo are the same as defined in figure 2.1.

Figure E.1: The figure shown in (a) shows identified models and interfaces, while the figure shown in (b) shows the created model based on these models and interfaces.

The main part which changes in this approach is the fundamental finite element equation used to define the structrural and dynamic response of the system, as shown in equation E.1. The hydrodynamic contributions, being the added mass matrix **A**, hydrodynamic damping **B** and hydrostatic stiffness **C**, are added to the defined structural matrices **M**, **D** and **K**. the hydrostatic stiffness and hydrodynamic damping are represented by springs and dampers in figure E.1b, note that these are only applied on the discretized elements for the vessel. A frequency domain formulation is again used, based on a harmonic response assumption. At last, the system is excited by a wave force $\mathbf{F_w}$.

$$\begin{aligned} \mathbf{x} &= \mathbf{u} \cdot e^{-i\omega t} \\ \left(-\omega^2 \left[\mathbf{M} + \mathbf{A}\right] + i\omega \left[\mathbf{D} + \mathbf{B}\right] + \left[\mathbf{K} + \mathbf{C}\right]\right) \mathbf{u} &= \mathbf{F}_w \end{aligned} \tag{E.1}$$

These figures and this equation summarize the approach to obtain a model where two-way coupling between the ship and cargo, taking hydrodynamic contributions into account. This appendix describes the approach based on the following. At first, paragraph E.1 describes some additional literature related to connecting the hydrodynamic contributions to the structural model. After that, paragraph E.2 presents the identified implementation method based on the literature. This then concludes the additional information required to model the two way coupling, so paragraph E.3 continues on this for a case which is attempted to be modeled. Finally, paragraph E.4 discusses the difficulties encountered when modeling the problem, and provides some identified problems. Note that no theory related to the structural model is presented here, this is all governed in chapter 5.

E.1. Additional literature two-way coupling

In literature, some examples can be found how the hydrodynamic properties can be coupled to the structural model. In [76] a submerged cable is discretized using a lumped mass model, which is validated in this study. Here, the hydrodynamic properties are linked to the nodes. The added mass is added at the node locations, while damping is modeled as drag force, given by Morison's equation.

Furthermore, in different discrete hydro-elastic analysis, the hydrodynamic properties are distributed over nodes as well [6, 77, 78]. The added mass is added to the nodal mass, and the hydrodynamic damping is defined per segment, and applied per node as well. Furthermore, Wei et al. mention in their paper that the hydrodynamic damping is significantly larger than the structural damping [77]. More research should be performed to determine whether this is the case for the considered problem. Figure E.2 shows the wave force components acting on a certain node.

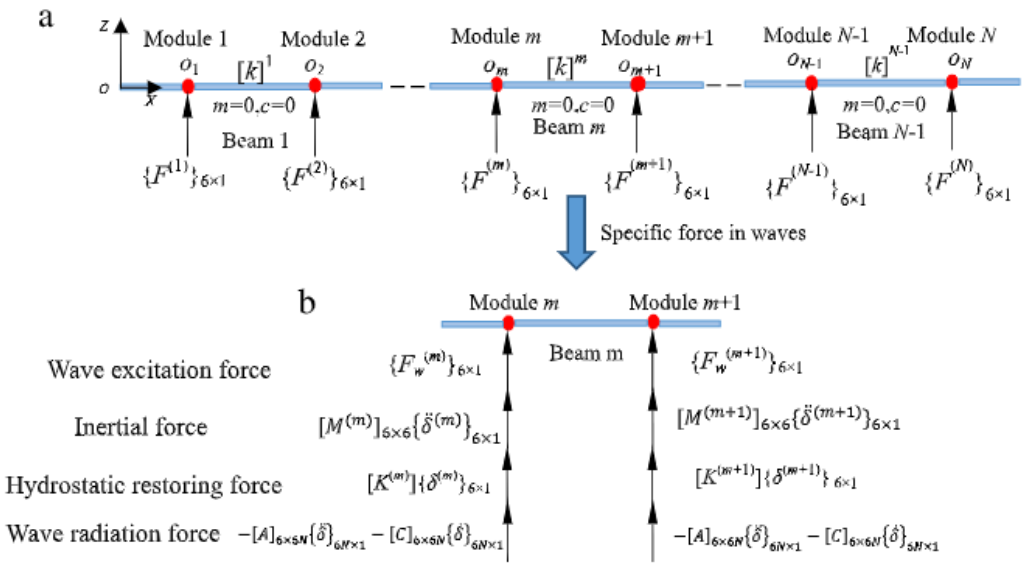

Figure E.2: Hydrodynamic forces acting on nodes in discretized model [77]

In this study equation 2.14 is transferred into frequency-domain, as shown in equation E.2. In this equation parameter ω is defined as the excitation frequency by the waves. The assumption is made that if the excitation force is harmonic, the response will be harmonic as well.

$$\begin{aligned} \mathbf{x} &= \mathbf{u} \cdot e^{-i\omega t} \\ \left(-\omega^2 \left[\mathbf{M} + \mathbf{A}\right] + i\omega \left[\mathbf{B} + \mathbf{D}\right] + \left[\mathbf{C} + \mathbf{K}\right]\right) \mathbf{u} &= \mathbf{F}_w \end{aligned} \tag{E.2}$$

Note that the implementation of the wave excitation force $\mathbf{F_W}$ defines a hydro-elastic formulation or not. In case of hydrodynamic two-way coupling, this excitation force is a function of the structural displacement. When considering a one-way coupling, this displacement is neglected. From a numerical efficiency point of view this simplification is preferred, since it results in fewer complicated calculations [79]. In figure E.3 a figure is shown that represents the different models and discretizations applied. Note that to solve for the hydrodynamic part, so for the hydrodynamic forces only a one-way coupling between the fluid and structural model is assumed. After applying the hydrodynamic properties onto the finite element formulation of the ship, there will be a two-way coupling present in the structural part of the model, between the cargo and the vessel.

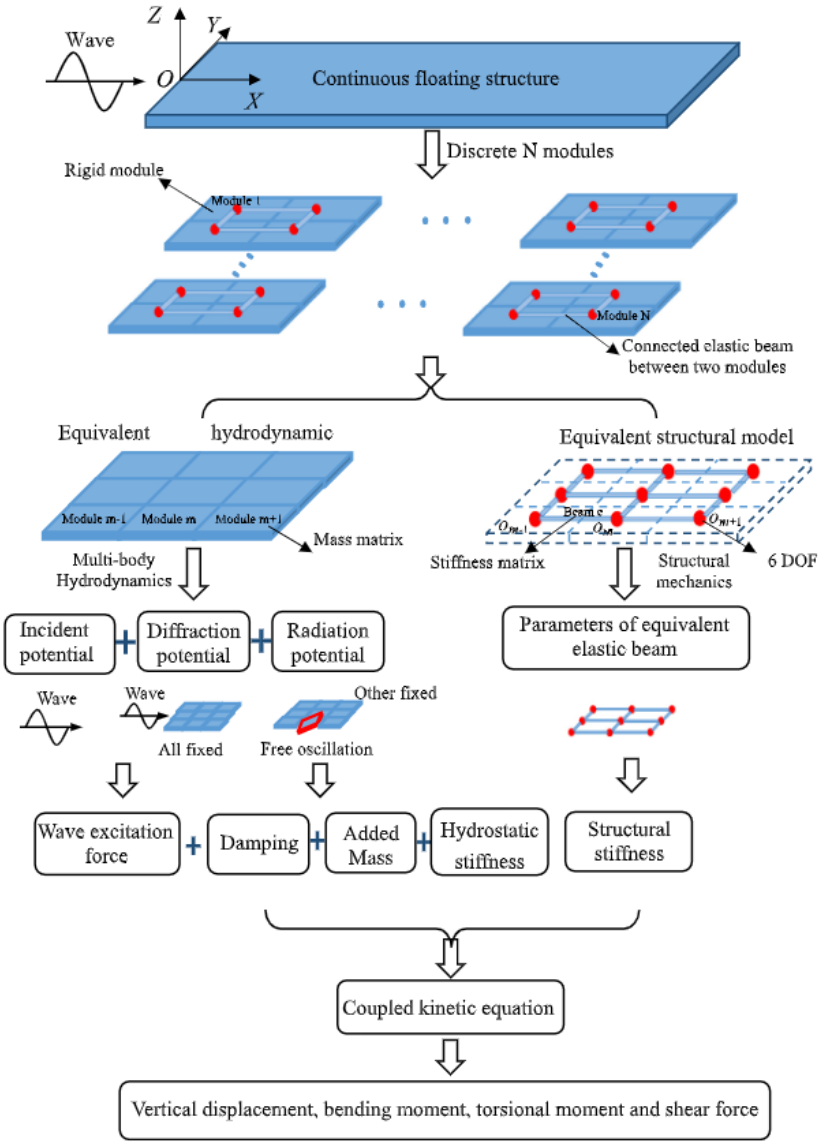

Figure E.3: Different models distinguished in structural and hydrodynamic analysis [77]

E.2. Implementation of hydrodynamic model

Via BigLift hydrodynamic data is obtained for the MC-class vessel. This consists of the added mass, damping and hydrostatic stiffness matrices, based on the wave frequency. This paragraph discusses the connection between the hydrodynamic and structural side of the model.

In order to connect the hydrodynamic and structural model one major difference between the two is identified. Figure E.4 shows the defined degrees of freedom for a ship, considered in diffraction analysis. This implies that the matrices and forces found in the analysis are defined for a vessel in a global coordinate system. The structural model can be defined as a local model, taking into account the deflections of the vessel. Therefore, this section further clarifies how the data obtained for the global vessel motions is transformed into data used by the structural model.

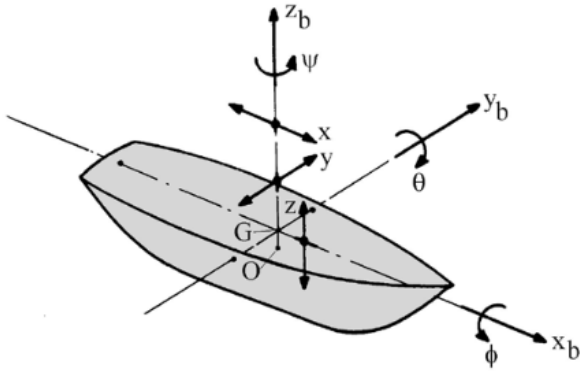

Figure E.4: Definition ship motions in six degrees of freedom [65]

Furthermore, another important difference is that the structural model is defined for a 2-dimensional situation. Therefore, only contributions and behavior relevant for surge, heave and pitch motion is considered in this analysis.

E.2.1. Distribution added mass, damping and hydrostatic stiffness

Added mass

In equation E.3 some definitions of the added mass in the heave and pitch directions are shown. In this equation $a_{33}(x)$ is defined as the added mass distribution, x the length variable over the vessel and L the total length of the vessel. This implies that the heave and pitch added mass, and the coupling terms, are only dependent on the heave added mass distribution. Therefore, an analysis is made how this distribution can be defined, since this part could be connected to the structural model. Furthermore, note that the definition for the damping terms is analogous to the added mass shown in equation E.3.

$$\begin{aligned} A_{33} &= \int_{-L/2}^{L/2} a_{33}(x)dx \\ A_{35} = A_{53} &= -\int_{-L/2}^{L/2} x\ a_{33}(x)dx \\ A_{55} &= \int_{-L/2}^{L/2} x^2\ a_{33}(x)dx \end{aligned} \tag{E.3}$$

Figure E.5 shows the heave added mass distribution for a half-cylinder, placed longitudinally in the water. In this case, 2D and 3D represent different analysis methods to obtain the added mass distribution. In this case, only the 3D distribution is considered. What this figure shows is that the heave added mass distribution is maximum in the middle of a uniform object and lowest at the sides. Intuitively, this is correct, since the added mass is constrained the most in the middle of the vessel.

A difference between this uniform half-cylinder and ships is the symmetry in the yz-plane. Since vessels are generally not symmetrical in this plane, it causes asymmetry in the heave added mass distribution. This asymmetry will result in heave-pitch coupling, so the A_{35} and A_{53} terms are nonzero. Both these values are known for the MC-class vessels and will be used in the definition of the added mass distribution.

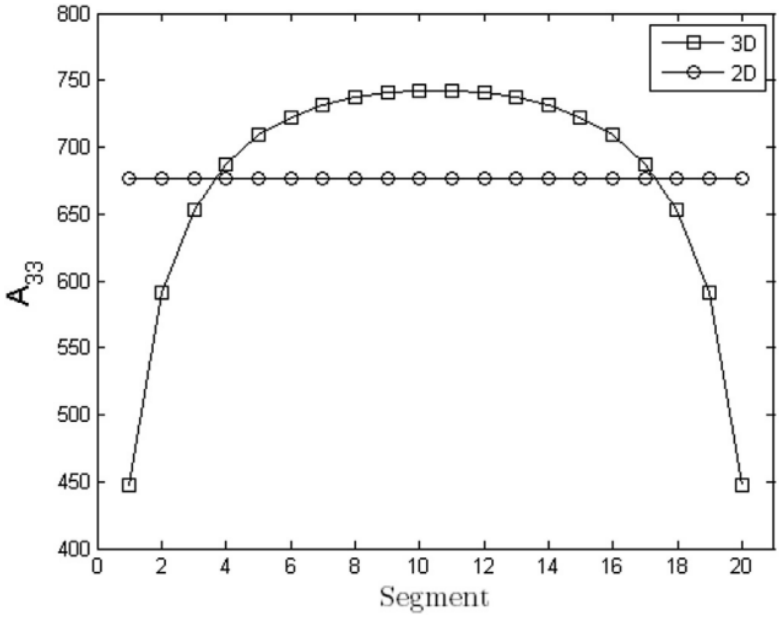

Figure E.5: Heave added mass distribution with different approximation methods [80]

Figure E.6 shows another heave added mass distribution, for a 100 meter long catamaran [81]. It can be seen that this distribution is more flat compared to the one shown figure E.5. This flattening is expected to be caused by a non-uniform shape, since the water around the front and aft end of the hull is less constrained.

In this paper, they compared different approximation methods of the added mass distribution with their influence on the first natural frequency [81]. What is observed in this paper is that the distribution only slightly does influence the natural frequency. Although this conclusion is convenient and allows for simple implementation, it is tried to find an accurate distribution over the length. It is expected that the local added mass contributions do have an effect on the deflections of the vessel.

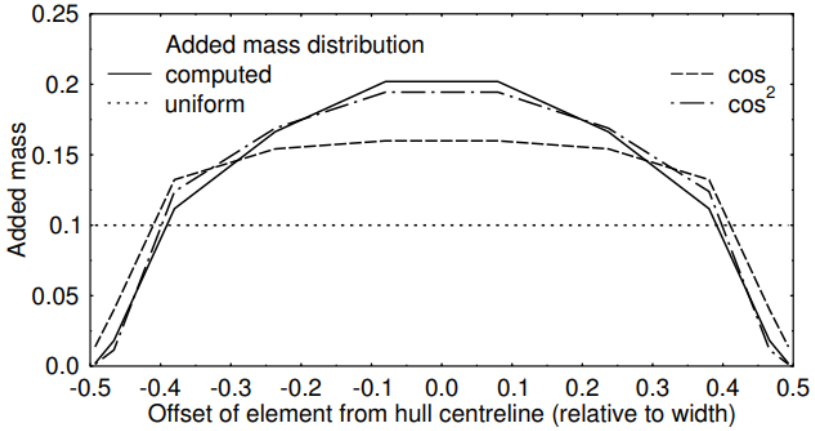

Figure E.6: Heave added mass distribution based on different analysis methods [81]

In order to find an accurate added mass and damping distribution for the MC-class vessels some curve fitting is applied. The distribution function needs to comply with the following conditions:

1. The values A_{33}, A_{35} and A_{55} are known, so equation E.3 needs to hold.
2. Based on figure E.5 and E.6 the added mass along the main frame needs to be more or less uniform
3. At the front and aft end of the ship the added mass needs to be 0.
4. All values must be positive.

The most important step in curve fitting is selecting a mathematical expression for which the fit will be performed. A statistical distribution is chosen as base function for the fit. There are 2 main properties that the function needs to have, being that the skewness and kurtosis of the distribution is dependent on the input parameters. After some research, no function was found where skewness and kurtosis could be independently influenced by separate parameters. Therefore, the generalized normal distribution is chosen as a base function, since here kurtosis can be controlled by the parameter β. The generalized normal distribution is shown in equation E.4. Based on this equation, a curve fit could be made for the added mass based on the values A_{33} and A_{55}. Note that the function is implemented in a different manner, represented by $a(x)$ in figure E.7. Within this figure, parameter b is varied between 0.5 to 0.8, showing different levels of kurtosis. Furthermore, the implementation of $a(x)$ in this manner ensures that the integral can have the value of A_{33} instead of being 1.

$$p(x) = \frac{\beta}{2\alpha\Gamma(1/\beta)} e^{-(|x-\mu|/\alpha)^{\beta}} \tag{E.4}$$

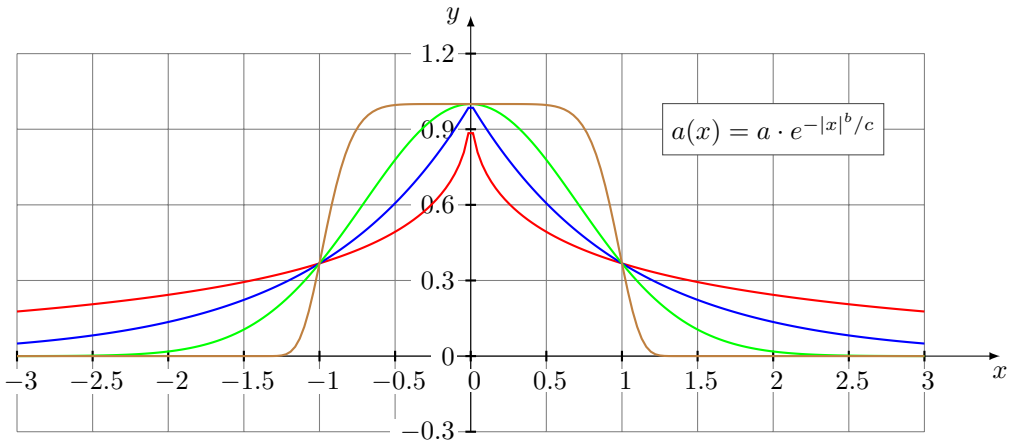

Figure E.7: Force deflection curves for different saddle formulations

To be able to include the requirement based on A_{35} value as well, a method needs to be found to include asymmetry in the function as well. Figure E.8 shows the equation chosen to include skewness. This function has a value of 1, except for the locations $+e$ and $-e$. Furthermore, the steepness of this function is defined by parameter d. In this manner, asymmetry can be created within the function. The function shown in figure E.8 is multiplied by E.4, and this is then put into a solver. Please note that the result is not unique, multiple solutions are possible.

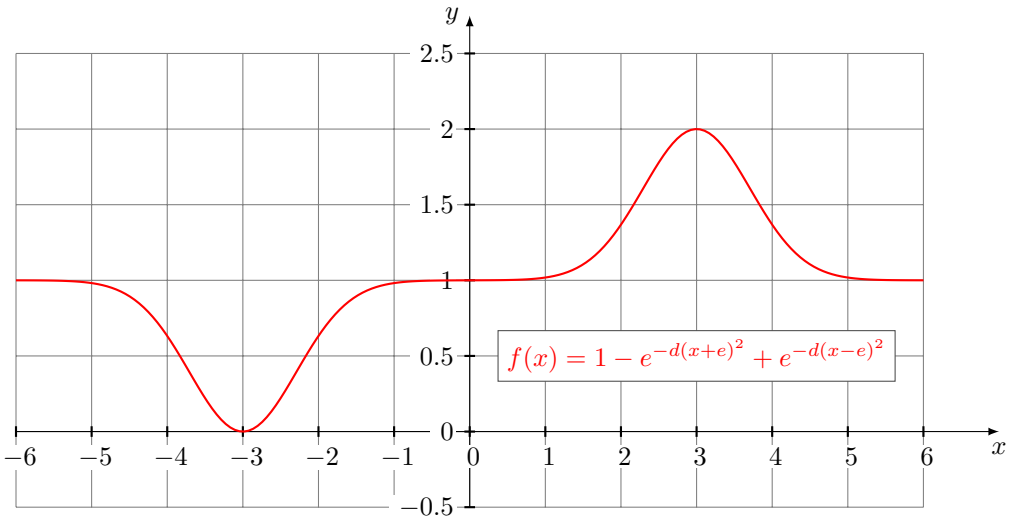

Figure E.8: Force deflection curves for different saddle formulations

Table E.1 shows the coefficients of the curve-fitted curve. The resulting added mass distribution is shown in figure E.9. Compared to Figures E.5 and E.6, the results are reasonable. The large drops at the front and aft end of the ship are expected, due to 3D effects and the change in hull shape. Note that the condition regarding the distribution being 0 at the front and aft end is relaxed, since a distribution cannot be equal to 0.

Table E.1: Results curve fitting

Coefficient	Value
a	1973.7
b	3.33
c	51.2
d	0.0013
e	75

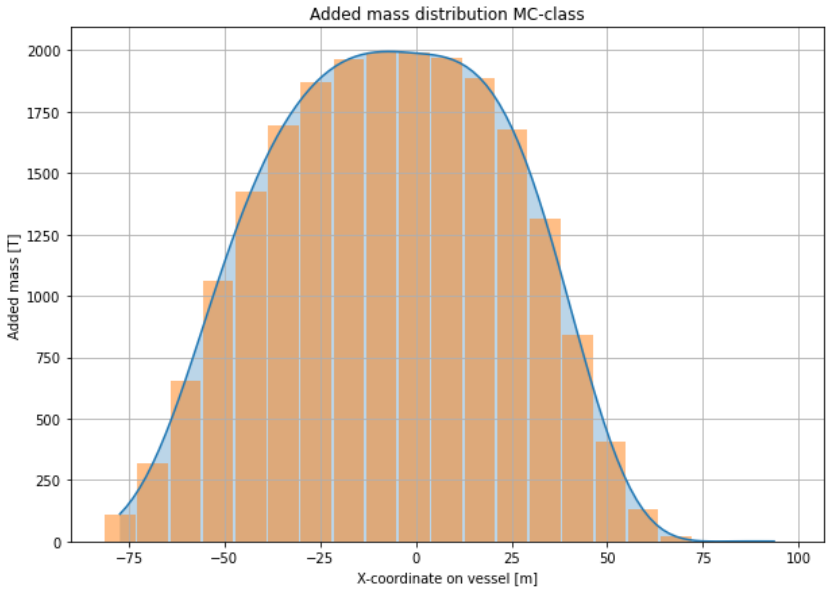

Figure E.9: Heave added mass distribution for MC-class vessels based on curve fitting

The orange bars in figure E.9 shows the distribution of the curve over 21 nodes. The area represented by these orange bars is equal to the added mass which is applied to each structural node in the finite element formulation. For the surge direction a similar type of analysis can be made. After some inspection of the total surge added mass value A_{11} it became clear that this value is approximately 150 times smaller than the heave value. Therefore, the choice has been made to neglect it since its value is limited and the analysis required is extensive.

Hydrodynamic damping

For the hydrodynamic damping the same analysis can be made, since B_{33}, B_{35} and B_{55} are known. After some analysis it became clear that the damping is of less importance with regard to the obtained numerical results. For closed cross sections the inertial forces dominate over the damping forces, as shown in the experimental study of K.H. Chua [82]. In this paper they showed that damping forces do become significant for open cross sections. For closed cross sections the damping only influences the phase of the hydrodynamic forces.

On the basis of experience regarding the structural model the choice is made to still include the damping. It is observed that the structural model has trouble with convergence close to eigenfrequencies, since the response tends to infinity if no damping is included. Therefore, the same algorithm as mentioned for the added mass will be applied. Table E.2 shows the coefficients obtained for the fitting of the hydrodynamic damping, with the resulting curve shown in figure E.10.

Table E.2: Results curve fitting hydrodynamic damping

Coefficient	Value
a	38.0
b	2.96
c	34.6
d	0.0002
e	58.4

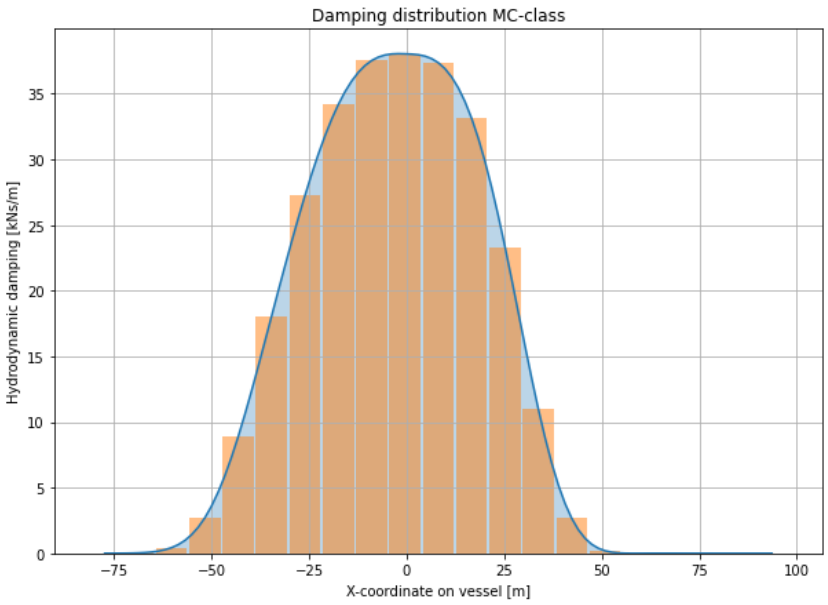

Figure E.10: Hydrodynamic damping distribution for MC-class vessels based on curve fitting

Hydrostatic restoring stiffness

The hydrostatic restoration stiffness depends on the area of the ship. It is known that the hydrostatic stiffness is much smaller than the structural stiffness, but this will still be included in the system. During

the previous analysis, it became clear that for some situations the model would converge to situations where a free-free beam would rotate, since no rotation constraint was applied. Therefore, the same procedure is repeated for the hydrostatic stiffness distribution. The results of the curve fitting procedure are shown in table E.3 and figure E.11.

Table E.3: Results curve fitting hydrodynamic damping

Coefficient	Value
a	417.3
b	4.97
c	80.4
d	0.0011
e	98.0

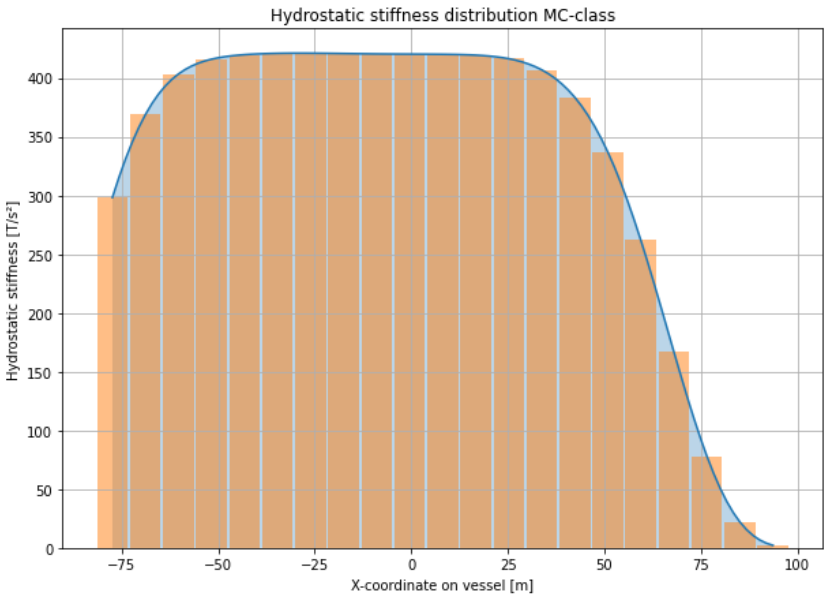

Figure E.11: Hydrostatic stiffness distribution for MC-class vessels based on curve fitting

Hydrodynamic load distribution

The last step in modeling the loadcase is finding a distribution for the applied force. This distribution depends on the pressure and waterline area distribution of the vessel. An example of this pressure distribution is shown in figure E.12.

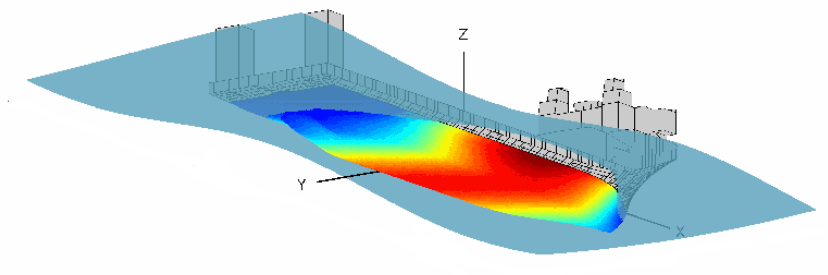

Figure E.12: Hydrodynamic pressure distribution for example ship

Furthermore, these forces are calculated in diffraction software using equation E.5. These forces and moments are all derived from the pressure distribution p, which follows from potential theory. Equation

E.5 shows the definition of the pressure based on the undisturbed wave potential Φ Note that the pressure distribution p is a function of the wave amplitude ζ_a, wave frequency ω and water depth z. Since only access has been obtained for the results of the diffraction analysis, some simplifications need to be made.

$$\begin{aligned} \mathbf{F} &= -\iint_S (p \cdot \mathbf{n}) dS \\ \mathbf{M} &= -\iint_S p \cdot (\mathbf{r} \times \mathbf{n}) dS \\ p &= -\rho \frac{\partial \Phi}{\partial t} - \rho g z \\ \Phi(x, y, z, t) &= \frac{\zeta_a g}{\omega} \cdot e^{kz} \cdot \sin(kx \cos \mu + ky \sin \mu - \omega t) \end{aligned} \tag{E.5}$$

The information that follows from the diffraction analysis is the total force amplitude F_a and phase between the force and wave elevation $\epsilon_{F,\zeta}$ for a given wave exciting frequency ω, as shown in equation E.6. Here, a key assumption is that for a harmonic excitation ω, the response will be harmonic with frequency ω as well.

$$\begin{aligned} F_3(t) &= F_{3,a} \cos(\omega t + \epsilon_{F3,\zeta}) \\ F_5(t) &= F_{5,a} \cos(\omega t + \epsilon_{F5,\zeta}) \end{aligned} \tag{E.6}$$

Based on this background an analysis will be made to find an approximation for the pressure distribution over the vessel. Note that this analysis is again performed for the 2D situation, so only taking surge, heave and pitch into account. Some conditions are posed on this pressure distribution, formulated as follows:

1. The pressure distribution must be a function of the wave elevation along the ship and be of the same shape.
2. The resulting pressure distribution multiplied by the location dependent waterline area A_{wl} needs to be equal to the force amplitude F_3, at the moment in time where maximum heave force is excerted on the vessel.

The implementation of the first step is shown in figure E.13. Note that the magnitude of this pressure is not known a priori. The step shown here assumes only that the shape of the pressure corresponds to the shape of the wave elevation. Furthermore, any phase difference between the wave elevation and pressure distribution is neglected, since it is not relevant for the loadcase.

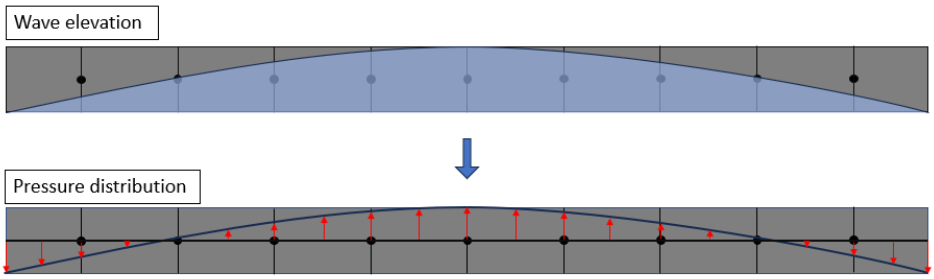

Figure E.13: Hydrodynamic pressure distribution for certain wave elevation

Equation E.7 shows the mathematical formulation of the wave elevation and the derived pressure formulation. To obtain the pressures over the length, a certain phase change needs to be accounted for. This phase change is defined by the term kx, with k being the wave number and x the location on the vessel. Furthermore, the term e^{kz_x} follows from the undisturbed wave potential, and takes the influence of submersion into account. Parameter z_x is defined as the mean draft at a certain longitudinal location.

$$\begin{aligned} \zeta(x,t) &= \zeta_a \cos(\omega t + kx) \\ p(x,t) &= p_a e^{kz_x} \cos(\omega t + kx) \end{aligned} \tag{E.7}$$

The wave number k can be obtained using the dispersion relation with the deep water assumption, shown equation E.8. This enables creating a pressure distribution of over the length of the vessel.

$$k = \frac{\omega^2}{g} \tag{E.8}$$

From there, this distribution form can be multiplied by the waterline area distribution. This distribution of the waterline area is shown in figure E.14, together with the distribution of the draft over the length. The waterline area can be discretized for a specified number of nodes. At this location a certain average draft can be obtained as well, which is then used in the pressure formulation. The average draft shown around the value of $x = 60\ m$ is to take the bow flare into account.

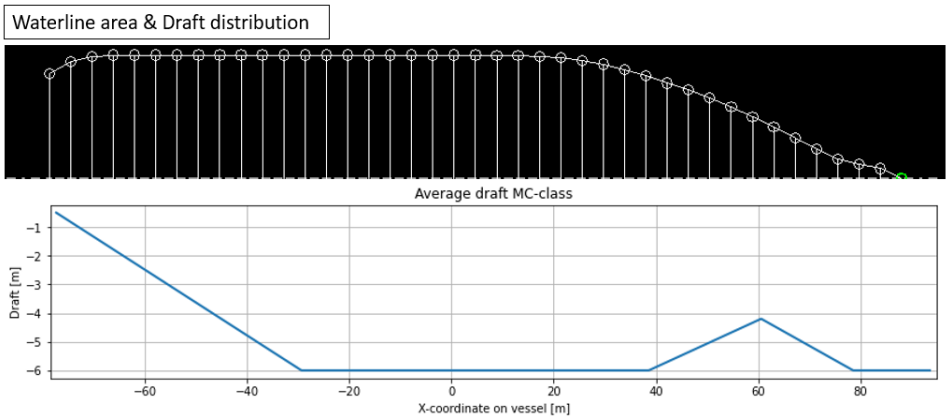

Figure E.14: Waterplane area and draft distribution for MC-class vessels

By multiplying the area by the pressure, a force per node is obtained. Figure E.15 shows this force per node, with a clear longitudinal location and area dependency. The sum of all these forces should be equal to the resulting force amplitude value $F_{3,a}$ from the diffraction analysis, specified for a certain wave height ζ_a and frequency ω.

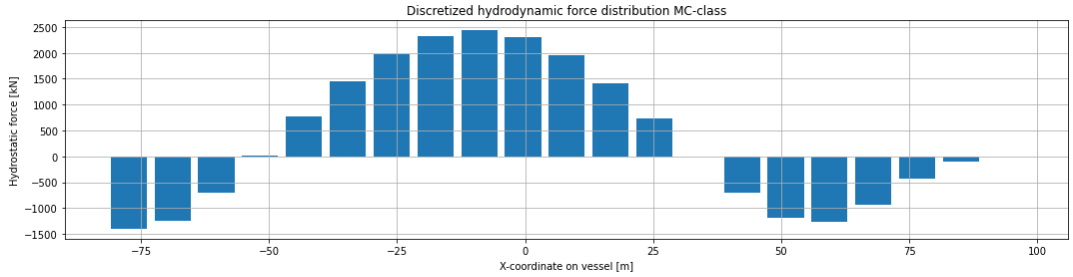

Figure E.15: Discretized hydrodynamic force for MC-class vessels

At last, the moment in time needs to be identified at which the maximum heave force is exerted on the vessel. Figure E.16 shows the hydrodynamic force distribution for two different instances in time. For the left figure a large upward heave force is observed, while the resulting force for the right figure will be approximately zero. Therefore, the conclusion is drawn that the moment in time when the maximum heave force is exerted must be equal to the amplitude $F_{3,a}$.

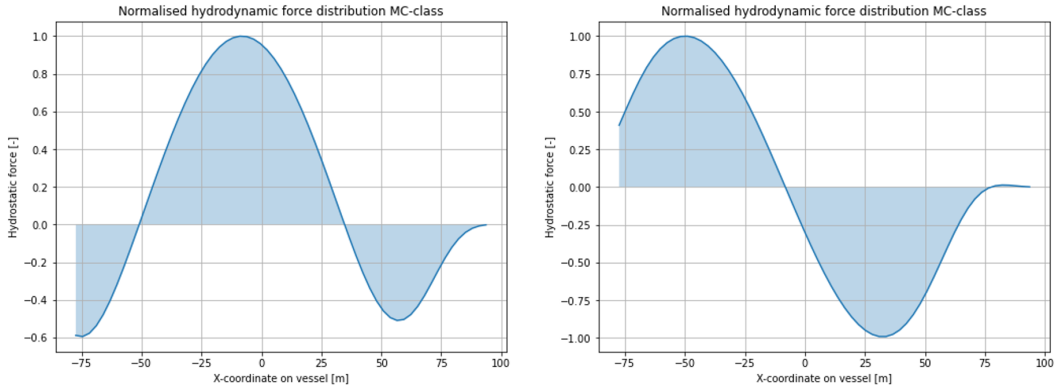

Figure E.16: Effect of phase on hydrodynamic force contribution

Important to understand here that the moment in time with the largest resulting heave force requires the smallest amplitude of the hydrodynamic force distribution to do so. This implies that a minimization problem can be identified. Equation E.9 shows the first step in the derivation of the objective function. This is based on the force equilibrium in heave direction, the summation of all local forces acting on the nodes need to be equal to heave force amplitude. Parameter $p(x_i, t)$ represents the pressure acting at a certain location x_i, with A_{x_i} being the waterplane area that this certain node governs. Furthermore, the earlier identified force and pressure formulation, shown in E.6 and E.7 respectively, are substituted in this equation. The phase $\epsilon_{F3,\zeta}$ is set to 0 as mentioned earlier, since it is not relevant to the magnitude of the load case.

$$\begin{aligned} \sum p(x_i, t) A_{x_i} &= F_3(t) \\ \sum p_a e^{kz_x} \cos(\omega t + kx_i) A_{x_i} &= F_{3,a} \cos\left(\omega t + \epsilon_{F3,\zeta}\right) \end{aligned} \tag{E.9}$$

Equation E.10 rewrites the phase change, drops out the time dependent part and solves for the pressure amplitude p_a. In this equation ϵ_{x_i} represents the phase due to the longitudinal position relative to the center of buoyancy of a certain node. Finally, an artificial phase change ϵ is introduced to account for the behavior discussed earlier, shown in figure E.16.

$$\begin{aligned} \epsilon_{x_i} &= kx_i \\ p_a(\epsilon) &= \frac{F_{3,a}}{\sum A_{x_i} e^{kz_x} \cos(\epsilon_{x_i} + \epsilon)} \end{aligned} \tag{E.10}$$

The result of equation E.10 is transformed into a minimization problem, using the pressure amplitude function as objective function. This minimization problem is defined as follows.

$$\begin{aligned} \min_x \quad & f(x) = \frac{F_{3,a}}{\sum (A_{x_i} e^{kz_x} \cos(\epsilon_{x_i} + x))} \\ \text{Subject to:} \quad & -\pi < x < \pi \\ & 0 < f(x) \end{aligned}$$

The result of this minimization problem $f(x)$ is equal to the pressure amplitude p_a, with x being the phase where this amplitude occurs. With the pressure amplitude being known, the force distributed for every node can be computed using equation E.11.

$$F_{a,x_i} = p_{a,x_i} A_{x_i} \tag{E.11}$$

Figure E.17 shows the hydrodynamic force distribution for 0.12, 0.6 and 1.2 rad/s. For the longest wave with a frequency of 0.2 rad/s the left figure clearly shows a hydrostatic dominant force distribution, in

line with the expected behavior. For the shortest wave of with a frequency of 1.2 rad/s, shown in the most right figure, the pressure change over draft is observed in the aft of the vessel.

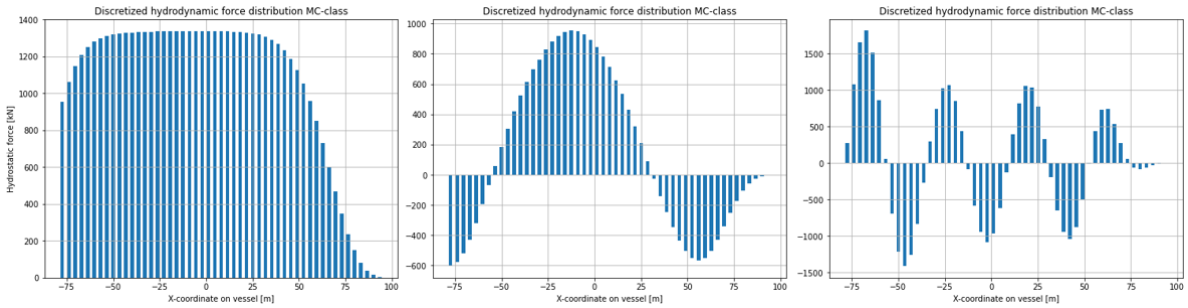

Figure E.17: Hydrodynamic force distribution for 0.12, 0.6 and 1.2 rad/s, shown in the left, middle and right figure respectively

Table E.4 shows some excitation frequencies ω with the obtained pressure amplitude p_a. The results can be verified to some extent, since information regarding the pitch moment is present as well. Another solver is used to identify the maximum bending pitch moment, and these are compared to the results in the table. This table shows that the results seem reasonable for 0.12 and 1.2 rad/s, but a large deviation is observed for 0.6 rad/s. It is expected that small differences in the waterplane area definition result in large differences here.

Table E.4: Verification results hydrodynamic force distribution

Frequency ω [rad/s]	**Averaged pressure amplitude p_a [kPa]**	**Pitch moment $F_{5,a}$ [kNm]**	**Pitch moment diff. $F_{5,a}$ [kNm]**	**Difference [%]**
0.12	9.44	3.17e5	3.289e5	3.6
0.6	6.71	11e5	7.81e5	30
1.12	8.0	2.6e5	2.78e5	6.5

E.2.2. Verification hydrodynamic model

In this section the implementation of the hydrodynamic model is verified, using data known for this particular loadcase. This data consist of the rigid body motions, and the response amplitude operators. If the identified hydrodynamic loadcase is applied on the vessel, the rigid body motions should result from the structural model. Table E.5 shows the main particulars of the verification loadcase. Note that the draft defines the values of the hydrodynamic matrices. The weight and rotary inertia of the vessel and cargo define the rigid body motions.

Table E.5: Identified parameters verification case

Parameter	**Value**	**Unit**
T	6	m
Δ	30365	T
I_{yy}	6.98e7	Tm^2

Verification hydrostatic stiffness

To verify the methodology chosen to distribute the mass, damping and hydrostatic stiffness some data of the waterline is obtained. Figure E.18 shows the comparison of the data and the approximation method. In general, it is observed that the shape of the approximation shows good accordance with the data.

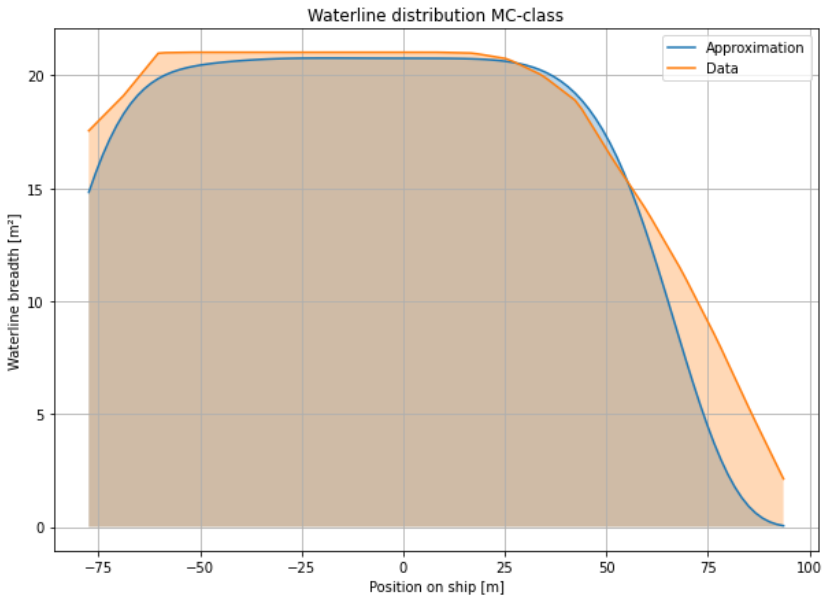

Figure E.18: Waterplane area distribution comparison

Table E.6 shows a comparison between the resulting hydrostatic stiffness. Here it is observed that the waterline data overestimates the actual hydrostatic stiffness value retrieved from the C matrix. In later stages it became clear that this overestimation influences the observed rigid body motions. Therefore, the choice is made to continue with the approximated waterplane area.

Table E.6: Comparison hydrostatic stiffness

Parameter	Value [T/m^2]
C_{33} Data	57675
C_{33} Approx.	61000
C_{33} Actual	57700

Furthermore, during the implementation of the loadcase some other important aspects related to the hydrostatic stiffness is observed. In order to model the rigid body motions, the rigid body modes in heave and pitch direction need to be used from the structural model. Figure E.19 shows the rigid body modes for different center of gravity values. Here the observation is made that the center of gravity of the model needs to be directly above the center of flotation in order to not cause any rotation, as shown in the left figure. For the right figure an offset is present between the COG and COF, causing a rotation in the rigid body mode.

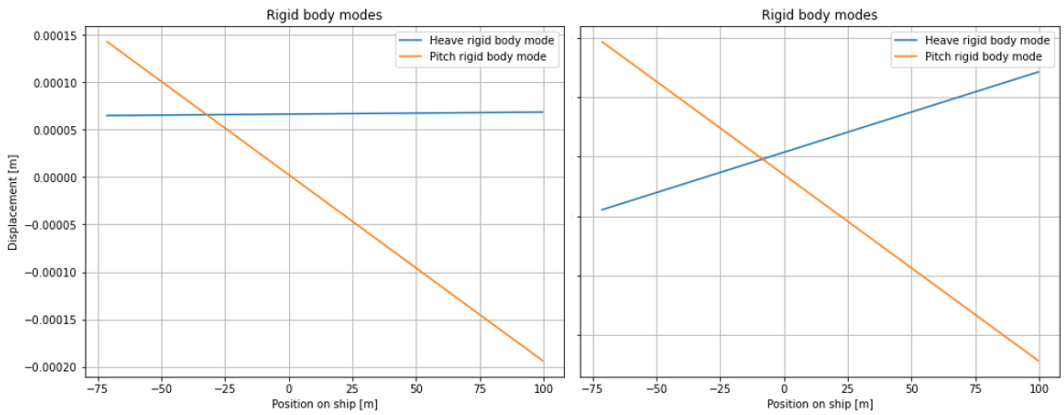

Figure E.19: Rigid body modes for different a different center of gravity

This is caused by the type of modeling chosen, since in reality the COG does not necessarily need to be above the center of flotation to have a heave rigid body motion. Within the model no information is present regarding the submerged volume of the vessel, which restricts the model to have a different equilibrium position besides the center of flotation.

E.2.3. Verification rigid body motions

The next step in verifying the hydrodynamic loadcase is to evaluate the rigid body motions resulting from the structural model. Figure E.20 shows the heave and pitch response amplitude operators. For the heave motion good accordance is observed, only some error is present near a wave frequency of 0.7 rad/s.

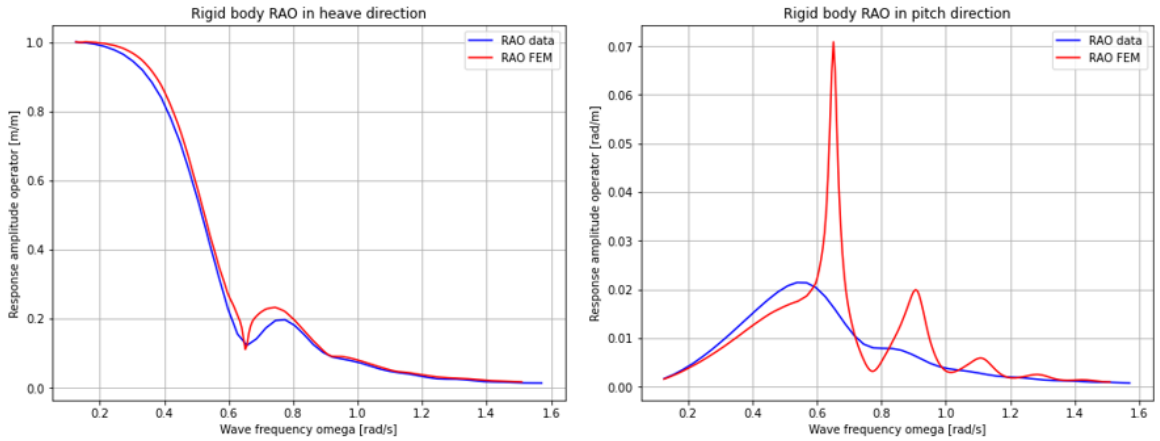

Figure E.20: Response amplitude operators for heave and pitch, based on heave force

For the response amplitude operator in pitch direction a larger discrepancy is observed. Here large oscillations between 0.6 and 1.2 rad/s are shown. After some further investigation the behavior shown in figure E.21 is discovered. This figure shows the wave force magnitude for wave frequencies of 0.6 and 0.68 rad/s. What is observed is that the wave forces become significant, causing the peaks observed in figure E.20.

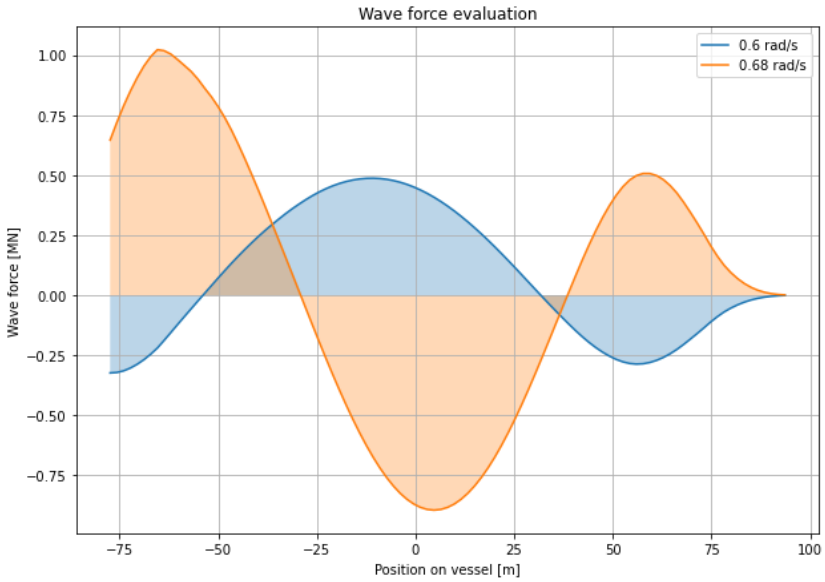

Figure E.21: Wave force over ship length for different wave frequencies

This problem is caused by the implementation of the equation shown in E.10. For some wave lengths,

corresponding to the peaks, the net resultant wave force becomes small. This small net resultant contribution causes the pressure amplitude to become large, to end up with the global heave force. The analysis can be done from a different point of view, by evaluating equation E.10 for the pitch bending moment $F_{5,a}$. The result of this analysis is shown in figure E.22. Here different behavior is observed, being that a better accordance for the pitch RAO is observed. For this case, the opposite is true for the heave direction. This is caused by the same behavior as shown in figure E.21, but then a low net moment contribution would result in high amplitudes.

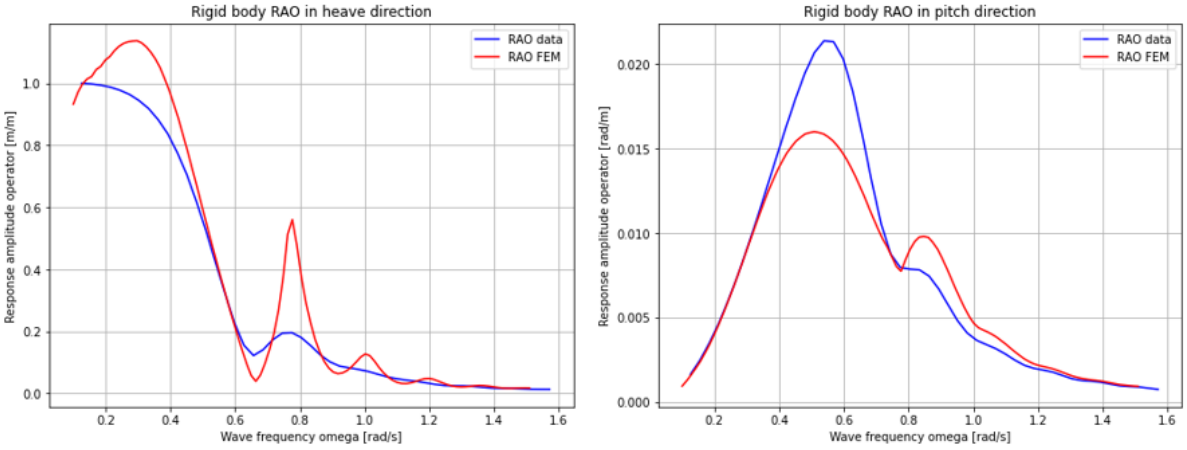

Figure E.22: Response amplitude operators for heave and pitch, based on pitch force

Furthermore, it is expected that an error is made in dicretizing the rotary inertia of the cargo and vessel. This because the behavior could match better to the measured data, and this is the case when the rotary inertia is increased. It is unsure where this error originates from. Besides this error, the right behavior is observed though.

The choice is made to continue with the pitch loadcase, and to make an error in the heave displacement. This is based on the maximum bending moment being the governing loadcase in sailing conditions. Selecting the heave loadcase would lead to a significant overestimation of the bending moment loads, which would then lead to high displacements.

E.2.4. Connection structural and hydrodynamic model

The models are connected in the manner shown in equation E.12, based on equation 2.4. Note that all components are expressed in the frequency domain. Furthermore, caution should be taken with respect to the frequency dependence of the added mass matrix **A** and the hydrodynamic damping **B**.

$$\left(-\omega^2\left[\mathbf{M}+\mathbf{A}(\omega)\right]+i\omega\mathbf{B}(\omega)+\left[\mathbf{K}+\mathbf{C}\right]\right)\mathbf{q}+\mathbf{f}_{nl}(\mathbf{q},\dot{\mathbf{q}})=\mathbf{f}_{w}(\omega) \tag{E.12}$$

E.3. Model implementation for case

Vessel parameters

The structural weight and stiffness distribution are the 2 main parameters which define the vessel. For the structural stiffness no distribution data was available, but for the midship section a value could be retrieved. Therefore an approximation for this distribution is made. Table E.7 shows some of the retrieved data. In this table parameters I_{mid} and A_{mid} repesent the structural stiffness and lateral steel area of the midship section. Note that this steel area consists only of the structural elements which are continuous in longitudinal direction, which is important in the stiffness matrix in equation 5.1. Other structural steel areas could lead to an incorrect longitudinal stiffness. Parameters ρ_s, E and v are material properties and represent the steel density, Young's modulus and the poisson ratio respectively.

Table E.7: Structural parameters MC-class vessel

Parameter	Value	Unit
I_{mid}	103.8	m^4
A_{mid}	4.78	m^2
ρ_s	7830	kg/m^3
E	205	GPa
v	0.3	$-$

Some other relevant data is obtained from BigLift and presented in figure E.23. This figure shows the bending strength and lightship weight distribution. The bending strength distribution is used to distribute the stiffness and lateral area over the vessel. This is done by normalizing it and multiplying by the midship stiffness or area.

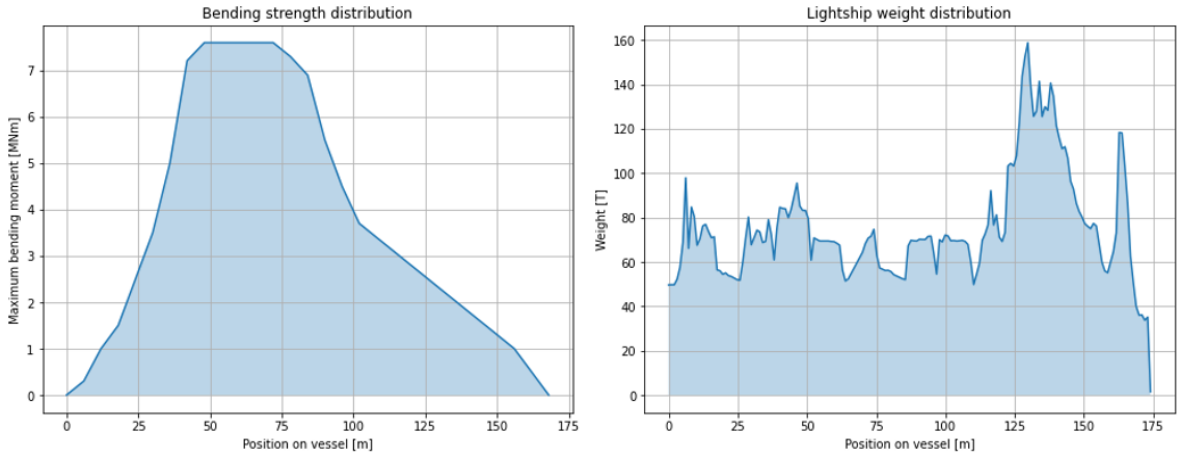

Figure E.23: Bending strength and lightship weight distribution for MC-class vessel

The remaining lightship weight is transformed into an structural steel area, by using equation E.13. This structural area is used in the element mass matrix. Here the assumption is made that the lightship weight has the same inertial properties as a beam.

$$\begin{aligned} m_s &= \rho_s \cdot V_s \\ A_s &= \frac{V_s}{\rho \cdot L_e} \end{aligned} \tag{E.13}$$

Cargo parameters

Within this research the ship is kept the same, which implies that these variables are kept fixed. Furthermore, the cargo variables are variables. To check the implementation in the model, an example cargo is presented here. This cargo is one of the largest monopiles currently existing, with structural parameters as shown in table E.8. Material properties are equal to those shown in E.7. These dimensions are retrieved from [15]. In the example case 4 monopiles will be assumed as the cargo.

Table E.8: Structural parameters example monopile [15]

Parameter	Value	Unit
L	112	m
D	8	m
t	10.4	mm
I_m	20.1	m^4
A_m	2.8	m^2

E.4. Difficulties implementing case in model

During the implementation of all elements within the model some difficulties arose, which are described in this paragraph.

Modeling of a free-free beam

At first, some difficulties arose during the modeling of a free-free beam in the non-linear model. Figure E.24 shows an example of this situation, for which the model was just able to converge. This figure shows that the beams start to rotate, since no constraint is present. If this rotation stays limited the model is still able to converge, but if it becomes extensive it breaks down.

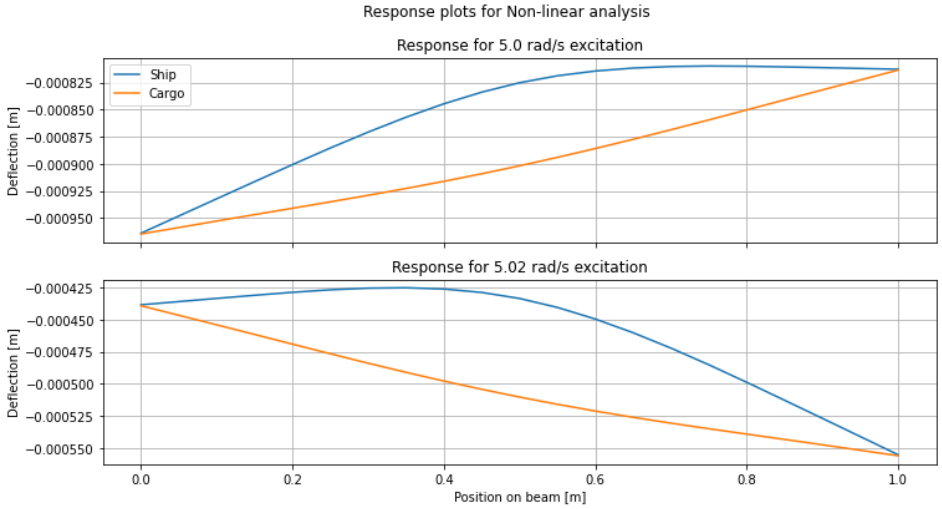

Figure E.24: Rotation of free-free beams

It was expected that implementing the hydrostatic stiffness in the model was able to resolve this problem, since this would constrain the beams in the model. After analysis it became clear that this is not the case, because of the difference in magnitude present for the structural and hydrostatic stiffness. For 20 elements, a structural stiffness of $\mathcal{O}(10^{12}\,\mathrm{N/m})$ is present, while the hydrostatic stiffness has a order of magnitude of $\mathcal{O}(10^{6}\,\mathrm{N/m})$.

What further complicates this problem is that an inverse relation between the structural stiffness K_{ij} and the element length L is observed. A linear relation is present for the hydrostatic stiffness C_{ij} and the element length L, a larger element length implies that the total hydrostatic stiffness needs to be distributed over a smaller amount of nodes. So, increasing the number of nodes only negatively influences this behavior, because the K_{ij} values become larger and the C_{ij} values becoming smaller. Paragraph E.4 further elaborates on the requirements regarding the nodes.

Modeling of unilateral springs

Some other difficulties arose regarding modeling the unilateral springs. Figure E.25 shows an issue observed when modeling unilateral springs. To mitigate the earlier identified problem with modeling a free-free beam, the cargo and ship are clamped at one side as shown in the left figure. The red dot on the geometry shows the point where the response in time is evaluated, as shown in the left figure. Note that, for simplicity, it is assumed that the cargo has the same length as the vessel.

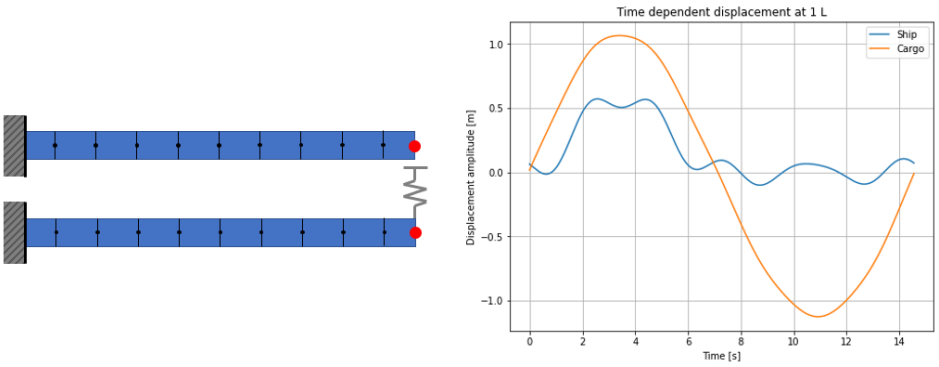

Figure E.25: Results for modeling unilateral constraint using ship and cargo

This figure shows right behavior in general, consisting of a displacement if the ship moves upward and being approximately zero if the ship moves downward. What is visible as well is that the saddle is compressed for almost 0.5 meters of displacement. This behavior could be solved by increasing the saddle stiffness, but this leads to a situation where no convergence is observed.

What complicates this situation is that the unilateral spring stiffness should be dependent on the order of magnitude of the displacement, if zero deflection in the saddle is desired. This is a complicated iterative process where stiffness should be found where the model is just able to converge. This leads to a high number of iterations for every specific observed displacement, being dependent on the loadcase.

Requirement high number of nodes

To obtain some geometric accuracy, it is required that a high number of nodes is present for the cargo and the ship. Based on the verification and validation analysis performed in appendix F it became clear that incorrect discretization of the beam leads to a significant deviation in results. Figure E.26 shows an example of this behavior, here the left figure is for 21 and the right for 18 nodes. In this case, selecting 18 nodes leads to a small offset in the location of the forcing and the non-linear springs. Furthermore, selecting 18 nodes introduces a-symmetries as well, which has a significant influence on the results as well.

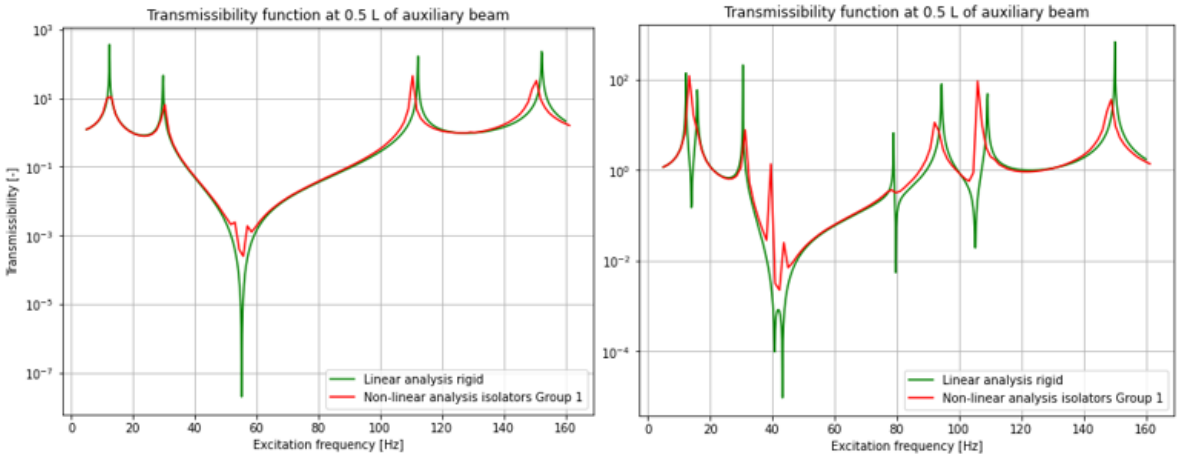

Figure E.26: Influence of number of nodes on results, the left figure shows the correct number and the right a wrong number of nodes

To conclude, the discretization needs to be performed in such a manner that the location of nodes and connections corresponds to their actual location. In the situation when a ship and its cargo is modeled it is expected that this leads to a high number of nodes, due to the geometric complexities. Furthermore, the earlier described distributions in the mass, stiffness, added mass, damping and hydrostatic stiffness pose some requirements on the discretization as well, in order to ensure accuracy. This contradicts

the requirement stated in E.4, in which there is stated that a low number of nodes is desired in order to preserve numerical accuracy.

Table E.9 shows the influence of nodes, iterations and harmonics on the runtime of a calculation. This table shows that especially for a high number of harmonics the runtime starts to become significant. In case of modeling unilateral constraints, a high number of harmonics is required to represent the solution as shown in figure E.25. Although the numerical efficiency of the Harmonic Balance Method is good compared to a time domain method, still the runtime becomes significant.

Table E.9: Runtime for different number of nodes and harmonics in seconds, for a single exitation frequency

		Nodes		
		11	*51*	*101*
Harmonics	*1*	0.1	2.7	12.5
	3	0.5	15.5	61.4
	5	1.4	145.1	1969.7

This runtime would be acceptable if valid results and convergence would be ensured, but this can't be ensured yet. Furthermore, debugging and testing becomes a tedious process in case of these large runtimes.

Modeling near eigenfrequencies

Another observation made during the validation of the model is some trouble with modeling near eigenfrequences. It is known that near eigenfrequencies the deflections become large, and, in case of no damping, even become infinite. This causes a lot of convergence issues for the solver, or problems in the continuation method. Figure E.27 shows this problem, in this situation the continuation method causes the solver to walk backwards on the solution path. The continuation method has trouble defining the direction vector, resulting in this problem.

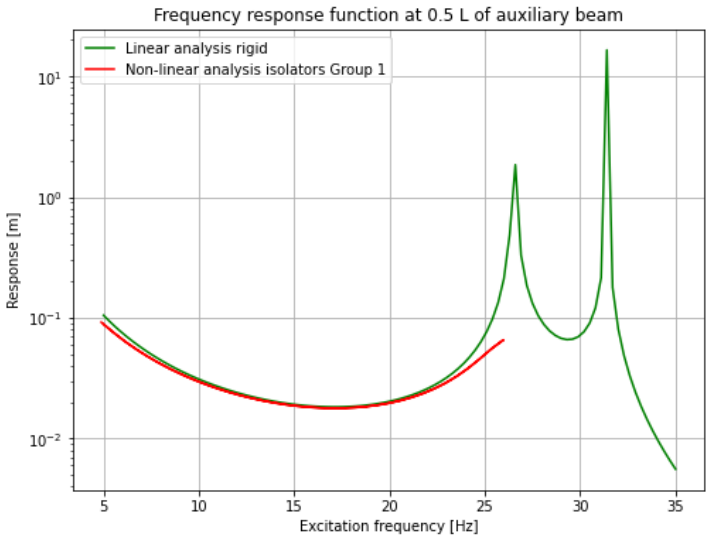

Figure E.27: Issues related to the continuation method

To resolve this problem it was expected that this could be solved by introducing hydrodynamic damping. This damping significantly reduces the response near eigenfrequencies, resulting in better convergence performance. It cannot be verified independently since no situation has been found in which the total situation could be modeled.

E.4.1. Potential solutions

Based on the difficulties mentioned above, some solutions can be identified. These solutions are as follows.

- First, a solution can be created where the model is more constrained, to prevent the rotation which causes trouble in the solver. An analysis should be made what type of constraint should be applied and how to take its influence in force and moment distribution into account.
- With respect to the behavior of the saddles, a solution can be found where an iteration is performed over the guesses. The solution that a solver finds is highly dependent on the quality of the guess provided.
- Better numerical performance could be obtained by separating the loop over a certain number of cores. This can be achieved by making different independent loops which follow and independent path of results.
- In situations close to eigenfrequencies an artificial amount of damping could be applied, leading to smaller deflections. By reducing the deflections, it should be easier for the solver to converge to solutions. The observed response would not be correct, but this should enable the model to identify the locations of eigenfrequencies.

Due to time considerations and the lack of conclusive evidence that it would work it is not possible to implement these solutions. Therefore, an alternative approach was identified, using a model where only one-way coupling is applied. This greatly reduces the complexity of the model and better allows for debugging and troubleshooting in the model. The approach and analysis done with this model is described in the main part of this thesis.

F

Verification & validation linear structural model

This appendix describes the validation and verification performed for the structural model. Verification and validation are based on the data obtained in experimental results, presented in [83]. The first study analyzes the eigenfrequencies for a simple strip, for simply supported and free boundary conditions [83]. Note these results are obtained for a free-free beam, with the dimensions as shown in table F.1. All results discussed in this appendix are based on this beam dimensions.

Table F.1: Eigenfrequencies from model and found in study [83]

Parameter		Value	Unit
Length	L	1.044	m
Breadth	B	0.023	m
Height	H	0.005	m
Density	ρ	7830	kg/m^3
Young's modulus	E	205	GPA

The appendix is structured as follows. First, the mathematical formulation of the analytical model is described. After that, results of the linear finite element method are described and compared to the analytical results. Finally, the validation of the linear model is described.

F.1. Analytical model

The analytical model is based on Euler-Bernoulli beam theory, which, on its order, is based on Newton's second law. This is shown in the first equation of F.1. This equation can be transformed into an ordinary differential equation of 2^{nd} and 4^{th} by assuming that the solution consists of a time- and space-dependent part. Solving the space-related differential equation results in the second equation shown in F.1.

$$\begin{aligned} &\rho_s \cdot A \cdot w(t,x)_{,tt} + EI \cdot w(t,x)_{,xxxx} = 0 \\ &\psi(x) = C_1 \cdot \cos(\beta \cdot x) + C_2 \cdot \sin(\beta \cdot x) + C_3 \cdot \cosh(\beta \cdot x) + C_4 \cdot \sinh(\beta \cdot x) \end{aligned} \tag{F.1}$$

The space-dependent solution can be solved by applying the appropriate boundary conditions at the beginning and the end of the beam. This solution results from the eigenvalue problem by putting together the boundary condition equations into a matrix. The eigenfrequencies result from requiring the determinant to be zero, which ensures nontrivial solutions.

Equation F.2 shows an example of some mode shape functions, defined for different boundary conditions. In this equation parameter β results from requiring the determinant to be zero. This parameter defines the mode shape and the eigenfrequency. Parameter L is the length of the beam, and x is the coordinate over the length of the beam.

$$\begin{aligned} \text{Free: } \psi &= \frac{\cos\beta L - \cosh\beta L}{\sinh\beta L + \sin\beta L}(\sin\beta x - \sinh\beta x) + (\cos\beta x + \cosh\beta x) \\ \text{Pinned: } \psi &= \sin\beta x \\ \text{Clamped: } \psi &= (\sinh\beta x - \sin\beta x) + \frac{\sinh\beta L - \sin\beta L}{\cos\beta L - \cosh\beta L}(\cosh\beta x - \cos\beta x) \end{aligned} \tag{F.2}$$

The eigenfrequency can be calculated using equation F.3 and is defined in radians per second. Note that this eigenfrequency corresponds to a specific mode shape. Parameters E and I are defined as the Young's modulus and area moment of inertia. The material density is defined by ρ, and the lateral area is defined by A.

$$\omega_i = \beta_i^2 \cdot \sqrt{\frac{EI}{\rho A}} \tag{F.3}$$

Figure F.1 shows some of the resulting mode shapes and eigenfrequencies in hertz. These results are valid for a beam with free-free boundary conditions

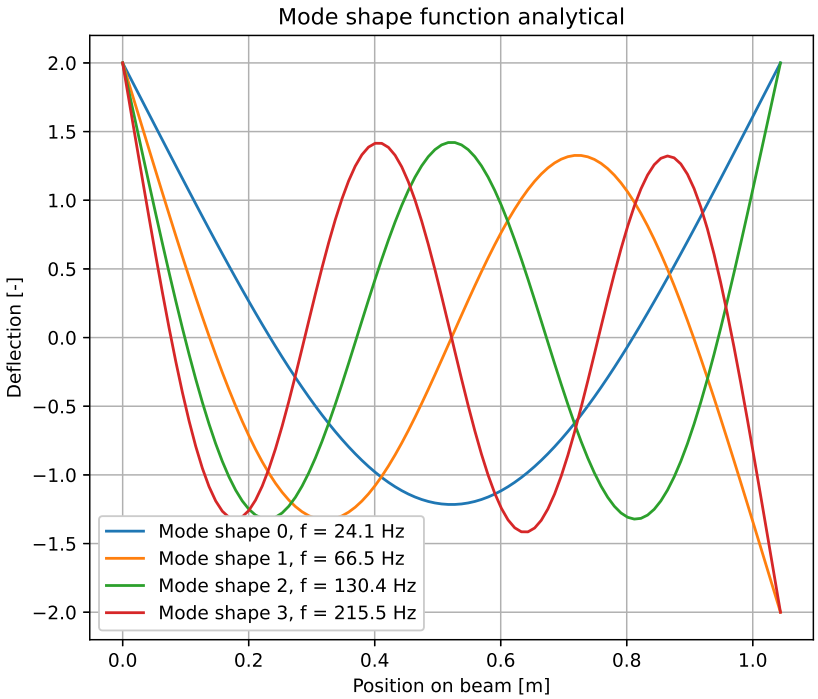

Figure F.1: Mode shapes and eigenfrequencies as defined by the analytical model

At last, a forced response situation is analyzed using the modal summation principle. Equation F.4 shows how the forced response per mode can be defined. To obtain the total response, the response per mode needs to be summed.

$$\frac{\tilde{X}_j}{\tilde{F}_k} = \sum_{i=1}^{n} \frac{\psi_{i,j}\psi_{i,k}}{m_{m,i}\left(\omega_i^2 - \omega_k^2\right)} \tag{F.4}$$

In this equation, j represents the location of the response, and k the location where the object is excited. Subscript i represents the certain mode. Parameter $m_{m,i}$ is defined as the modal mass. Figure F.2

shows the frequency response spectrum for the considered object. In this figure, the eigenfrequencies are clearly visible. Furthermore, destructive interference is visible as well between the modes.

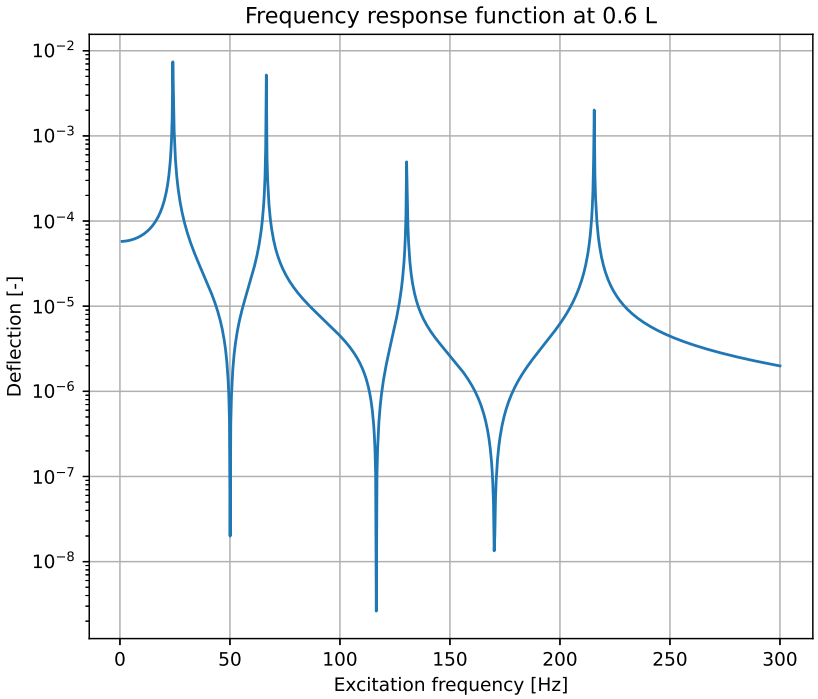

Figure F.2: Frequency response function for excitation and response at 60 % of the length of the beam

F.2. Finite Element Method model

The linearthеory discussed in chapter 5 is used as starting point here. The eigenfrequencies and mode shapes can be found using equation F.5 [73]. The first equation represents an eigenvalue problem, where the eigenvalues are represented by ω_i^2 and the eigenvectors by ψ_i. Note that this equation is solved for a free vibration solution. The second equation represents the response, which is defined to be harmonic. The last equation represents the forced vibration solution, with the amplitude being defined as α.

$$\begin{aligned} (\mathbf{K} - \omega_i^2 \mathbf{M})\boldsymbol{\psi_i} &= 0 \\ a = \boldsymbol{\psi_i} \cos(\omega_i t + \theta_i) & \\ (\omega_{ex}^2 - \omega_i^2)\alpha_i &= \boldsymbol{\psi_i^T} \mathbf{f} \end{aligned} \tag{F.5}$$

Solving these equations results in the mode shapes shown in figure F.3. Here, some different behavior can be observed compared to Figure F.1. Mode shape 0, 1 and 2 are defined as rigid body modes. Mode shape 2 is the rigid body mode in x direction, therefore the y-deflection is equal to 0. Mode shape 0 is the rigid body mode in y-direction, and mode shape 1 is the rigid body mode in θ-direction. These rigid body motions do not directly result from the analytical analysis, so therefore they are only observed for the finite element analysis. Note that for these modes there is no eigenfrequency, since no bending vibration is present in the mode. At last, the first bending mode, represented by mode shape 3, has the same shape and eigenfrequency as defined by the analytical model.

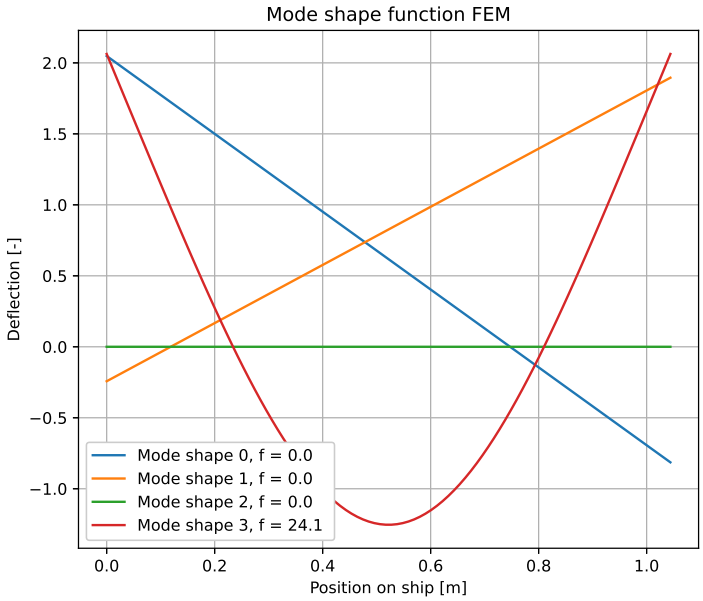

Figure F.3: Mode shapes based on Finite Element Method

Boundary conditions

Some boundary conditions between the beams are modeled in order to create a multi-beam model. The beams can be connected using a rotated beam element. To do so, a rotation matrix should be applied to the element stiffness and mass matrix. This rotation matrix R is shown in equation F.6. The operations required to rotate the element matrices are shown as well in this equation.

$$[\mathbf{R}] = \begin{bmatrix} \cos\theta & \sin\theta & 0 & 0 & 0 & 0 \\ -\sin\theta & \cos\theta & 0 & 0 & 0 & 0 \\ 0 & 0 & 1 & 0 & 0 & 0 \\ 0 & 0 & 0 & \cos\theta & \sin\theta & 0 \\ 0 & 0 & 0 & -\sin\theta & \cos\theta & 0 \\ 0 & 0 & 0 & 0 & 0 & 1 \end{bmatrix} \tag{F.6}$$

$$[\mathbf{M_{rot}}] = [\mathbf{R}]^T[\mathbf{M_e}][\mathbf{R}]$$

$$[\mathbf{K_{rot}}] = [\mathbf{R}]^T[\mathbf{K_e}][\mathbf{R}]$$

Furthermore, for a pinned condition the stiffness matrix shown in equation F.2 is used. In this situation, the stiffness k is put to a high value, in order to force the displacement of the vessel and cargo to be the same.

$$[\mathbf{K_{pinned}}] = \begin{bmatrix} k & 0 & 0 & -k & 0 & 0 \\ 0 & k & 0 & 0 & -k & 0 \\ 0 & 0 & 0 & 0 & 0 & 0 \\ -k & 0 & 0 & k & 0 & 0 \\ 0 & -k & 0 & 0 & k & 0 \\ 0 & 0 & 0 & 0 & 0 & 0 \end{bmatrix} \quad [\mathbf{K_{clamped}}] = \begin{bmatrix} k & 0 & 0 & -k & 0 & 0 \\ 0 & k & 0 & 0 & -k & 0 \\ 0 & 0 & k & 0 & 0 & -k \\ -k & 0 & 0 & k & 0 & 0 \\ 0 & -k & 0 & 0 & k & 0 \\ 0 & 0 & -k & 0 & 0 & k \end{bmatrix}$$

Table F.2: Caption

Note that to apply these boundary conditions, the to-be-connected nodes of the vessel and cargo need to be obtained. The stiffness and mass matrix are split into four 3 by 3 matrices, which need to be placed onto the correct nodes in the global stiffness matrix.

F.3. Further verification and validation of model

This paragraph describes how the model is verified and validated. Note that the Finite Element model for continuous beam is validated by the analytical model. More complex structures and discontinuities are verified or validated by ANSYS, or by literature.

Table F.3 shows the comparison between the analytical, FEM and experimental results. Note that the eigenfrequencies are corresponding to the bending modes. Furthermore, only 5 elements are required to obtain the eigenfrequency within 1 % accuracy for the third eigenmode. Note that this error increases for higher order modes. The table shows that, in general, the results correspond well. The only mode with a high deviation is mode 2, in their paper they don't mention why this difference is large. It could be that some error is introduced by the supports of the beam, since it is not possible to obtain a fully free-free situation.

Table F.3: Parameters beam used in [83]

Boundary condition	Mode	Experimental freq.	Analytical freq.	Finite element freq.
free-free	1	25.63	24.13	24.13
	2	77.51	66.51	66.51
	3	128.8	130.4	130.4
pinned-pinned	1	12.21	10.64	10.64
	2	37.62	42.57	42.57
	3	-	95.79	95.79

Stepped beam

A discontinuity which is verified for the FEM-model is the stepped beam shown in figure F.4 [84]. Note that free boundary conditions are applied on this stepped beam.

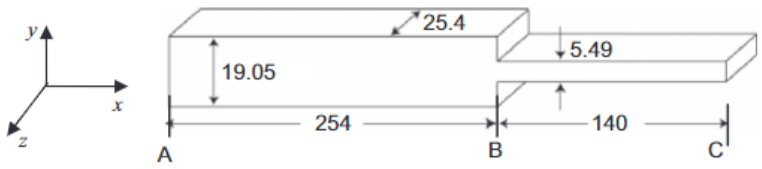

Figure F.4: Stepped beam considered in study [84], dimensions are in millimeters

Table F.4 shows the comparison between the result from the study and from the finite element model. Note that in this study, a composite element method (CEM) is applied. The results show good agreement with each other, with the error being around 0.5 percent. This confirms that the implemented method to handle discontinuities is valid.

Table F.4: Eigenfrequencies of model and of study [84]

Mode	Study freq.	Finite element freq.
1	291.9	293.13
2	1176.2	1182.0
3	1795.7	1805.9

Figure F.5 shows the mode shapes for the stepped beam. These mode shapes show the correct behavior as well, with a clear difference in stiffness visible. This further confirms that the FEM-model is able to handle complex geometries.

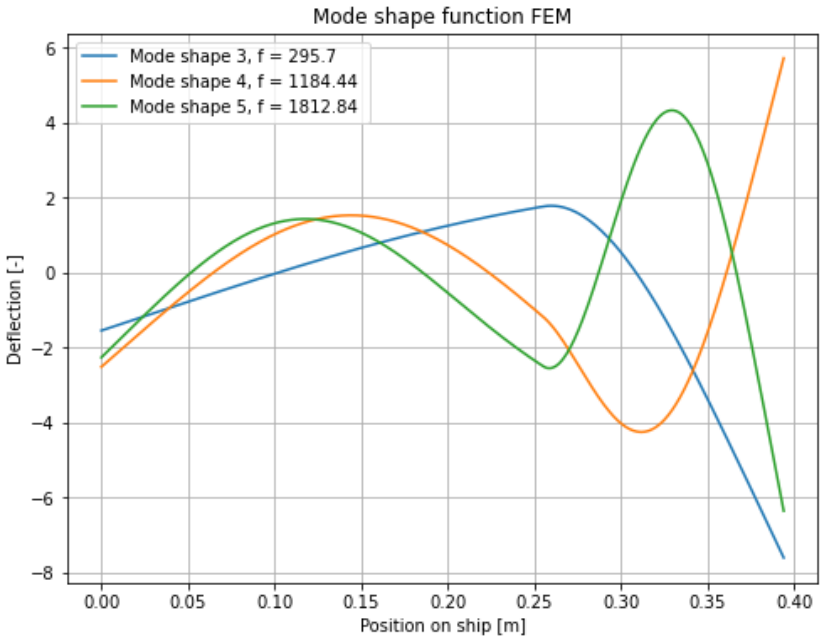

Figure F.5: Mode shapes for beam discussed in [84]

Multi-beam structures

At last, an analysis is made as well to verify the results of multi-beam structures. This is done by setting-up an ANSYS-model. Figure F.6 shows the multi-beam model created in ANSYS.

Figure F.6: Multi beam model created in ANSYS

Table F.5 shows the eigenfrequencies for certain modes. This table shows that the results have a minimal difference. This shows that the FEM-model is able to model multi-beam structures as well.

Table F.5: Eigenfrequencies of model and of study [84]

Mode	ANSYS freq.	Finite element freq.
1	0.273	0.275
2	0.895	0.886
3	1.012	1.012

G

Verification & validation non-linear structural model

This appendix describes how the non-linear modeling method is verified and validated. The verification is based on two different approaches, using ANSYS and the study of Wang and Zheng [85].

G.1. Verification using ANSYS

In order to verify the created model some cases are created. These cases are analysed in ANSYS and by the model, and defined as follows:

- Clamped beam with non-linear spring
- Clamped beam with unilateral spring
- Clamped multi-beam attached by non-linear springs

The verification of these cases are discussed individually with their added value to the legitimacy of the model.

Case 1: Clamped beam with cubic spring

Figure G.1 shows a schematic representation of the analyzed situation. Note that the red arrow represents an oscillating force. The accordance between the model and ANSYS confirms that the applied solution method is able to find correct results for non-linear systems. Caution should be paid that the exciting force is sufficient to generate a significant response, so the non-linear forces become pronounced.

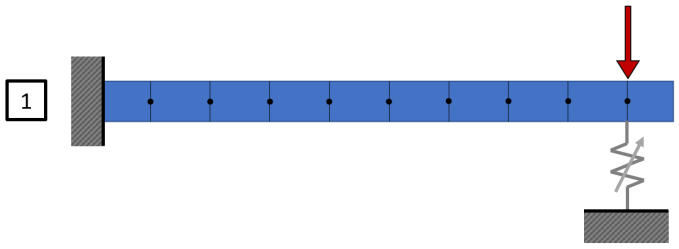

Figure G.1: Clamped beam with non-linear spring

Table G.1 shows the beam, loading and non-linear stiffness properties. These beam properties are arbitrary, but chosen in the same order of magnitude as beams used in [51, 84, 85]. Both these parameters are loaded in the ANSYS and Python models, and a response analysis is made. Note that the response is evaluated at the end of the beam, so where the cubic spring is located.

Table G.1: Beam, loading and non-linear stiffness properties tested in case 1

Parameter		Value	Unit
Length	L	0.1	m
Breadth	B	0.005	m
Length	H	0.005	m
Young's modulus	E	205	GPa
Density	ρ	7830	kg/m^3
Load	P	1000	N
Frequency	f	33.3	Hz
Stiffness	k	6	GN/m^3

The figures in G.2 show the results from the ANSYS and Python-model. These figures show a good agreement, the magnitude of the response is similar. Note that for the ANSYS model some smaller vibrations are observed. In the Python-model some small vibrations are visible as well, but with a smaller magnitude. Therefore, it is expected that this is transient behavior, while the Python model is only able to model steady-state behavior. Note that a trade-off should be made between harmonic order and runtime, since the runtime increases drastically if the harmonic order is increased.

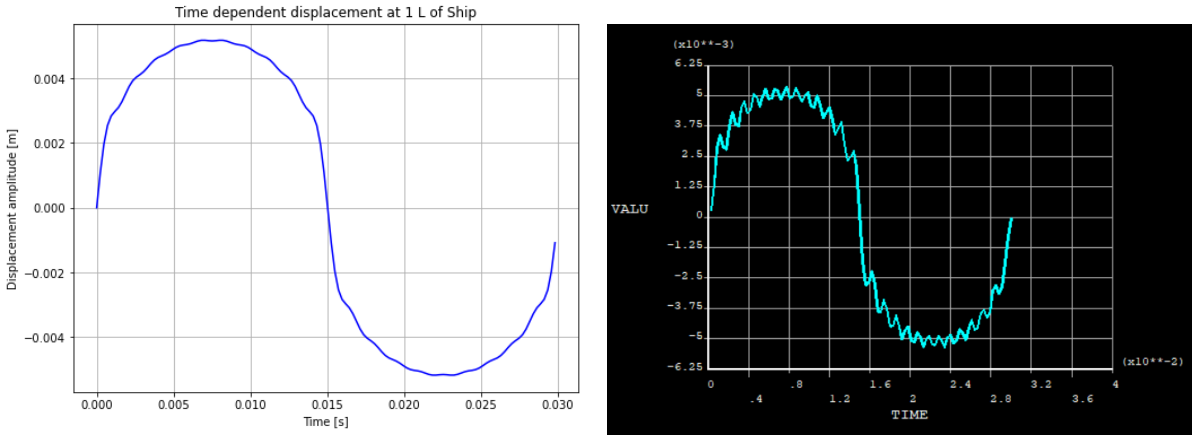

Figure G.2: Response end of beam based on Python-model (left) and ANSYS (right)

Table G.2 shows the numerical results. Only a difference of 4 % is observed between the results.

Table G.2: Comparison deflection computed by ANSYS and Pyhton-model

Method	Result
Python	0.00515
ANSYS	0.00536
Difference	3.8 %

Case 2: Clamped beam with unilateral spring

Figure G.3 shows a single beam model with a unilateral spring at the end. This case is of particular interest since the unilateral spring causes a highly non-linear situation, due to the discontinuity in the force-deflection curve of the spring. This causes the suspicion of potential errors due to the Gibbs-phenomenon, emphasizing a thorough analysis. The gap in the figure is shown to illustrate the unilateral spring, but this distance is modeled to have a value of 0.

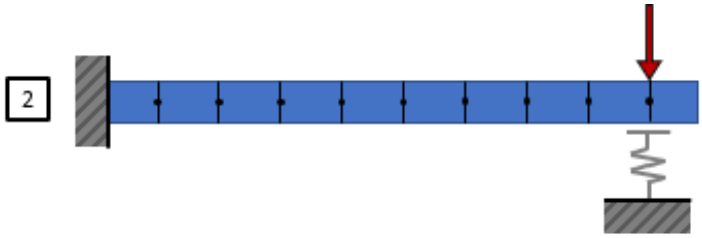

Figure G.3: Clamped beam with unilateral spring

Note that the properties of the beam and load are the same as shown in table G.1. Table G.3 shows the properties of the unilateral spring. This spring is modeled as a linear spring.

Table G.3: Unilateral spring properties tested in case 2

Parameter		Value	Unit
Stiffness	k	6	MN/m
Gap	e	0	m

Figure G.4 shows the results from the Python-model and ANSYS. Note that the spring resists movement above $x = 0$, but has no influence below this value. The ANSYS results show more oscillations compared to the Python-model, but here the same conclusion is drawn as in the first case.

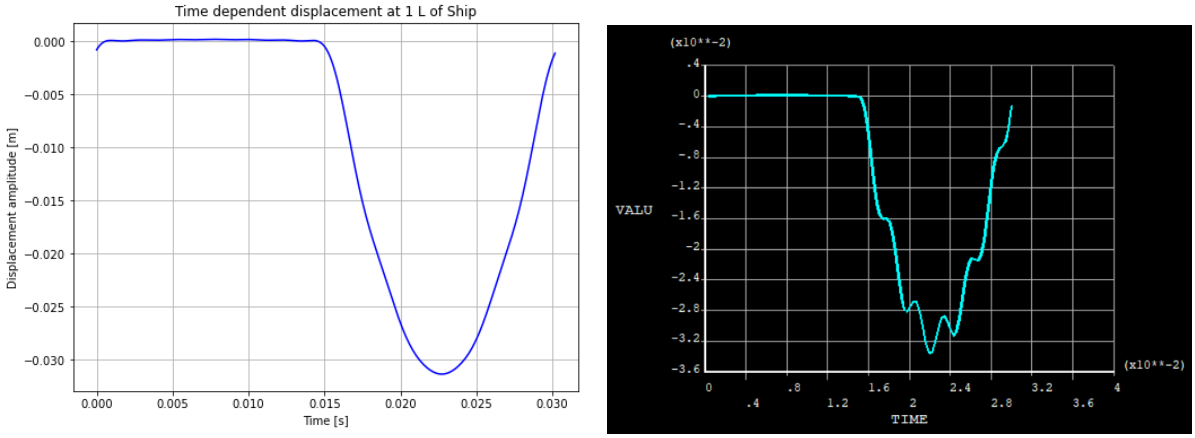

Figure G.4: Response end of beam based on Python-model (left) and ANSYS (right)

Table G.4 shows the numerical results for the second case. Here the difference increases to 6 %.

Table G.4: Comparison deflection computed by ANSYS and Pyhton-model

Method	Result
Python	-0.0314
ANSYS	-0.0335
Difference	6.3 %

Some additional analysis is made since the Python-model had trouble to converge to this result, a long calculation time and many iterations were required. Especially when the stiffness was increased even further, the model would break down. This issue is important to analyze, because the situation could occur that the axial stiffness of the saddles will be far larger than the bending stiffness of the monopiles.

Figure G.5 shows the force and deflection at the location of the unilateral spring for one oscillation

over time. The blue curve shows the guess for the displacement over time, based on which the green curve is calculated. The green curve represents the force due to this displacement, evaluated in time domain. Using the fourier transform this curve is tranferred into frequency domain, represented by the red curve.

The left figure shows a substep in the iterations to find the solution and directly makes clear why the solver has trouble finding the actual solution. Harmonics with a small amplitude lead to a large force, because of the unilateral spring with high stiffness. A check has been performed to verify whether or not the Gibbs phenomenon influences this behavior, but this is not observed. This is done by smoothing the time domain force at the discontinuities around 0.

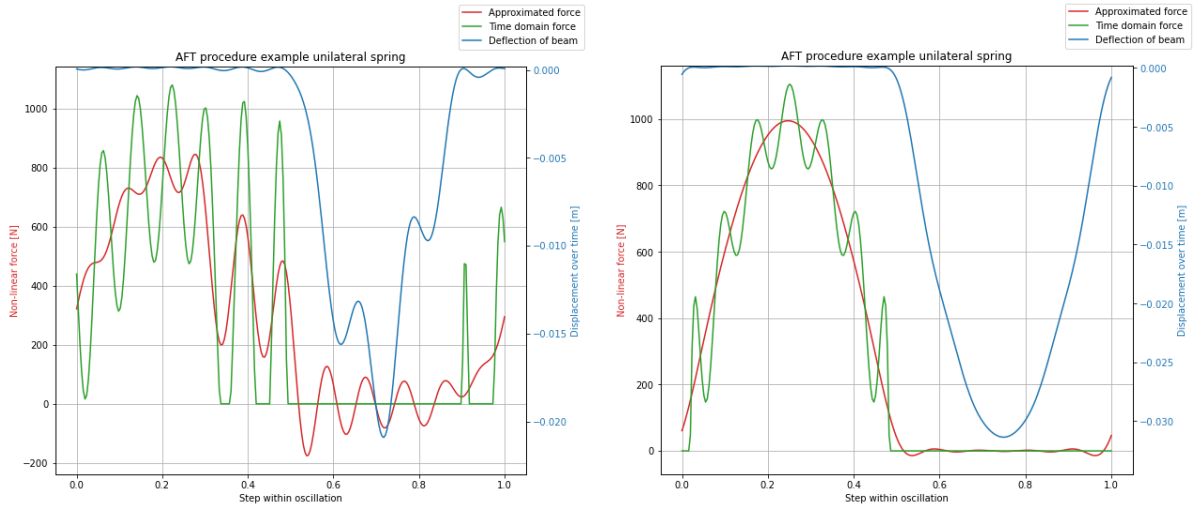

Figure G.5: Beam deflection and unilateral spring force for a substep (left) and for the end result (right)

To solve this issue a different spring representation for the saddles needs to be investigated. It is expected that a quadratic or cubic spring would reduce this behavior. Figure G.6 shows the force deflection curve for a linear and a quadratic spring. By implementing a quadratic spring, the reaction force for small amplitudes will be smaller compared to a linear spring. But for larger amplitudes this force will exceed the linear one.

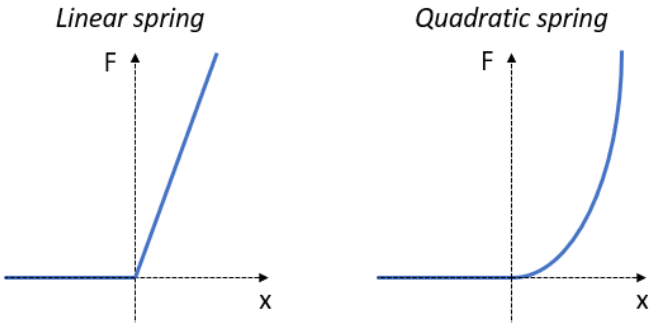

Figure G.6: Force deflection curves for unilateral linear and quadratic spring

Implementing the saddles in this manner has some consequences which need to be considered. So will the deflection at the locations of the saddles not be accurate anymore, up to a certain point the monopile will deflect the saddles more than in reality. This is not considered to be a problem, since this research is focused on detachment of the monopile instead of the deflective behavior at the saddles. Note that for other applications where this behavior is important the model might become inaccurate. Table G.5 shows a comparison results for different spring implementations. Note that the springs stiffness needs

to be increased for a higher order spring, to ensure that the maximum deflection stays limited. A cubic spring will be implemented, since this gives accurate results with limited iterations. Furthermore, cubic springs ensure smoothness for force deflection curve, but as well for its derivative. This is useful since the Jacobian is used in the solver.

Table G.5: Comparison implementation springs

Method	Stiffness	Min	Max	Iterations
Linear	6e6	-0.03145	0.00018	126
Quadratic	6e9	-0.03145	0.00042	78
Cubic	6e12	-0.03147	0.00056	55

G.2. Validation using literature

In order to be able to validate model using the paper, a continuation method needs to be implemented. This is based on the fact that now a range of frequencies is evaluated instead of a single exictation frequency.

G.2.1. Continuation method

Chapter 5 describes how the system equations can be solved using the harmonic balance method. As identified in the literature review, a continuation method is also required when creating frequency response curvers. This continuation method ensures that complex behavior like bifurcations is managed correctly, that all solutions are found for a given excitation frequency.

At first, a predictor step is required in the continuation method. A common method applied to define a predictor is the tangent method, shown mathematically in equation G.1. In this equation, $\mathbf{X}_0$ represents the previous solution, Δs the step size and $\mathbf{X}_1^*$ the normalized tangent vector [51].

$$\mathbf{X}^{pre} = \mathbf{X}_0 + \Delta s \mathbf{X}_1^* \tag{G.1}$$

As the corrector step, various methods are present as well. Figure G.7 shows some of the options. The mathematical representation of the arc-length and orthogonal continuation is shown in equation G.2. For the arc-length algorithm, the next solution point needs to be on the sphere with a radius of Δs. For the orthogonal algorithm, the next solution point needs to be on the plane tangent to the solution point.

$$\begin{aligned} \text{Arc-length: } & p_{\mathsf{c}}(\mathbf{X}) = (\mathbf{X} - \mathbf{X}_0)^{\mathsf{T}} (\mathbf{X} - \mathbf{X}_0) - \Delta s^2 = 0 \\ \text{Orthogonal: } & p_{\mathsf{c}}(\mathbf{X}) = \mathbf{X}_1^{\mathsf{T}} (\mathbf{X} - \mathbf{X}^{\mathsf{pre}}) = 0 \end{aligned} \tag{G.2}$$

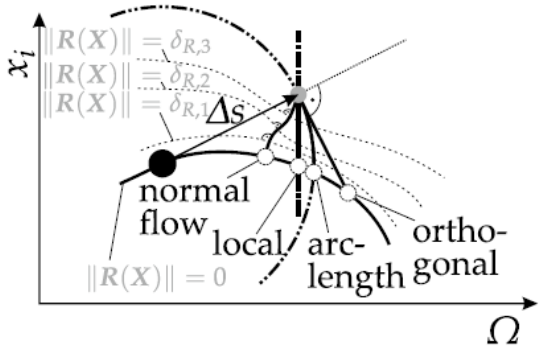

Figure G.7: Corrector methods [51]

The Python model with the continuation method is compared to the MATLAB tool NLvib in order to verify the implementation. Figure G.8 shows the comparison between the two tools, and the results show good accordance.

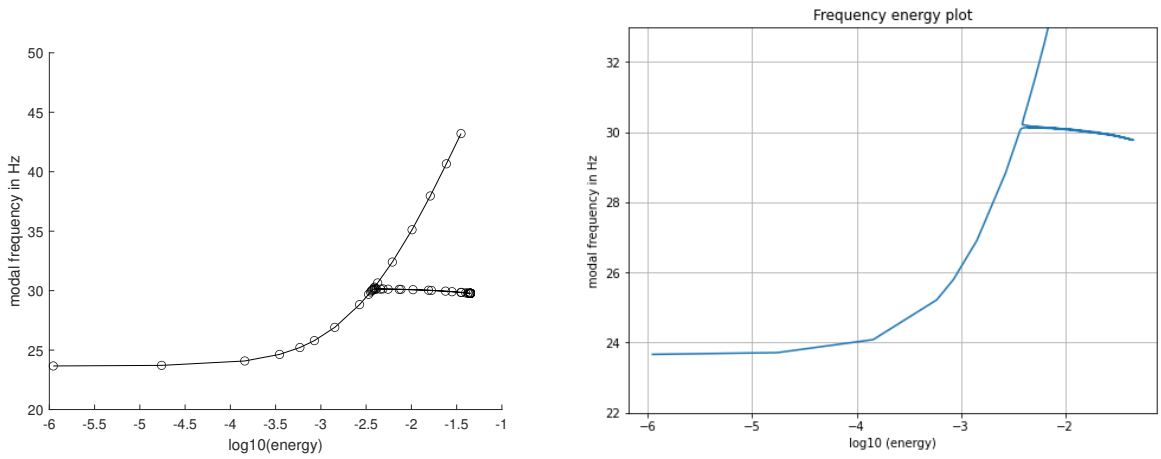

Figure G.8: Comparison between the MATLAB (left) and Python tool (right)

G.2.2. Reference case comparison

A reference case is found in the paper of Wang and Zheng [85]. In this paper they analyse the frequency response of a multi-beam configuration connected by non-linear springs. They evaluate the response in a analytical and a experimental manner. Figure G.9 shows the configuration of the test setup. A close-up of the non-linear isolator is shown in the bottom left of the figure.

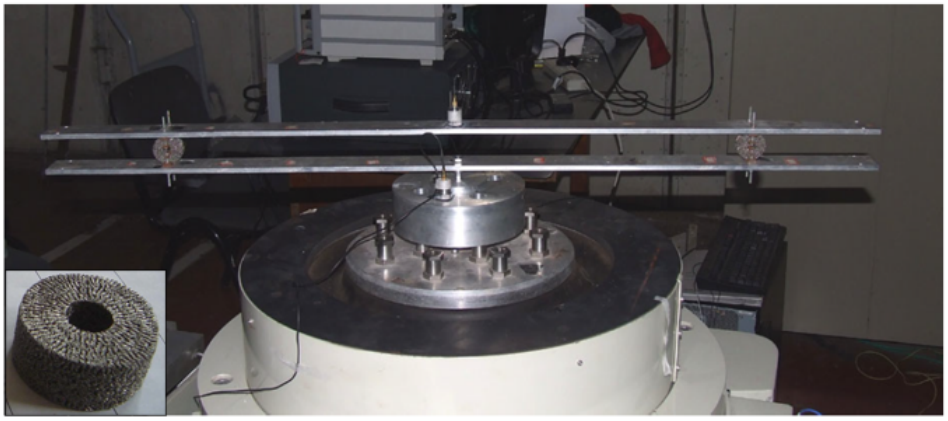

Figure G.9: Test set up of multi-beam configuration connected by non-linear isolators [85]

Modeling of isolators

The first step in analyzing this case is to model the non-linear isolators. The first part of the paper is related to the modeling and parameter identification of these isolators. Figure G.10 shows the single degree of freedom system used to identify the parameters of the non linear isolator [85].

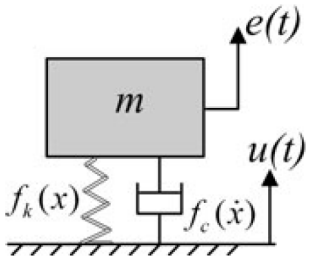

Figure G.10: Single degree of freedom system non-linear isolators [85]

To identify these parameters, the isolator is connected to a mass and applies a base excitation. In order to apply a base excitation, equation G.3 should be taken into account. This equation is based on the coordinates shown in figure G.10. This implies that the term $mu_0\omega^2$ represents the excitation force. Caution should be paid to $x(t)$ being the relative motion, $e(t)$ the response motion, and $u(t)$ the base excitation. The last equation shown represents the non-linear force description. The parameters c_1, c_3, k_1, k_2 and k_3 are defined in their study by parameter identification based on experiments. These parameters are adopted in the non-linear model to evaluate the response.

$$\begin{aligned} x(t) &= e(t) - u(t) \\ m\ddot{e} + f_c(\dot{x}) + f(x) + f_{nl}(x,\dot{x}) &= mu_0\omega^2 e^{j\omega t} \\ f_{nl}(x,\dot{x}) &= c_1\dot{x} + c_3\dot{x}^3 + kx_1 + k_2 x|x| + k_3 x^3 \end{aligned} \tag{G.3}$$

This translates to a single degree of freedom system, and is modeled in the MATLAB tool NLvib. Figure G.11 shows response curves for the springs considered in the research. Good accordance is observed between the results from the study of Wang and Zheng and the harmonic balance method.

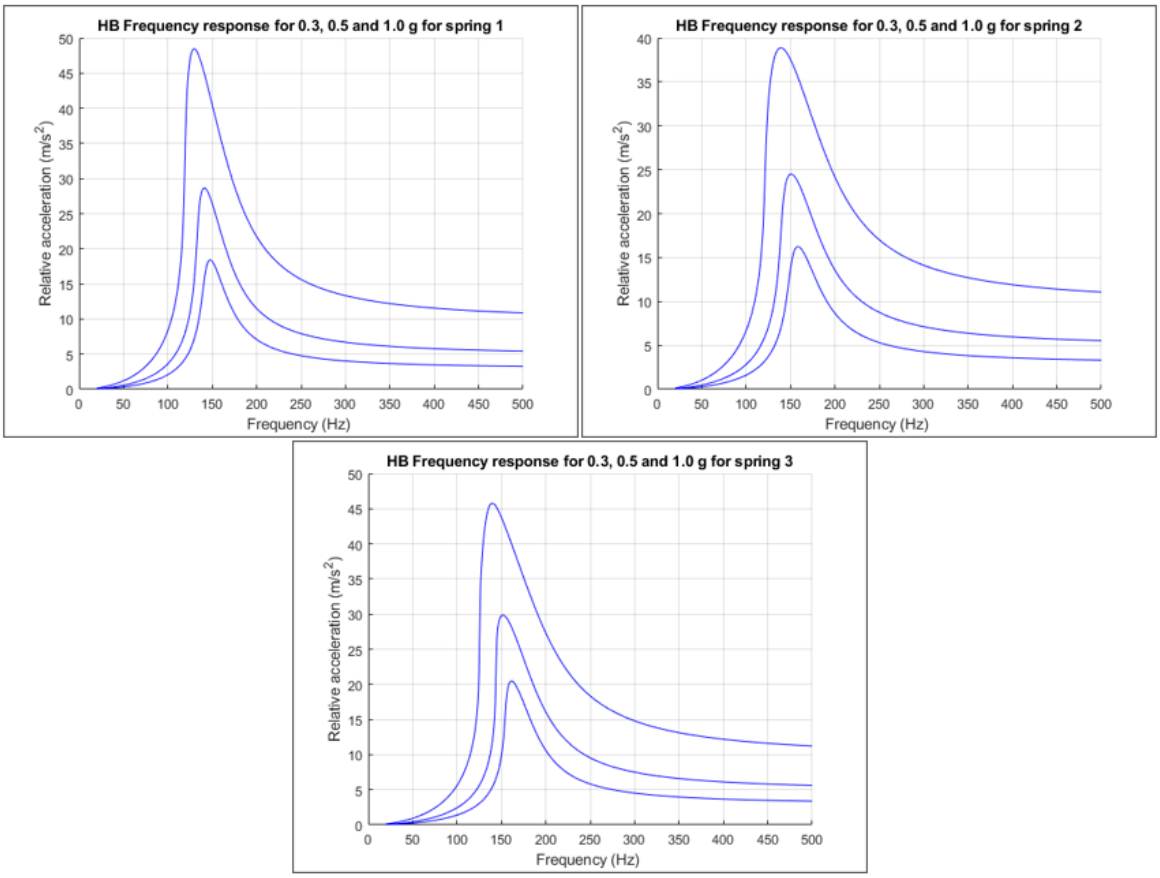

Figure G.11: Comparison between results from the tool and the study [85]

Modeling of multi-beam structure

The next step is to model the multi-beam part, now it is clear that the non-linear isolators are modeled correctly. Figure G.12 shows the transmissibility curves for the first isolators. If compared to the paper of Wang and Zheng, it shows the correct behavior and deviations from the rigid connection analysis.

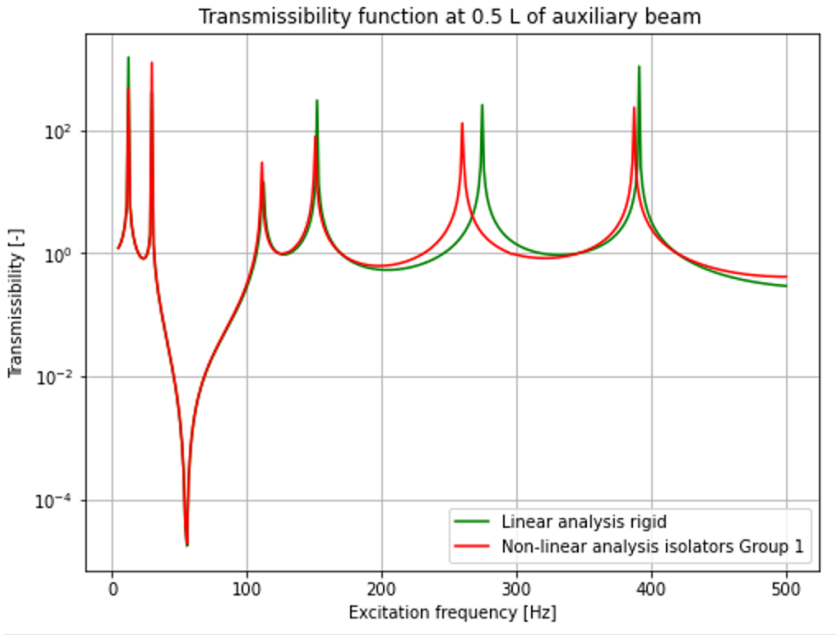

Figure G.12: Comparison transmissibility curves for rigid connection and non-linear isolators group 1

Table G.6 shows the observed peak frequencies. This table shows that the results compare good to the values found by Zang and Wheng. Therefore, the conclusion can be drawn that the model is able to define this part of the behavior correctly.

Table G.6: Peak frequencies comparison

Mode	Rigid	Group 1 W & Z	Group 1	Difference	Group 1 Linear
1	12	12	12.4	0 %	12.3
2	30	29	29.8	3 %	29.8
3	112	117	111.2	5 %	111.1
4	152	154	150.9	2 %	150.8
5	275	257	260.1	1 %	259.4
6	391	385	387.3	1 %	386.9

After some more analysis, the situation shown in figure G.13 was encountered. This figure shows a comparison between a non-linear analysis, and an analysis of the linearised problem. This figure shows that the behavior is predominantly defined by the linear part. This is shown in table G.6 as well, the peak frequencies have a small difference. Therefore, further investigation is required in order to validate the model.

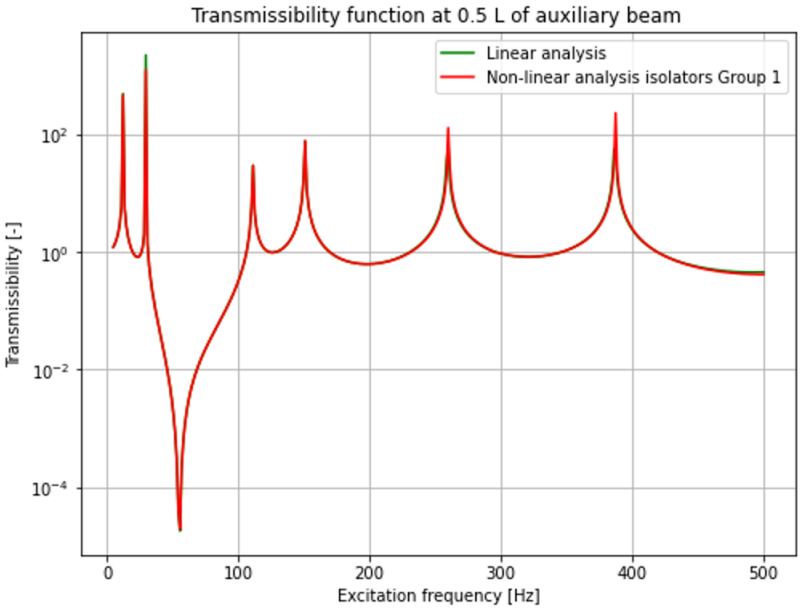

Figure G.13: Transmissibility curves comparison for linearised and non linear analysis

Table G.7 shows the other data that Wang and Zheng used in their research. The proportion stated in the table is the proportion between the deformation of the springs and the maximum deflection of the beams. Here, a larger discrepancy is observed. The general behavior is observed in this table, but the numerical values are off. One possible explanation for this could be that evaluations are made at frequencies where extremes are located. Because of doing this, differences get magnified, causing a bad correlation. Another explanation is the difference in solution methods, causing different numerical values.

Table G.7: Deflection of beam-deflection of spring proportion comparison

Mode	Mode 1	Mode 2	Mode 3	Mode 4	Mode 5	Mode 6
Proportion W&Z	0.0013	0.0021	0.0211	0.0418	0.7817	0.0492
Proportion	0.00165	0.00081	0.01812	0.0291385	0.16598	0.0801
Deflection spring	-1.01625e-06	2.53917e-06	-1.38405e-06	1.89042e-06	2.22001e-06	9.50677e-07

Furthermore, table G.7 shows the deflection of the springs as well. This data cant be verified since it is not provided in the paper, but it draws attention nevertheless. Figure G.14 shows the force deflection curve for nonlinear springs group 1. This figure shows that the springs have soft behavior for low deflections, but become more stiff for higher deflections. If the order of magnitude of deflection is analysed, it becomes clear why the observed behavior is linear. The small deflections caused it to behave in a linear manner, as represented by the yellow line.

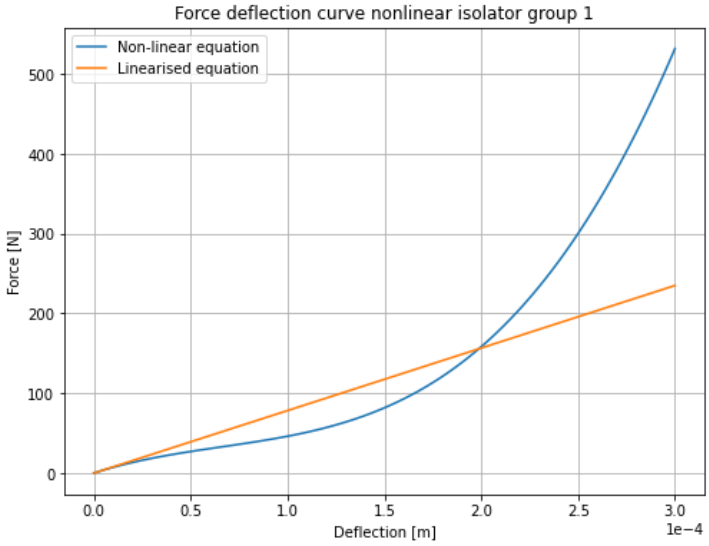

Figure G.14: Force deflection curve for non-linear isolators group 1

Therefore, the non-linearities in the system are analyzed more closely. The system will be excited with a larger amplitude. This analysis is performed for mode 5, since the deviations between the non-linear and rigid solution is largest. Therefore, the effects of changing the exciting force will be most pronounced here. The original results are obtained with an excitation of 0.4 g. Figure G.15 shows the results for an excitation of 20 and 60 g.

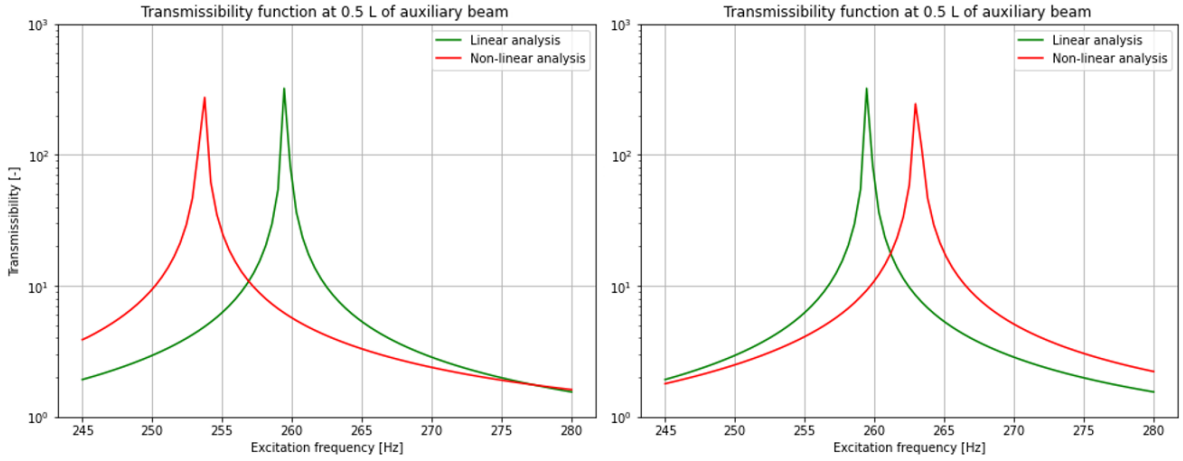

Figure G.15: Transmissibility curves for 20 g (left) and for 60 g (right) excitation

The left figure shows an transmissibility peak earlier than for the linearized system, indicating a smaller stiffness contribution. For the right figure, the opposite is observed. This behavior is analyzed in combination with the force deflection curve presented in figure G.16. This curve explains the earlier observed behavior. When excited with a low force, the spring deflects in the regime where it is considered soft. This implies a lower stiffness compared to a linear spring, explaining the shift observed in the left figure ofG.15. For higher excitations, the spring will operate in a more stiff regime, expecting results to converge to the rigid connection results. This behavior is observed in the right figure of G.15.

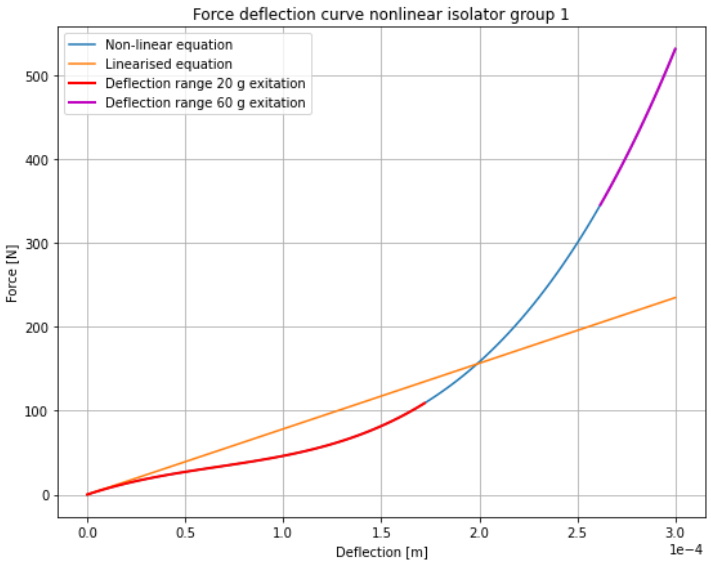

Figure G.16: Force deflection curve non-linear isolators with attained range for 20 g and 60 g excitation

H

Additional results parametric analysis saddles

Linear deflection

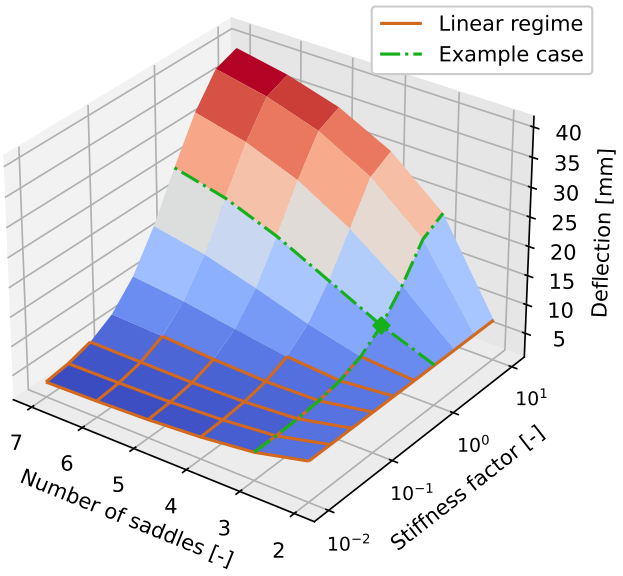

Non-Linear deflection

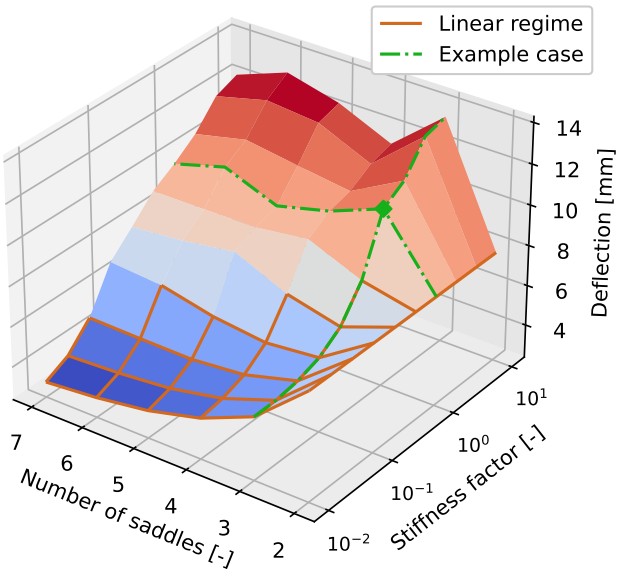

Non-Linear detachment

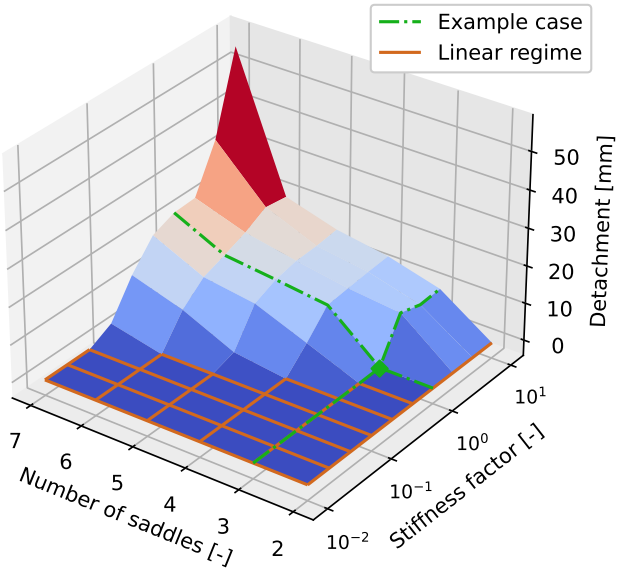

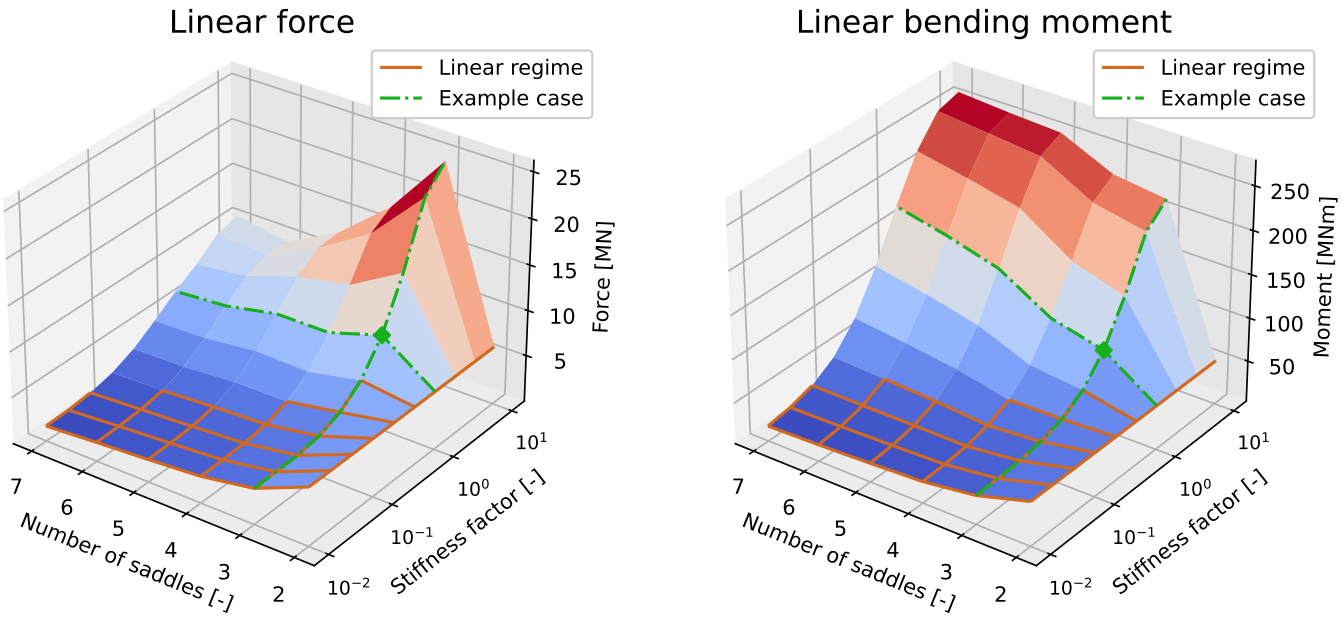

Figure H.2: Additional results for parametric analysis number of saddles and saddle stiffness. Every results is the maximum value observed.

I

Example case saddle analysis

The figures shown in figure I.1 show the force distribution during the oscillation and at $t = 0$. Two reasons can be identified why the non-linear forces in the seafastening system are larger compared to the observed linear forces. At first, the large linear negative force at the outer saddles causes the monopile to stay connected to the middle three saddles. This causes them to distribute the normal force over these three, instead of being taken up by one, as shown for the non-linear force distribution. Second, the tensile force caused by the force regularization is amplified by the stiffness. This results in a larger negative force observed for the second and fourth saddle, if compared to figure 5.3.

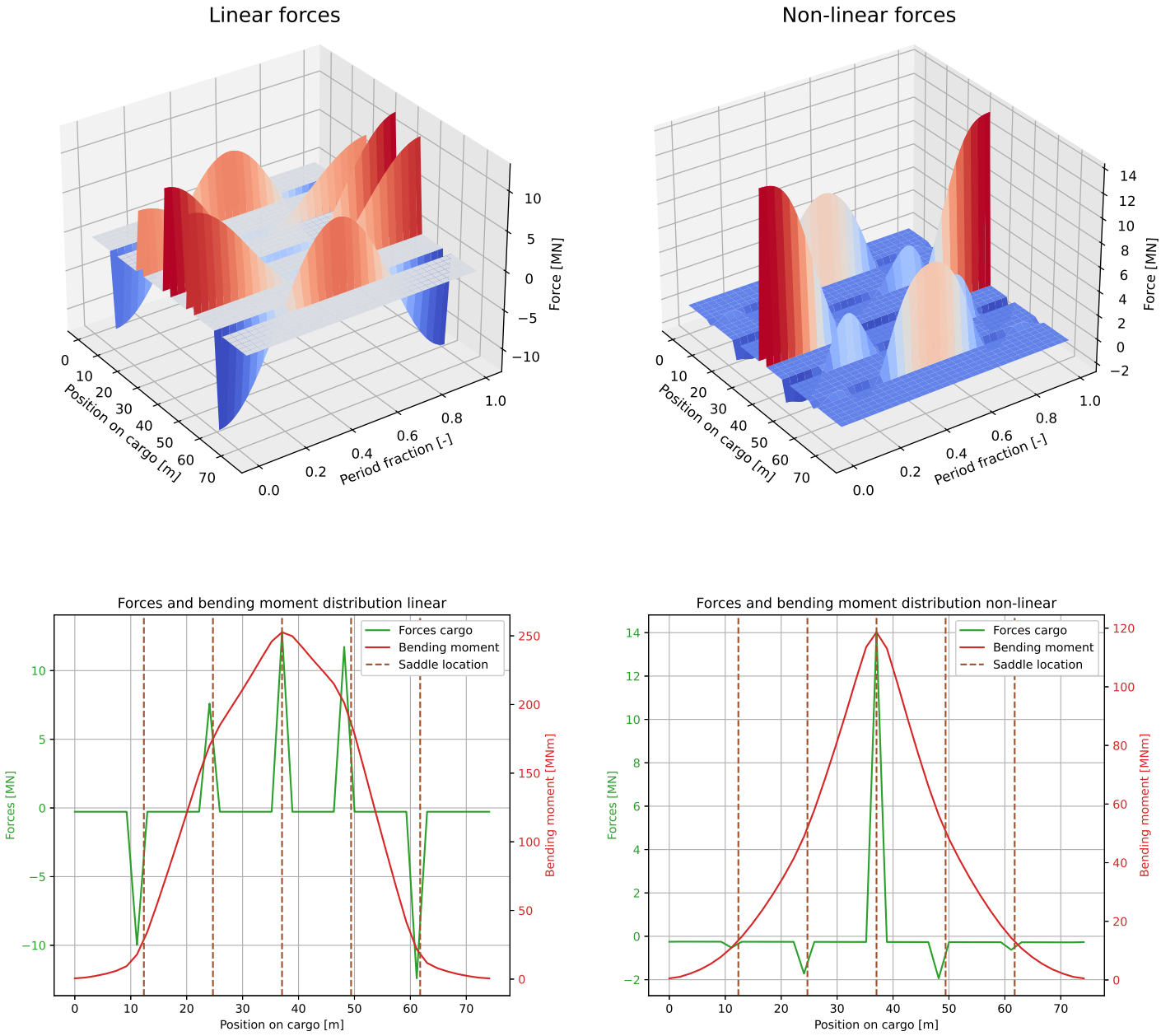

Figure I.1: Force distribution for situation with 5 saddles in combination with 10 times the saddle stiffness. The 2D plots represent the force and bending moment distribution for the beginning of the oscillation, so $t = 0$.

The overconstrained situation is not confirmed by the maximum force observed in the system, but by the maximum observed bending moment. Table I.1 shows the main results for the linear and non-linear analysis. These tables confirm the observed behavior shown in the figures. Furthermore, the maximum deflection of the monopile shows that for the linear case, the cargo is forced into a far larger deflection compared to the non-linear case. Furthermore, this table shows as well that the non-linear deflection of 13 mm is larger then the deflection under its own weight of 12 mm. As mentioned earlier, this is caused by the tensile saddle forces. At last, overconstraining by a linear approach is also visible for the bending moment, which is more than double the value observed for a non-linear approach.

Table I.1: Maxima for 5 saddles in combination with 10 times stiffness for linear and non-linear model

Parameter		Linear	Non - Linear	Unit
Deflection monopile	u_m	34.9	13.1	mm
Deflection saddle	u_s	1.9	2.3	mm
Detachment	u_d	-	15.3	mm
Force	F	12.8	14.0	MN
Bending moment	M_b	118.6	252.6	MNm
Bending stress	σ_b	30.4	64.7	MPa

At last, the figures shown in I.2 show the deflection of the cargo, for reference.

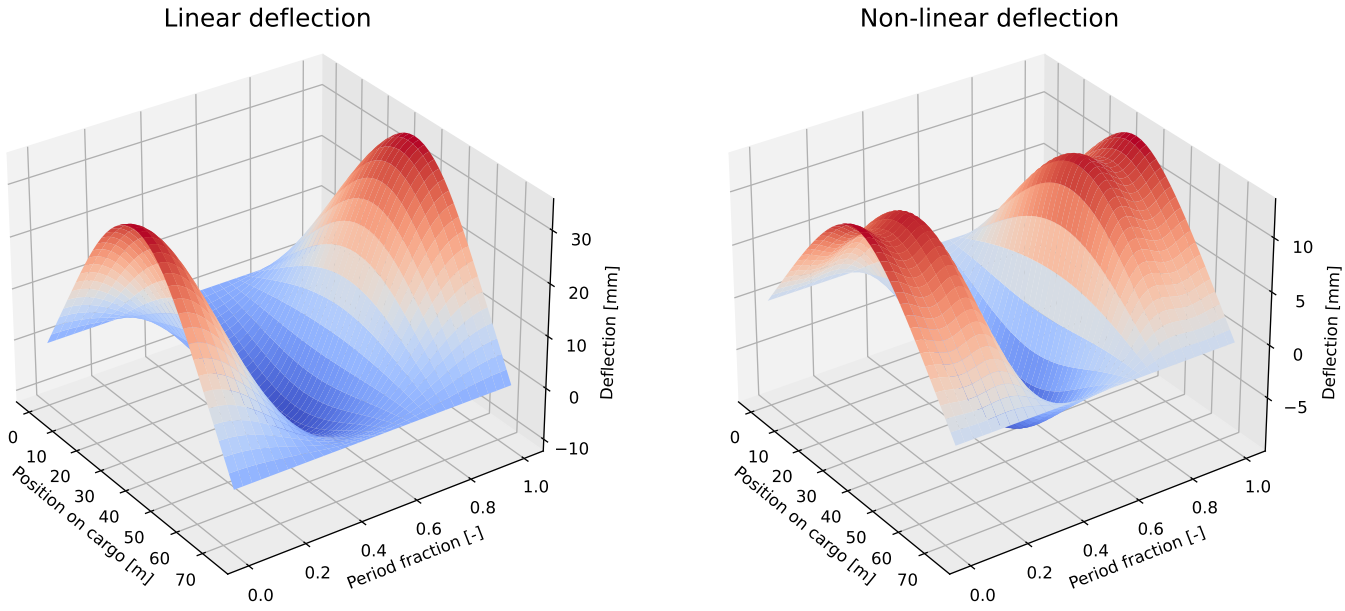

Figure I.2: Deflection for length of monopile and instance in time, analysed in a linear and non-linear manner

J

Limit case saddle analysis

Figure J.1 shows additional results for the limit case analysis. The displacement shows the same pattern for the observed forces, indicating that the forces in the sea-fastening system are predominantly defined by inertial contributions. Table J.1 shows the numerical results corresponding to the limit case. This table shows that the deflection of the saddles becomes significant, in the same order of magnitude as observed for the vessel. Furthermore, this table shows as well that the deflection of the monopile drops down to small values, indicating that the load transferred to the monopile is low.

Table J.1: Maxima for 7 saddles in combination with 0.006 stiffness for linear model

Parameter		**Linear**	**Unit**
Deflection monopile	u_m	3.3	mm
Deflection saddle	u_s	259.5	mm
Force	F	1.5	MN
Bending moment	M_b	19.5	MNm
Bending stress	σ_b	5	MPa

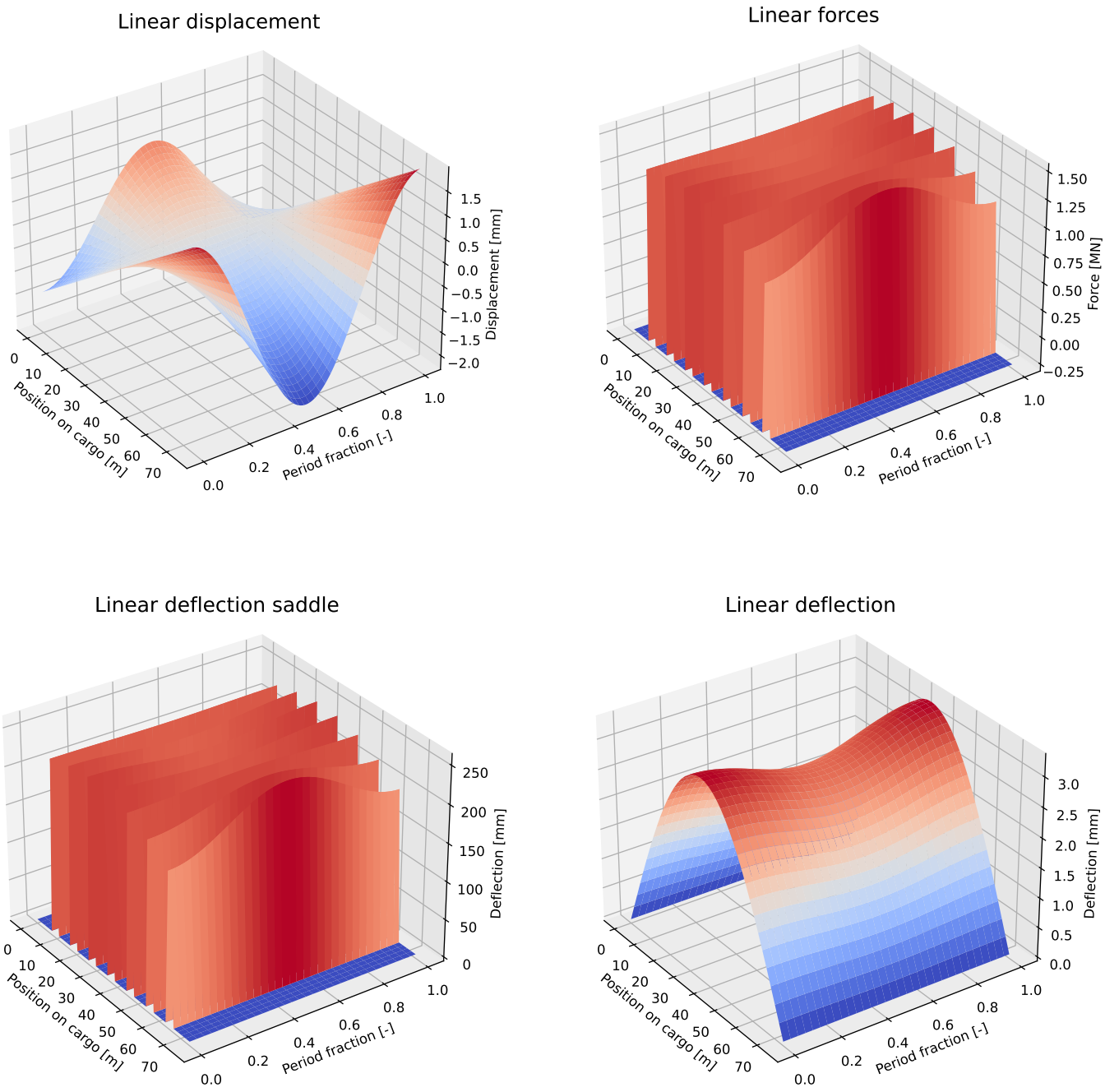

Figure J.1: Additional results for the limit case of the saddle analysis

K

Additional results parametric analysis lashing

Linear deflection

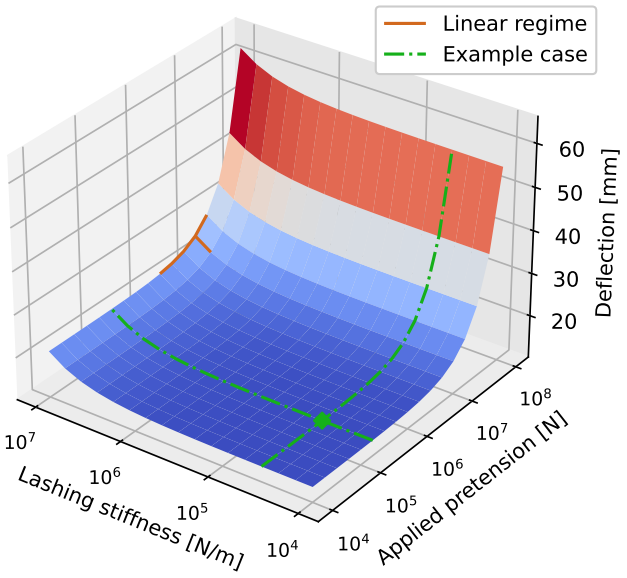

Non-Linear deflection

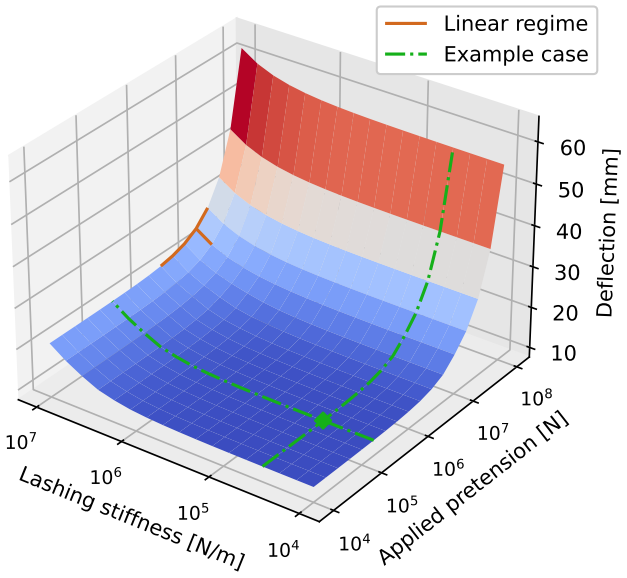

Non-Linear detachment

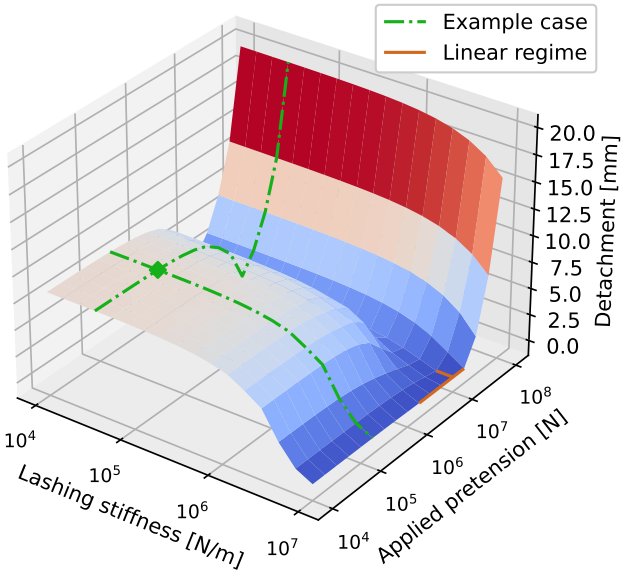

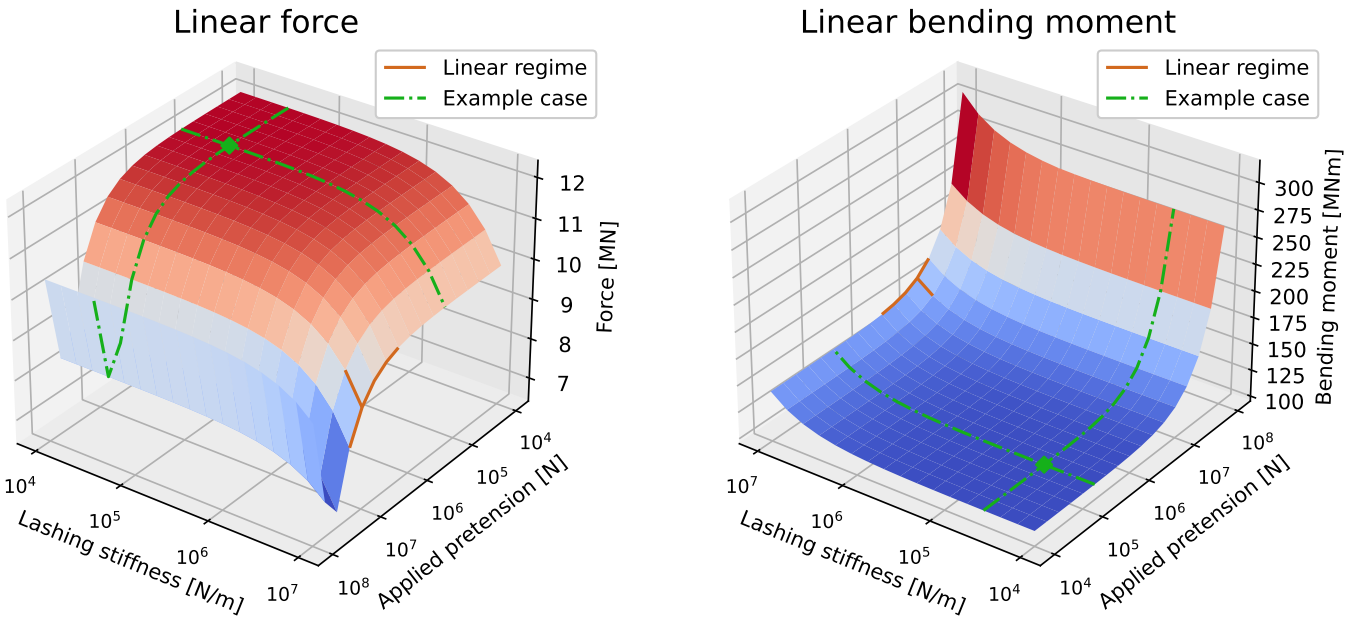

Figure K.2: Additional results for parametric analysis lashing stiffness and lashing pretension. Every results is the maximum value observed.

L

Example case lashing analysis

Figure L.1 shows an example case for the lashing analysis. The saddle parameters are equal to the ones defined in the base case. For the pre-tension a value of 10^8 N is used, while for the lashing stiffness a value of 10^7 N/m is used.

these figures show that due to the high pre-tension, the monopile has forced contact with the first and last saddle. The normal force is therefore again distributed over 2 saddles again, leading to a lower maximum normal force. Furthermore, the 2D plots show that at $t = 0$ the bending of the monopile is almost equal to the bending of the vessel. Note that in this situation the pretension force in the lashing wire far exceeds the normal forces observed for the saddles.

Table L.1 shows the results for the example case. This table shows that due to this pre-tension the deflections and bending moments reach high values. The table shows that for high pre-tension the detachment of the monopile becomes large. This is due to the pre-tension becoming so large that it causes the monopile to bend above the middle saddle.

Table L.1: Maxima for lashing example with a pre-tension 10^8 N and lashing stiffness of 10^7 N/m for linear and non-linear model

Parameter		**Linear**	**Non - Linear**	**Unit**
Deflection monopile	u_m	62.1	62.0	mm
Deflection saddle	u_s	9	5.3	mm
Detachment	u_d	-	15.2	mm
Force	F	9.5	5.5	MN
Bending moment	M_b	311.3	310.9	MNm
Bending stress	σ_b	79.8	79.7	MPa

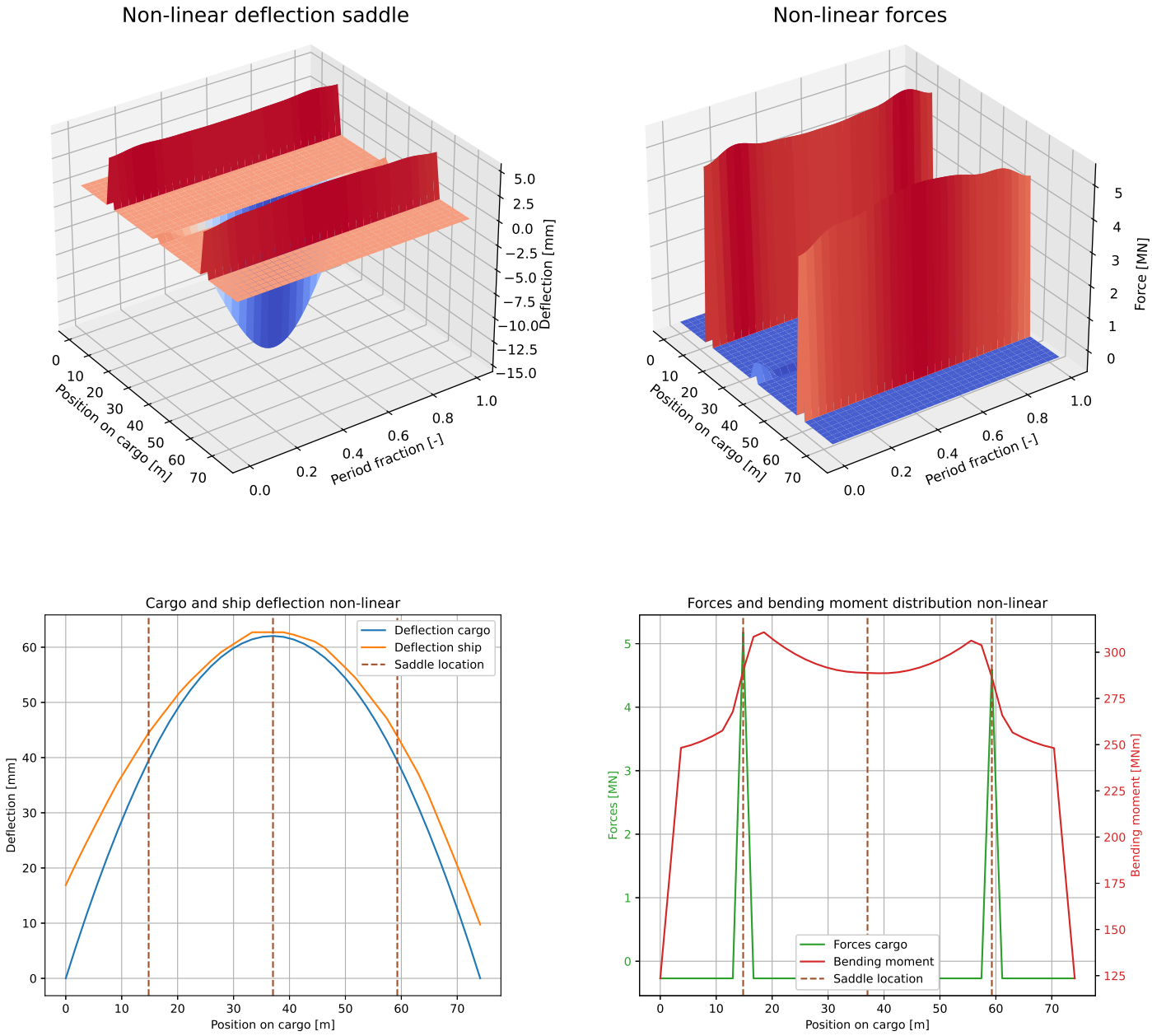

Figure L.1: Deflection and forces for example case lashing analysis. Lashing stiffness of 10^7 N/m is used in combination with a lashing pretension of 10^8 N.

M

Additional results parametric analysis cargo

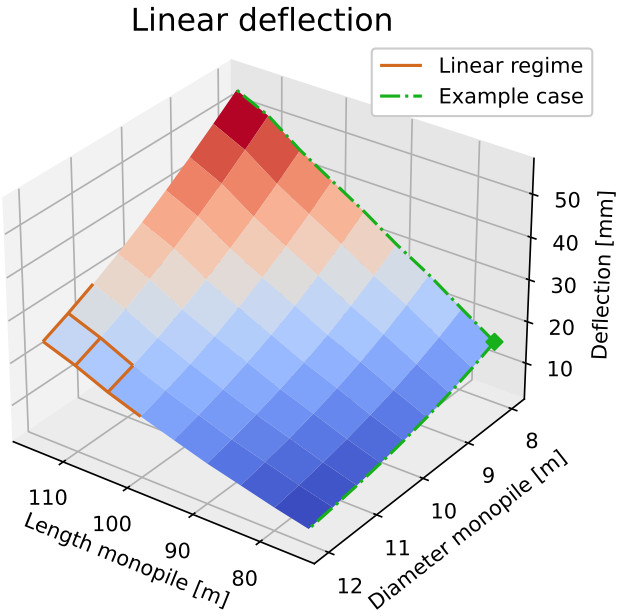

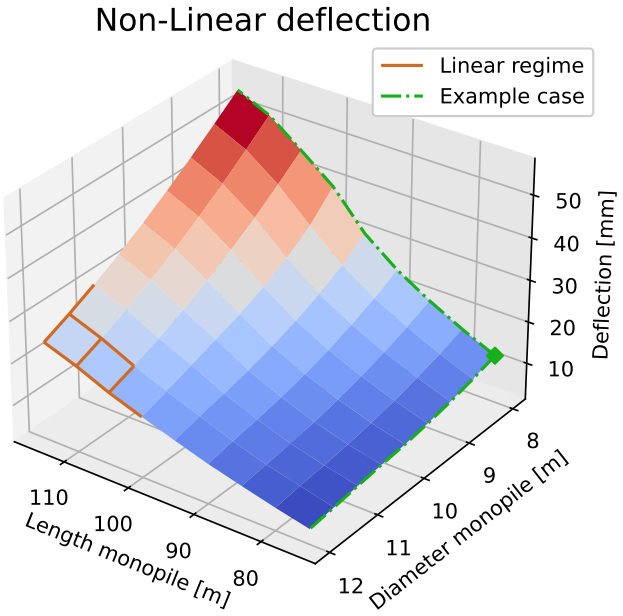

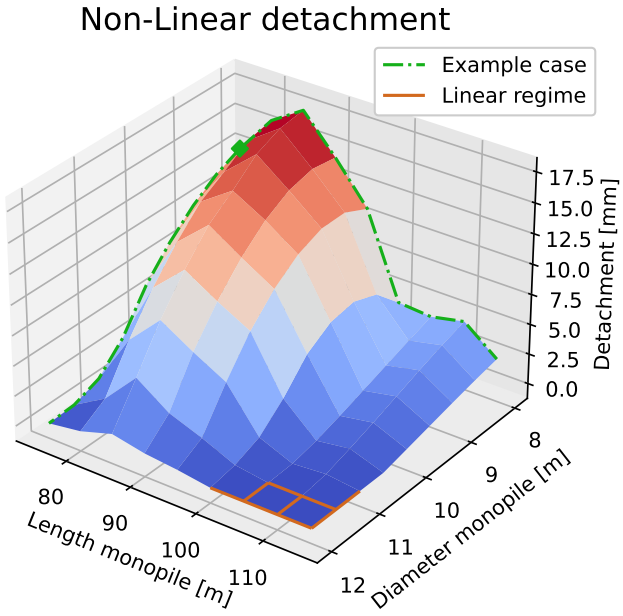

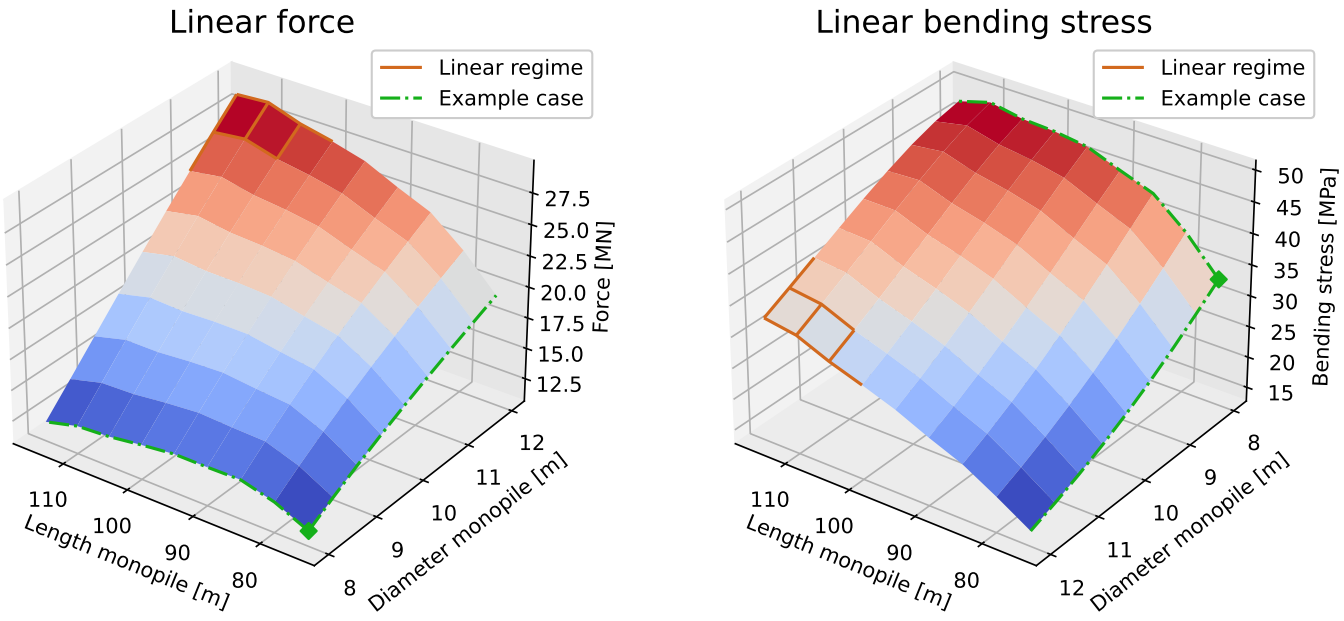

Figure M.2: Additional results for parametric analysis number of saddles and saddle stiffness. Every results is the maximum value observed.